Mapping microclimate temperatures in open ecosystems using UAVs: a comparison between thermal, correlative, and mechanistic approaches

Christophe Metsu[a,b], Sander Raets, Marijke Thoonen[c,d], Stef Haesen[a,b], Reinout Vandenabeele[a,b], Karlien Moeys[a,b], Sam Ottoy[a,e,f], and Koenraad Van Meerbeek[a,b].

Affiliations:

[a] Division Forest, Nature and Landscape, Department Earth and Environmental Sciences, KU Leuven, 3000 Leuven, Belgium
[b] KU Leuven Plant Institute, KU Leuven, 3000 Leuven, Belgium
[c] Research Institute for Nature and Forest (INBO), 1000 Brussels, Belgium
[d] Forest & Nature Lab, Ghent University, Gontrode, Belgium
[e] Bio-Research, PXL University College, 3590 Diepenbeek, Belgium
[f] Center for Environmental Sciences, Hasselt University, 3590 Diepenbeek, Belgium
*Corresponding author: christophe.metsu@kuleuven.be

Keywords: Microclimate, Modelling, Open ecosystems, UAV, *microclimf*, Thermal, Remote Sensing, Machine Learning, Heathland, Temperature, Land Surface Temperature, Drone

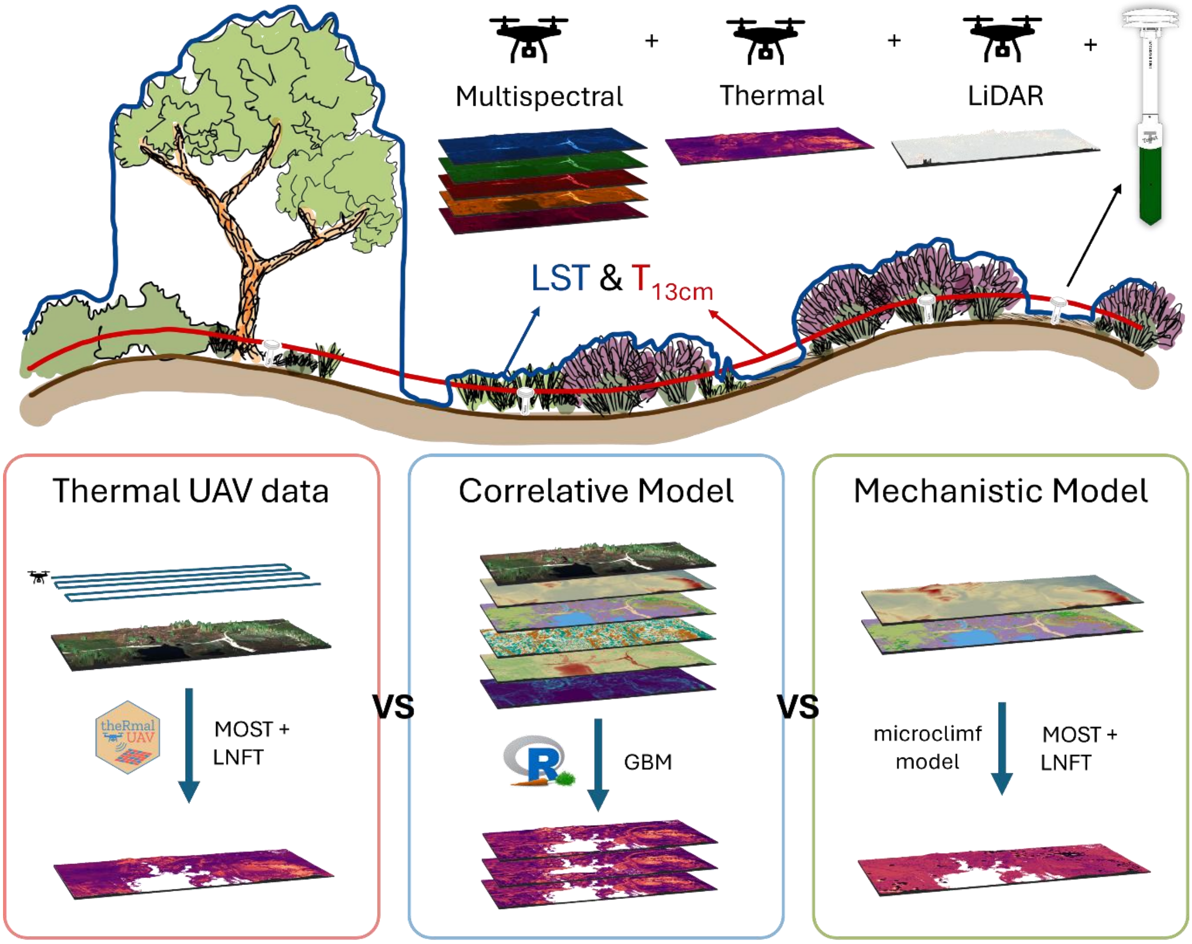

Abstract

Open terrestrial ecosystems exhibit pronounced fine-scale thermal heterogeneity, yet spatially continuous microclimate data at biologically relevant heights and scales remain scarce. Here, we evaluate three unoccupied aerial vehicle (UAV)-informed approaches for mapping microclimate temperatures, including land surface temperature (LST) and near-surface air temperature (T_{13cm}), in an open heathland ecosystem. The approaches comprise a correlative gradient-boosted model (GBM), the mechanistic microclimate model *microclimf*, and UAV-based thermal remote sensing, with LST physically converted to near-surface air temperature. The comparison was conducted across four summer UAV campaigns in 2024 under clear-sky and overcast conditions. All spatial predictor variables, including topography, vegetation structure, land cover, and NDVI, were derived from UAV-borne thermal, multispectral, and LiDAR sensors. The GBM showed the closest agreement with in situ TOMST TMS-4 logger measurements for near-surface temperature (RMSE = 2.22 °C), followed by the UAV-based thermal conversion (3.37 °C) and *microclimf* (4.43 °C). Differences among approaches were systematic: *microclimf* generally underestimated near-surface temperatures, particularly beneath solitary trees, whereas the UAV-based thermal approach tended to predict higher temperatures, reflecting sensitivity to vegetation parameterization, spatial alignment, and potential radiative warming of shielded loggers. UAV-derived thermal observations captured more extreme LST values and sharper spatial contrasts than either correlative or mechanistic models, revealing fine-scale thermal mosaics characteristic of these open ecosystems. Overall, our results demonstrate that UAV-based thermal remote sensing, particularly when integrated with multispectral and LiDAR-derived structural information and physically based temperature conversions, provides complementary value to established microclimate modelling approaches by resolving thermal extremes and spatial variability that are otherwise smoothed or overlooked.

1. Introduction

Microclimate modelling has gained strong attention in recent years within ecology and environmental meteorology. It plays a key role in understanding how climate change affects organisms in our ecosystems (Bramer et al., 2018; Kemppinen et al., 2024). Unlike macroclimate temperature—the free-air temperature measured by weather stations—microclimate temperature better reflects the conditions organisms actually experience (Klinges et al., 2024). Topography and vegetation properties, such as canopy height and cover, strongly shape these conditions. As a result, microclimate temperatures can differ greatly from macroclimate values (De Frenne et al., 2021; Lembrechts et al., 2022). Consequently, retrieving and modelling microclimate has become a central topic in microclimate ecology. This interest has grown further as microclimate information has been shown to improve species distribution models by representing biologically relevant thermal conditions and responses in plant dynamics due to climate warming (Haesen et al., 2023; Lembrechts et al., 2019; Zellweger et al., 2020). It also enables the identification of microrefugia, i.e. locally warmer and colder areas, acting as a potential buffer for organisms against regional climate warming (Greiser et al., 2020; Lenoir et al., 2017; Zhou et al., 2025). Such spatially explicit microclimate maps are, therefore, increasingly recognized as valuable tools for climate-adaptive landscape design and informed nature management.

Empirical microclimate research has its roots in forest ecosystems (De Frenne et al., 2013), grounded in the premise that forest conditions strongly deviate from the macroclimate because dense forest canopies buffer temperature by reducing incoming shortwave radiation and enhancing evaporative cooling (De Frenne et al., 2021). This focus has introduced a strong information bias towards forest ecosystems (De Frenne et al., 2025; Kemppinen et al., 2024). Yet, weather stations are shaded and therefore approximate forest-like conditions, whereas organisms in open ecosystems often experience full exposure to solar radiation (Alujević et al., 2025; De Frenne et al., 2025; Gardner et al., 2019). In open systems, direct radiation amplifies temperature contrasts between vegetated patches and bare soil, increasing both vertical and horizontal thermal heterogeneity at fine spatial scales (Aalto et al., 2022). Additional drivers, such as microtopography, vegetation height and structure, wind exposure, and soil moisture, further shape near-surface temperatures (De Frenne et al., 2021; Greiser et al., 2024). Together, these processes can generate large variation and microclimate–macroclimate mismatches that challenge assumptions of uniform thermal conditions and highlight the need for accurate temperature data in open ecosystems.

Retrieving accurate temperature measurements in open ecosystems remains, however, challenging when sensors are exposed to direct solar radiation. To minimize radiative heating, microclimate researchers aiming to measure air temperature typically shield their temperature loggers. Yet, these shields might not always offer solutions to the problem as they absorb radiation themselves while not allowing for sufficiently air flow between the shield and the sensor itself, leading to erroneous temperature values as well (Maclean et al., 2021). As a result, debate continues on how to collect accurate in situ temperatures in open ecosystems (De Frenne et al., 2025). Recent work points to thermocouples as the most accurate option (Maclean et al., 2021). However, sensor choice involves trade-offs where accuracy often conflicts with feasibility, robustness, cost and comparability.

In addition, when the objective is to produce spatially continuous maps of microclimate, point-based field measurements alone are insufficient. Furthermore, the ability to model temperature variability over short distances requires data at very high spatial resolution. Recent advances in remote sensing—particularly reduced sensor costs and miniaturization—have driven a rapid increase in the use of unoccupied aerial vehicles (UAVs) in environmental research to provide such fine-scale information (Manfreda et al., 2018; Zellweger et al., 2019). Within microclimate ecology, several approaches have therefore been developed to derive spatially explicit temperature maps:

Correlative models link observed microclimate temperatures to environmental variables, typically including topography, vegetation properties, and macroclimate forcing, through statistical approaches (Davis et al., 2019; Gril et al., 2023) or machine learning (Haesen et al., 2021; Lembrechts et al., 2022). Their strengths lie in computational efficiency and scalability. They also integrate high-resolution terrain data effectively, and macroclimatic variables are not always needed at high temporal resolution (Fick and Hijmans, 2017; Kemppinen et al., 2024). However, they perform poorly outside their training range (Aalto et al., 2022). Reliable and transferable models, therefore, require very large logger networks that capture a wide range of environmental variation.

Mechanistic models explicitly solve energy-balance equations, including radiation, sensible and latent heat, and wind. They generate physically consistent estimates of temperature, humidity, and soil moisture at high temporal resolution (Kearney et al., 2020; Maclean, 2026). Because the underlying physics remain valid across systems, these models transfer well between ecosystems and climate scenarios. They also resolve vertical temperature profiles above and within canopies (Kolstela et al., 2024; Maclean and Klinges, 2021). However, they require highly-specific input layers, such as leaf area index, leaf orientation, leaf width, stomatal conductance, and soil reflectance, which are often unavailable or uncertain. Small parameter errors can propagate and bias temperature estimates. In addition, high-resolution or large-area applications remain computationally demanding. However, statistical model emulation techniques can offer a way forward in this avenue (Baker et al., 2022).

Thermal remote sensing directly measures land surface temperature (LST). A key limitation is its low temporal resolution, as it provides only instantaneous observations. While methods to overcome the limited temporal coverage of UAV-based thermal data are beginning to emerge, such as Alujević et al. (2025), most applications remain temporally sparse. Moreover, thermal sensors capture surface temperatures only and cannot penetrate vegetation canopies, limiting their ability to characterize sub-canopy microclimates (Zellweger et al., 2019). These constraints are further exacerbated for satellite-based thermal data, which typically have coarse spatial and temporal resolution (Andriambololonaharisoamalala et al., 2025). In contrast, thermal UAV data provide much finer spatial detail, allowing the detection of small-scale thermal heterogeneity that is particularly relevant in open ecosystems (Metsu et al., 2026). When repeated across seasons and times of day, UAV surveys can reveal thermally stable areas as well as persistent warm and cool spots, which may indicate potential microrefugia (Hoffrén and García, 2023). Despite this clear potential, integration of surface- or canopy-level temperatures derived from thermal remote sensing into established microclimate modelling frameworks remains limited (Zellweger et al., 2019).

Deriving spatially continuous, high-resolution microclimate temperatures in open ecosystems remains challenging. Here, we compare three approaches for estimating microclimate temperature in an open heathland ecosystem: (1) a correlative gradient-boosted model; (2) a parameterized mechanistic microclimate model, and (3) thermal UAV observations. The analysis covers four summer days under varying meteorological conditions. All spatial input variables, except soil parameters, originate from UAV-based sensors. The comparison encompasses both surface and near-surface temperature, with the aim of demonstrating the methodological potential of thermal UAV observations to estimate near-surface temperature.

2. Material and Methods

2.1. Study area

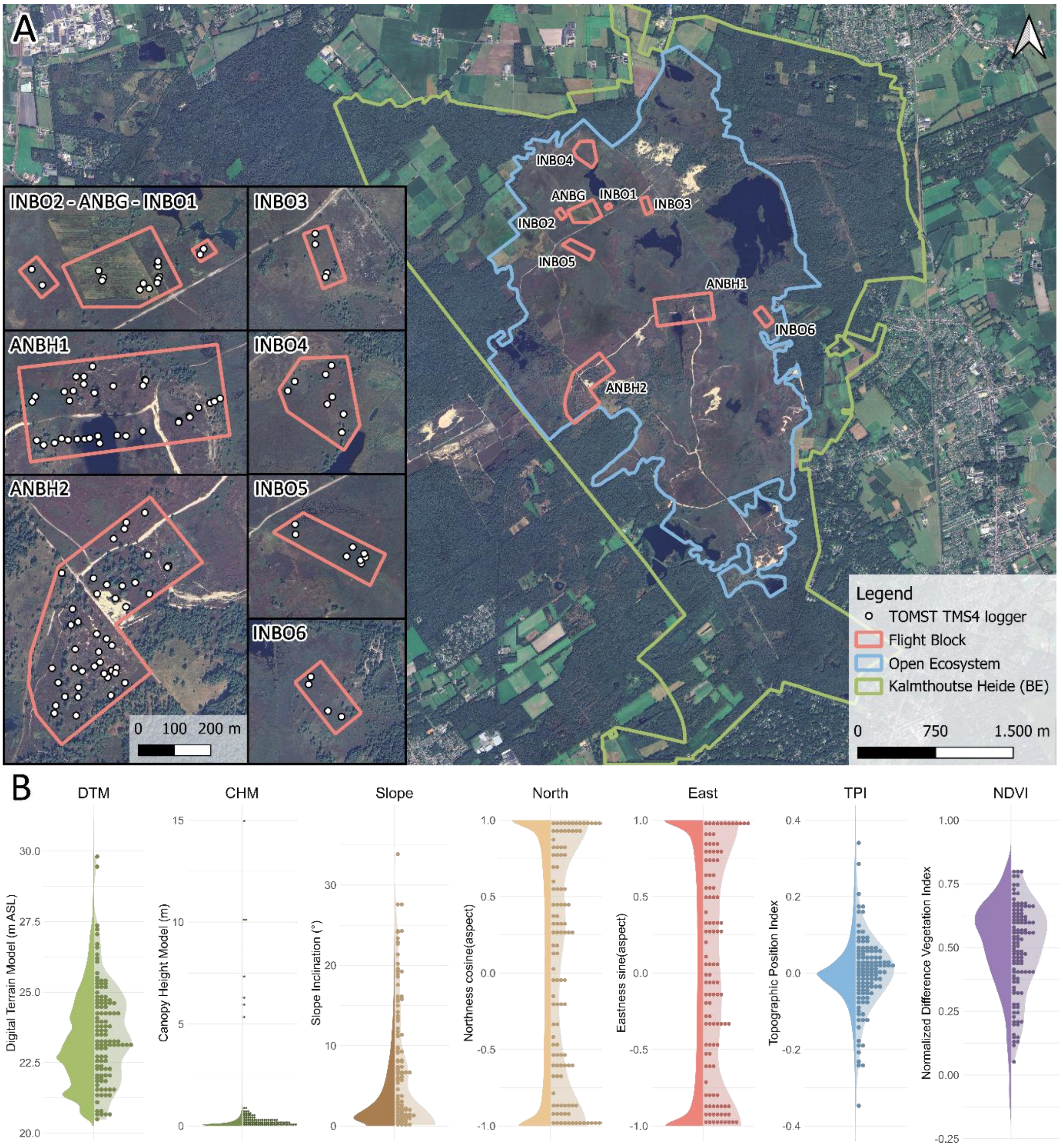

Figure 1. Study area and sampling coverage. *A) Location of the UAV flight blocks (red) within the open ecosystems of Grenspark Kalmthoutse Heide (blue outline; Belgian part in green). B) Environmental variability of the study area (left) and the conditions represented by the 119 TOMST TMS-4 loggers (right), based on LiDAR and multispectral UAV data.*

The study took place in Grenspark Kalmthoutse Heide (51°24'N, 4°25'E), a transboundary nature reserve of approximately 60 km² located in Belgium and the Netherlands. The area includes heathlands, grasslands, fens, dunes, pine and deciduous forests on predominantly sandy soils. The open ecosystem consists mostly of a mosaic of Common heather (*Calluna vulgaris*), Cross-leaved heath (*Erica tetralix*), and Moor-grass (*Molinia caerulea*). Large parts are also grazed by cattle (extensive grazing) and sheep (pulse and herded grazing). Nine subareas were selected to span key environmental gradients, such as vegetation type, cover, and topography. These subareas are hereafter referred to as “flight blocks”, as UAV surveys targeted them (Figure 1A).

2.2. Data acquisition

2.2.1. Climate data

This study used a microclimate logger network consisting of 119 TOMST TMS-4 loggers (Wild et al., 2019) measuring soil (-8 cm), surface (0 cm), and near-surface air (13 cm) temperature at 15-min intervals (Figure A1). To ensure coverage across the full range of environmental gradients (**Figure 1**B), we followed the procedure described by Lembrechts et al. (2021) to select logger locations within the Principal Component space of our study area created using gridded environmental products. To limit the influence of direct solar radiation, the sensors were equipped with a triple-shield setup, and the 0 cm sensor faced north. The lowest shield had a doughnut shape to promote airflow. Because large parts of the study area are grazed, chromed steel wired cages protected some loggers from trampling (Supplementary information Figure A1), while some were explicitly not equipped with this protection to avoid flattening of the surrounding vegetation, thereby disturbing vegetation structure and thus microclimate. The exact logger locations were recorded using an Altus APS3G Septentrio real-time kinematic (RTK) system with an accuracy of 0.02 m. Loggers were deployed in late summer 2023 and data were retrieved in October (INBO sites) and December 2024.

Macroclimate variables, including wind speed, wind direction, air temperature at 2 m height, relative humidity, global radiation, downwelling longwave radiation, and atmospheric pressure, were retrieved as hourly aggregates from a nearby automatic weather station operated by the Royal Meteorological Institute of Belgium in the municipality of Stabroek (approximately 9 km from the study site). In addition, cumulative precipitation over the preceding two days was calculated as a proxy for surface moisture and water retention in moss layers.

2.2.2. UAV data

All UAV data were collected using a DJI Matrice 300 RTK. Flights were conducted in combination with a DJI D-RTK 2 mobile station to improve positional accuracy. To enhance image alignment across survey periods, permanent thermal ground control points (GCPs) were distributed across the large flight blocks (ANBH1, ANBH2, ANBG). Each GCP consisted of four squares in a checkered pattern, where the white squares were covered with aluminum foil to ensure contrast in both short- and long-wave radiation (Maes, 2025). GCP locations were measured using an Altus APS3G Septentrio RTK system.

LiDAR (Light Detection and Ranging) data were acquired using a YellowScan Surveyor Ultra sensor equipped with a Hesai XT32M2X scanner. The system operates at 640,000 pulses per second and provides a reported precision and accuracy of 3 cm. Flights were conducted on 16 October 2024 between 10:00 and 15:45 Central European Summer Time (CEST). Data were collected at 75 m above ground level (AGL), with a flight speed of 5 m s^{-1} and a line spacing of approximately 25 m. This configuration yielded point clouds with a weighted mean density of 532 points m^{-2}.

Multispectral (MSP) data were collected using an AgEagle MicaSense Altum-PT sensor equipped with a DLS-2 downwelling light sensor. Data were acquired in the blue, green, red, red-edge, near-infrared (NIR), and thermal infrared (TIR) bands (Table A1). Flights were conducted on 19 September 2024 under clear-sky conditions between 09:45 and 15:45 CEST. These UAV missions were executed at 100 m AGL, with a speed of 6.6 m s^{-1} and 75% forward and side overlap. This resulted in a ground sampling distance of 4.32 cm. A 50% reflectance calibration panel (60 × 60 cm) was placed on the ground, centrally in the flight block. Images of the panel were acquired at flight altitude at the start, middle and end of each mission.

Thermal data were acquired using a TeAx ThermalCapture 2.0 sensor with an integrated calibrator, built around a FLIR Tau2 core (640 × 512 pixels). The calibrator enabled regular flat-field correction using a blackbody during flight, reducing sensor non-uniformity caused by wind and platform orientation. This setup resulted in an absolute radiometric accuracy of 1.5 °C and a thermal resolution of 0.04 °C (TeAx, 2022). The thermal sensor was co-registered with the MicaSense Altum-PT to leverage RTK positioning and enable simultaneous multispectral acquisition. Flights were conducted at 75 m above ground level, with a speed of 5 m s^{-1} and 75 % horizontal overlap. Vertical overlap was defined during preprocessing and set to a minimum of 90 %, given its 8 Hz acquisition rate (Section 2.3.4). This configuration yielded a spatial resolution of approximately 10 cm.

During each thermal flight, air temperature and relative humidity were recorded at 5-s intervals using a Kestrel 5500L environmental meter. Crumpled aluminum foil panels were deployed to estimate background temperature (Maes et al., 2017; Metsu et al., 2026). Four thermal flights were conducted during the summer under both clear and overcast conditions (Table 1).

Table 1. Overview of executed thermal UAV flights with the corresponding atmospheric information. *The time of flight (halfway point of the flight) is given as local time (CET), Sky indicates whether the sky was sky clear (without clouds, SKC) or if there was a full homogeneous overcast (OVC), air temperature (°C), relative humidity (%), wind speed (m/s), wind direction (°), downward shortwave radiation (Sw down, W/m^2), and downward long wave radiation (Lw down, W/m^2) are the aggregated hourly means corresponding to the hour in which the flight occurred, derived from the Royal Meteorological Institute from Belgium.*

Flight	Datetime	Sky	Air Temperature (°C)	Relative Humidity (%)	Wind Speed (m/s)	Wind Direction (°)	Sw down (W/m^2)	Lw Down (W/m^2)
1	2024-06-13 18:20	OVC	18.7	48.9	6.0	212.9	197.0	349.7
2	2024-06-26 16:30	SKC	29.9	42.5	1.8	29.3	719.8	391.5
3	2024-07-25 12:45	OVC	21.9	64.5	5.1	190.0	430.2	399.5
4	2024-08-06 17:15	SKC	28.1	48.5	4.3	227.9	518.2	388.2

2.2.3. Soil Variables

Soil data were obtained from Databank Ondergrond Vlaanderen, providing spatially interpolated maps of sand, silt, and clay fractions (%) of the upper 10 cm at a 10-m spatial resolution (Wittemans et al., 2023). Consequently, fine-scale variability in local soil conditions may not be fully captured.

2.3. Data processing

Apart from sensor or UAV-specific software mentioned in the relevant sections, all analyses were performed in R version 4.3.1 (R Core Team, 2023). Data manipulation relied primarily on dplyr v1.1.4 and tidyverse v2.0.0 (Wickham et al., 2023, 2019). Spatial analyses were conducted using terra v1.8-29 (Hijmans, 2025), and figures were produced using ggplot2 v3.5.2 (Wickham, 2016). QGIS 3.28.3 (QGIS Development Team, 2025) was used for spatial data inspection and management. Moreover, QGIS' georeferencer tool was used to align different layers based on the GCPs and distinctive features in the landscape. Here, the thin plate spline transformation and a cubic resampling method was chosen. To match the spatial resolution of the thermal UAV data, all spatial layers were generated or resampled to 10-cm resolution. This resolution allowed discrimination of fine vegetation structure while remaining computationally feasible.

2.3.1. Microclimate

Raw sensor data were partially processed using the myClim package (Man et al., 2023). Extreme values (> 70°C and < -20°C), outliers (temperature differences >10 °C between consecutive measurements), and flatlines (no temperature variation over 24 h), indicative of sensor malfunction, were removed. When radiation shields were removed or damaged by grazers or hikers, data from the preceding two weeks were excluded, corresponding to the biweekly field inspection interval.

The winter of 2023–2024 was exceptionally wet, resulting in five loggers remaining permanently submerged throughout 2024 and reducing the final dataset to 114 loggers. Some loggers were temporarily submerged until varying dates in spring; these periods were excluded from the analysis. As the study focuses on summer conditions, the dataset was restricted to the period from 15 March to 15 October 2024. The cleaned time series were subsequently aggregated to hourly resolution.

Due to the very high spatial resolution of the UAV-derived data, radiation shields and metal cages locally affected multispectral reflectance (and consequently NDVI and land cover classification, see Section 2.3.3) as well as thermal measurements at the exact logger positions. To extract representative environmental information, logger locations were adjusted to a nearby representative pixel within a radius of approximately 0.5 m, based on similarity in NDVI, land-cover class, canopy height, and topographic position.

For each hour within the study period, solar geometry was calculated using the microctools v0.1.0 package (Maclean, 2025). Solar altitude and azimuth were derived from Julian day, local time, and the central coordinates of the study site.

2.3.2. LiDAR UAV data processing and derivates

Initial LiDAR processing was performed in CloudStation v2007.0.1 (YellowScan, 2024). Post-processing kinematic corrections were applied using Applanix POSPac MMS 8.9 (Applanix, 2023). A virtual reference station was created using three Flemish positioning service (FLEPOS) RTK stations. This workflow produced a smooth best estimate trajectory (SBET) used for georeferencing. The coordinate reference system was set to WGS84 UTM 31N (EPSG:32631), with orthometric heights derived using the HBG03 (Belgium) geoid model. The point cloud was classified into ground and non-ground points using CloudStation. Classification parameters included an inner object size of 10 m, steepness of 0.05 (hilly), minimum object height of 0 m, and point cloud thickness of 0.1 m, with low-point removal enabled. The digital terrain model (DTM) was exported as a GeoTIFF at 0.5-m resolution using mean elevation per pixel and further smoothed in R using a Gaussian kernel ($n = 15$, $\sigma = 3$) from the spatialECO package (Evans, 2023). The DTM was then resampled to 10-cm resolution. The canopy height model (CHM) was derived by subtracting the DTM from the digital surface model (DSM), both exported as a GeoTIFF at 10-cm resolution. Artefacts in the DSM were set to NA and interpolated using neighbouring pixels. A DTM generated at 10-cm resolution was preferred over the smoothed one, as the latter introduced negative CHM values due to the smoothing and averaging.

Slope (°) and aspect (radians) were derived from the smoothed DTM using terra. Aspect was transformed into northness and eastness using cosine and sine transformations. The topographic position index (TPI) was calculated using the MultiscaleDTM package with a 10 m × 10 m kernel as measure to distinguish local depressions and hilltops in the landscape (Ilich et al., 2023). Surface roughness, i.e., the amount of topographical variation, was quantified with the same package using the vector ruggedness measure (VRM) on the DSM with a 3 m × 3 m kernel.

2.3.3. Multispectral UAV data and derivates

Multispectral images were processed in Agisoft Metashape v2.0.0 (Agisoft, 2022) following the MicaSense Altum-PT recommendations (Agisoft, 2024). Reflectance calibration used images of the 50 % calibration panel. DLS-2 data were included only under overcast conditions as recommended by Micasense (MicaSense, 2024). Images were aligned with high accuracy (with a 40,000 key point limit and 10,000 tie point limit), followed by dense point cloud generation using a mild depth filter (to avoid cutting of the tops of the vegetation). Subsequently, a digital elevation model was generated from the dense point cloud and used as the base raster for mosaicking reflectance values, applying the default "mosaic" blending mode. The final orthomosaics (WGS84 UTM 31N) were exported as a five-band raster stack (blue, green, red, red-edge, NIR) at a spatial resolution of approximately 4.5 cm. Note, the values were divided by 32768, to convert the 16 bit output to reflectance values between 0 and 1.

We derived the Normalized Difference Vegetation Index (NDVI; Rouse et al., 1974) from the multispectral data as a proxy for vegetation density. In addition, we divided the landscape into different land cover (LC) classes: grass, heath(shrubs), moss, bare sandy soil and trees. Training data was created by drawing shapefiles on high-resolution RGB composites. A Random Forest (RF) classifier was trained and tuned on the spectral bands, CHM and NDVI using the R-packages *ranger* v0.16.0 (Wright and Ziegler, 2017) and *Caret* v6.0-94 (Kuhn, 2008a). Models were fitted with 500 trees. Hyperparameters were tuned using a grid search over *mtry* (1–4), *min.node.size* (3, 5, 7, 9), and *split rule* ("gini", "extratrees", "hellinger"), evaluated via 10-fold cross-validation. Model selection based on the kappa index of agreement identified an optimal configuration with *mtry* = 4, *min.node.size* = 3, and the "gini" *split rule*. This model achieved an overall accuracy of 94.6% and a kappa coefficient of 0.927. More detailed information on the land cover classification, as well as the spatial outputs, can be found in the Supplementary Information (Appendix B).

2.3.4. Thermal UAV data

Thermal data from the ThermalCapture 2.0 camera were recorded as .TMC files and converted to TIFF format using ThermoViewer 3.0.10 (TeAx Technology, 2020), with metadata exported as a .csv file. Because the sensor provides at-sensor temperatures, radiometric and atmospheric corrections were applied using the theRmalUAV R package (Metsu et al., 2026), following the image-based workflow. Images were filtered to retain at least 90% overlap, background temperature was estimated from aluminum reference panels, and atmospheric correction was performed using meteorological data from the Kestrel 5500L weather station, assuming emissivity = 1 to obtain corrected brightness temperatures. Air temperature effects were accounted for (Maes et al., 2017; Metsu et al., 2026), and subsequently, the brightness temperature orthomosaics were generated in Agisoft Metashape using default settings. To derive the LST, a spatial emissivity correction was applied (Metsu et al., 2026) based on flight-specific land cover maps derived from multispectral imagery (Appendix B). Emissivity values were assigned per land cover class following Rubio, Caselles and Badenas (1997), yielding the final corrected LST maps. More detailed information regarding the processing of the thermal UAV data can be found in the Supplementary Materials (Appendix C).

2.4. Modelling

2.4.1. Gradient Boosted Models

In this study, we applied a gradient boosted modeling (GBM) approach for the correlative microclimate predictions of the hourly aggregated TMS-4 microclimate temperature (°C) at either ground or near the surface. GBM is a machine learning technique that uses an ensemble of decision trees (shallow learners), where each consecutive tree is trained to model the residuals of the preceding ensemble through boosting (Elith et al., 2008). Spatial predictors included: elevation (m), canopy height (m), northness and eastness, slope (°), topographic position index (m), surface roughness, land cover class, normalized difference vegetation index, and soil fractions (%). Weather related predictors included: macroclimate temperature (°C), wind speed (m s^{-1}), relative humidity (%), global shortwave radiation (W m^{-2}), solar altitude and azimuth (°), accumulated precipitation over the preceding 48 h (mm), and downwelling longwave radiation (W m^{-2}). An overview of the input variables used in the different modelling approaches is available in the Supplementary Materials (Appendix D).

Models were trained and tuned using the gbm package v2.2.2 (Ridgeway and GBM Developers, 2024) in combination with caret v6.0-94 (Kuhn, 2008a). Hyperparameter tuning explored combinations of interaction depths (2, 3, 4), number of trees (5,000–10,000, step 500), and minimum observations per node (8, 10, 12). Shrinkage (learning rate) was set to 0.01 to maintain relatively shallow trees and avoid overfitting of the model. Model performance was evaluated using mean absolute error (MAE), root mean squared error (RMSE), and coefficient of determination (R^2). We implemented a 10-fold block cross-validation, constructing folds while accounting for differences between flight blocks. To avoid clustering of validation data, we performed a principal component analysis (PCA) on the environmental variables using the stats package v4.3.1 (R Core Team, 2023), and visually inspected the first three axes to ensure folds adequately captured environmental variability, using the plotly package (Sievert, 2020; Figure E5). Hyperparameter tuning indicated an optimal interaction depth of 4; however, to reduce overfitting, we selected the smallest tested depth of 2, which already approached optimal performance and better captured general trends, consistent with Elith, Leathwick and Hastie (2008). The resulting reduction in accuracy was marginal (0.6 %). Final hyperparameters for both ground (T_{0cm}) and near-surface temperature (T_{13cm}) models were: shrinkage = 0.01; interaction depth = 2; 10,000 trees; and minimum observations per node = 12. The final GBM model formula, variables importances and details on hyperparameter tuning are attached in the Supplementary Materials (Appendix E).

2.4.2. Microclimf

In this study, we used the open-source mechanistic microclimate model *microclimf* (MacLean, 2026; version 0.2.0). This model requires four main types of input data: (1) tabular weather data (Section 2.2.1), with diffuse radiation calculated using microctools (Maclean, 2025), (2) vegetation or habitat information (Section 2.3.3), (3) a DTM (Section 2.3.2), and (4) soil type (Section 2.2.3). Ground reflectance was derived as the average reflectance of representative soil layers using multispectral UAV data. For bare sandy soils, the mean reflectance of this land-cover type was used. For areas covered by moss, including moss present under other vegetation, the reflectance of bare moss was used as the ground reflectance.

As a starting point for parameterization, vegetation parameters were derived from habitat types using the *vegfromhab* function in *microclimf*. To enable this, the land cover types were reclassified to match the *microclimf* habitat categories (Table A2), and canopy height derived from UAV-based LiDAR data (Section 2.3.2) was used as vegetation height. Notably, solitary or small patches of *Pinus sylvestris* were classified as “evergreen needleleaf forest,” as this category provided the closest match to their structural characteristics. Two vegetation parameters were adjusted: plant area index (PAI) and leaf reflectance. PAI was calculated from the NDVI map derived from MSP UAV data (Section 2.3.3) using the empirical relationship $0.1 \times \exp(2.83 \times \text{NDVI})$ for total vegetation established by Juutinen et al. (2017). This produced values similar to *microclimf* estimates while providing higher spatial resolution and variability. PAI was set to zero for bare soil and water. Leaf reflectance was calculated similarly to ground reflectance, as the pixel-wise average of MSP data representing the shortwave reflectance of vegetative surfaces.

Microclimf models were run at an hourly temporal resolution for the days corresponding to thermal UAV flights (Table 1). Each model run used input data from the matching MSP UAV flight. Target heights were set to 13 cm and 20.5 m: 13 cm matched the height of in situ TOMST TMS-4 near-surface temperature sensor, and 20.5 m (slightly above the tallest trees, ~20 m) was used to model leaf (canopy surface) temperatures of shrubs, grasses, trees, and mosses, allowing comparison with UAV-derived LST.

2.4.3. Thermal UAV data

Temperatures derived from thermal UAV data represent land surface temperatures (LST), which reflect the absolute temperature of the landscape surface. These temperatures differ significantly from those measured or modelled at 13 cm above the ground (T_{13cm}, Figure 2). Moreover, thermal UAV data only capture the surfaces visible to the UAV: for shrubs, this corresponds to the canopy temperature above 13 cm, while for mosses, our target temperature of 13 cm is above the measured surface. Although LST is highly relevant for ectotherms (Alujević et al., 2025) and other small surface-dwelling arthropods such as ants, ground beetles, and spiders, it cannot be directly compared with T_{13cm}. Therefore, we converted LST to temperatures at a specified height (T_z). The conversion of LST to T_z depends on both the desired height (z) and the canopy height of vegetation, and follows two distinct approaches: (i) T_z above the canopy or ground surface and (ii) T_z below the canopy or within vegetation. The vegetation height determines which approach is applied for each pixel. For bare soil or moss, the above-canopy method is used, whereas for taller shrubs or grasses, the below-canopy method is applied. These workflows are inspired by the *microclimf* methodology for modelling radiation budgets and T_z above and below vegetation canopies (MacLean (2026); Appendix F).

To model T_z above the canopy or ground, we used Monin-Obukhov Similarity Theory (MOST; Monin and Obukhov, 1954; Foken, 2006) to resolve the energy balance of a vegetated surface, such as moss, grasses, or small shrubs. Above the canopy, turbulence and wind drive heat and vapor exchange between the canopy and the overlying air (Campbell and Norman, 1998). The goal is to estimate near-surface temperature using the canopy temperature (derived from UAV LST) and reference meteorological conditions measured at a reference height, in our study measured at 1.5 m with the Kestrel 5500L environmental meter. The near-surface temperature at height z (°C) above the canopy is calculated as (Maclean, 2026):

$$T_z = T_A + (T_C - T_A)\left(1 + \frac{\ln\frac{z-d}{z_H}}{\ln\frac{z_R-d}{z_H}}\right) \tag{1}$$

where T_C is the canopy temperature (°C), T_A the reference air temperature (°C) at height z_R (m) above the ground, and d the zero plane displacement length (m), a measure representing the height within the canopy where the windspeed approximates zero m s^{-1}. Z_H is the roughness length for heat, a measure of how efficiently sensible heat is transferred between the surface and the atmosphere and is given by $0.2 \times z_M$, the roughness length of momentum (Campbell and Norman, 1998). The value of z_M is dependent on friction velocity and sensible heat flux, which in turn are dependent on z_M and each other. Solving the equations requires an iterative optimization model. Full details on this calculation are provided in Supplementary Information (Appendix F).

If the target height lies within the canopy (e.g., inside a shrub), the MOST approach is not applicable (Bonan et al., 2021). Instead, we use Raupach's Localized Near-Field Theory (LNZT; Raupach, 1989b, 1989a), which predicts the distribution of heat and vapor within a canopy using Lagrangian theory. In this approach, the mean temperature is the sum of a diffusive far-field contribution, following MOST, and a non-diffusive near-field contribution from local sources (e.g., leaves), assuming locally homogeneous turbulence. For this calculation, the leaf temperature at the canopy top is assumed to be the LST derived from UAV data. Detailed derivations and assumptions are provided in Supplementary Information (Appendix F).

2.5. Comparison of modelling approaches for T_{13cm} and LST

Land surface temperature (LST) and near-surface temperature at 13 cm height (T_{13cm}) were compared among the three microclimate modelling approaches and evaluated against in situ measurements for flight block ANBH1 (Figure 1A). The surface temperature follows the vegetation structure, while T_{13cm} is fixed at a constant height above the ground (Figure 2). Pixels classified as water were excluded from the comparison as temperatures over water bodies fall out scope of this study. Comparing modelled T_{13cm} with in situ measurements is straightforward for all models and vegetation types, as both represent the same height. In contrast, comparing LST with in situ measurements is less direct. The T2 sensor of the TOMST TMS-4 loggers measures ground surface temperature (T_0), which is only comparable with *microclimf* and thermal UAV outputs for the landcover types "Sand" and "Moss". Microclimate temperatures (LST and T_{13cm}) were modelled or predicted for the four specific hours corresponding to the thermal UAV flights (Table 1).

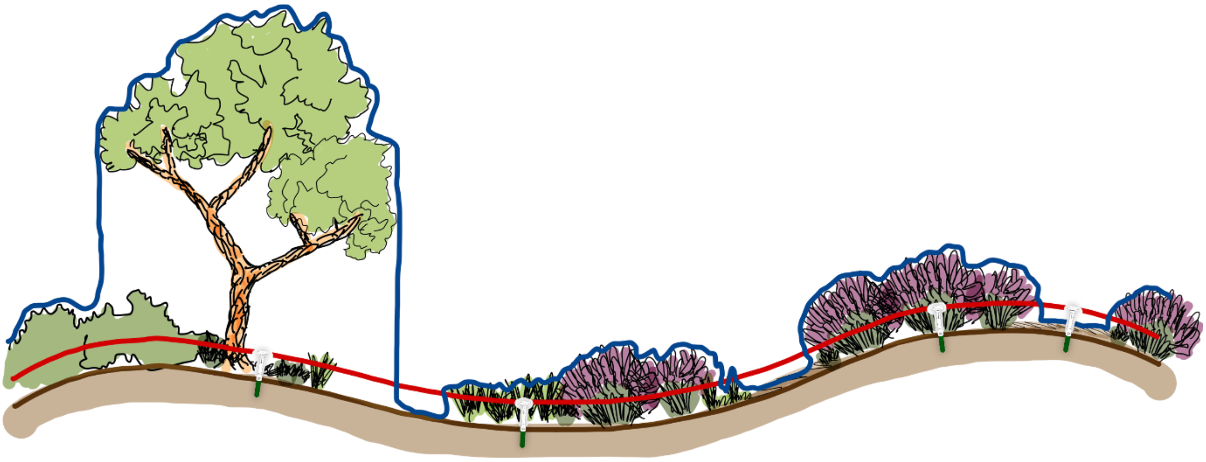

Figure 2. Conceptual visualization of the difference between land surface temperature and near-surface air temperature. *The land surface temperature (LST, in blue) follows the vegetation structure, providing information on what we can measure with thermal UAV data from above. The near-surface air temperature is measured with loggers at a fixed height above the ground, in this case 13 cm (T_{13cm}, in red).*

In this study, we established a logger network using TOMST TMS-4 loggers. At the time of field preparation, more accurate and robust thermocouple-based systems, such as SurveyTags (Concept

Shed), were still under development and therefore not available for deployment. The TMS-4 loggers are widely used in microclimate research, and their performance characteristics, limitations, and data-processing workflows are well documented in the literature. These loggers have a stated accuracy of ±0.50 °C (Wild et al., 2019), but are known to exhibit radiation-induced heating under high irradiance, which can lead to positive temperature biases under extreme conditions (Maclean et al., 2021). While acknowledging this limitation, we consider the spatial and temporal patterns observed in our ecosystem to exceed the expected magnitude of logger bias, particularly given the triple-shield setup. Logger performance is assumed reliable in shaded environments such as within heather shrubs, dense grasses, and beneath solitary or small trees, where direct radiative loading is reduced.

Nevertheless, even with shielding, positive temperature biases under high levels of direct solar radiation cannot be entirely excluded (Maclean et al., 2021). Consequently, the in situ measurements were treated as the best available reference, acknowledging that they do not represent a perfect or error-free representation of reality.

The three modelling approaches were evaluated against this reference using RMSE and the coefficient of determination (R^2), with pixel-level differences between modelled and measured temperatures, referred to as Δ, used to quantify over- or underestimation:

$$\Delta_{model} = T_{model} - T_{measured} \tag{2}$$

Additionally, to assess spatial variation within the models, sets of 50 random points per land cover class were generated. Microclimate temperatures from all three modelling approaches were extracted at these points.

3. Results

3.1. Measured and predicted temperature patterns

Daily minimum and maximum temperatures of T_{13cm} during the summer of 2024 are more extreme in open ecosystems compared to weather stations ($T_{Macroclimate}$), resulting in larger daily fluctuations (Figure 3). These fluctuations are further amplified under clear skies and high macroclimate temperatures (Flights 2 and 4). **Figure 3** also situates the dates of the UAV comparison flights within the study period, showing the different weather conditions for each flight. These trends are also visible in the microclimate offsets to macroclimate temperature (Appendix H).

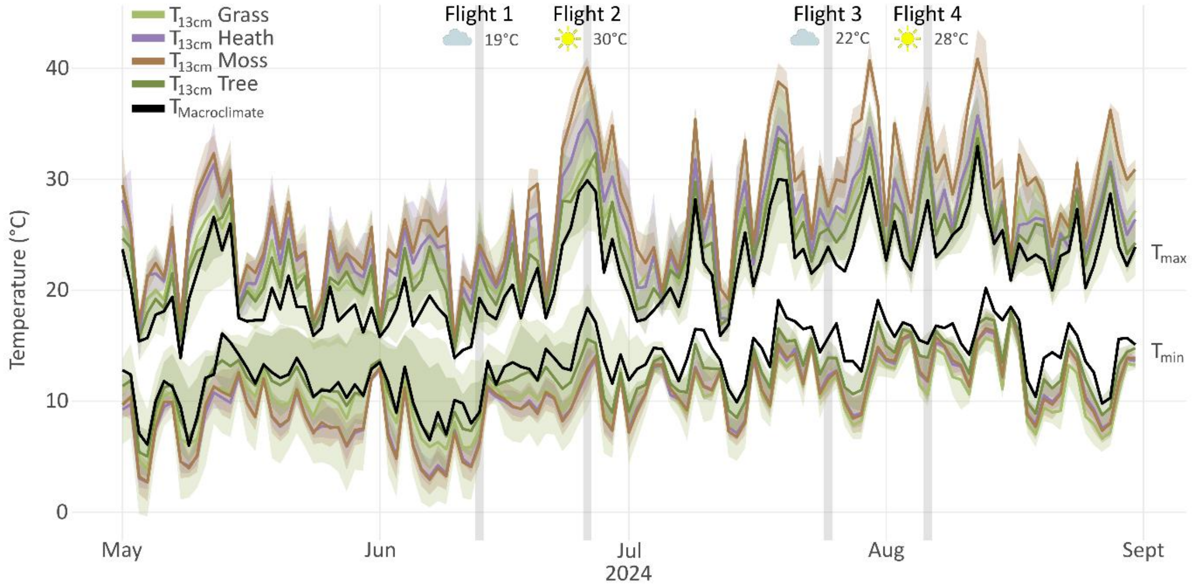

***Figure 3. Daily minimum and maximum micro- and macroclimate temperatures for the summer of 2024** within the focus area for the comparison (ANBH1, n = 30). The microclimate temperature measured at 13 cm (T_{13cm}) shows much higher extremes compared to the weather station, especially for open and sparse vegetation (e.g., mosses and heather shrubs). The dates for which the comparison is done are highlighted in grey, together with the weather conditions (derived from the in-situ Kestrel weather station) during the UAV flight.*

The maps with input variables derived from LiDAR and multispectral UAV data for flight block ANBH1 illustrate the highly heterogeneous landscape, with varying vegetation structures, slopes, and expositions, covering approximately 14 hectares (Figure 1B; Appendix D).

The final GBM models predicting T_{13cm} and T_{0cm} achieved RMSE values of 2.00 °C and 2.06 °C, respectively (Table E1). Macroclimate temperature was the most influential predictor in both models, accounting for 73.89% of the relative influence for T_{13cm} and 82.03% for T_{0cm}. Global shortwave radiation was the second most important variable (19.80% for T_{13cm}; 6.56% for T_{0cm}). Model-specific differences emerged for the remaining predictors: vegetation height ranked third for T_{0cm} (2.66%), whereas for T_{13cm}, longwave downwelling radiation (3.38%) and wind speed (0.42%) exceeded the influence of vegetation height (0.37%). The relative contributions of the remaining variables are provided in the Supplementary Materials (Appendix E).

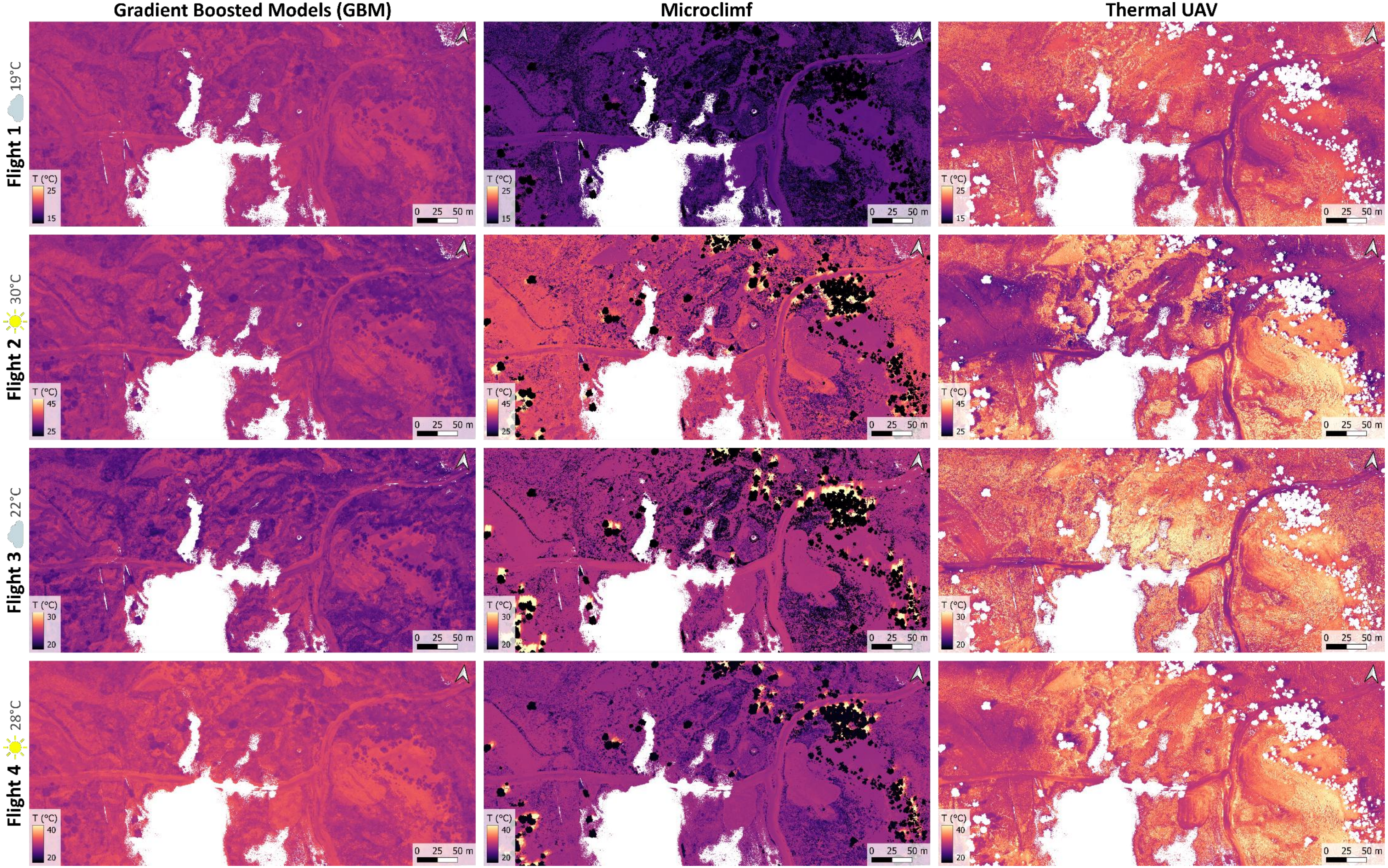

Figure 4. The modelled microclimate temperature at 13cm (T_{13cm}). *Each column presents the output of a different model (left: Gradient Boosted Model, GBM; middle: full mechanistic model, microclimf; right:* T_{13cm} *modelled from the land surface temperature derived with the thermal UAV data). Note the temperature range differs between the days, but is constant within a flight over the different models. Land cover classified as water is masked, as no reference data are available, and the thermal UAV approach also masks trees where the canopy height exceeds the reference height.*

The *microclimf* model generally predicts lower temperatures compared to the other two approaches (Figure 4). Areas under trees are notably cooler in the *microclimf* outputs relative to the GBM predictions. The thermal UAV approach predicts higher temperatures with a wider range within the study area. Modeled surface temperatures are provided in the Supplementary Materials (Figure A2).

3.2. Comparison for T_{13cm}

The differences (ΔT, equation (2)) between modelled T_{13cm} and measured temperatures for each land cover and flight are shown in Figure 5. Negative ΔT values indicate underestimation of the modelled temperatures relative to the measured temperatures, while positive ΔT values indicate overestimation. On hot, sunny days, ΔT varies more than on overcast days. The *microclimf* model tends to underestimate T_{13cm}, particularly for trees, while the thermal UAV approach generally overestimates T_{13cm} in all habitat types. The land cover class *Tree* is absent in the thermal UAV analysis, as the canopy height exceeds the reference height used to derive T_{13cm} from LST. Scatterplots of modelled vs. measured microclimate temperatures are available in the Supplementary Materials (0).

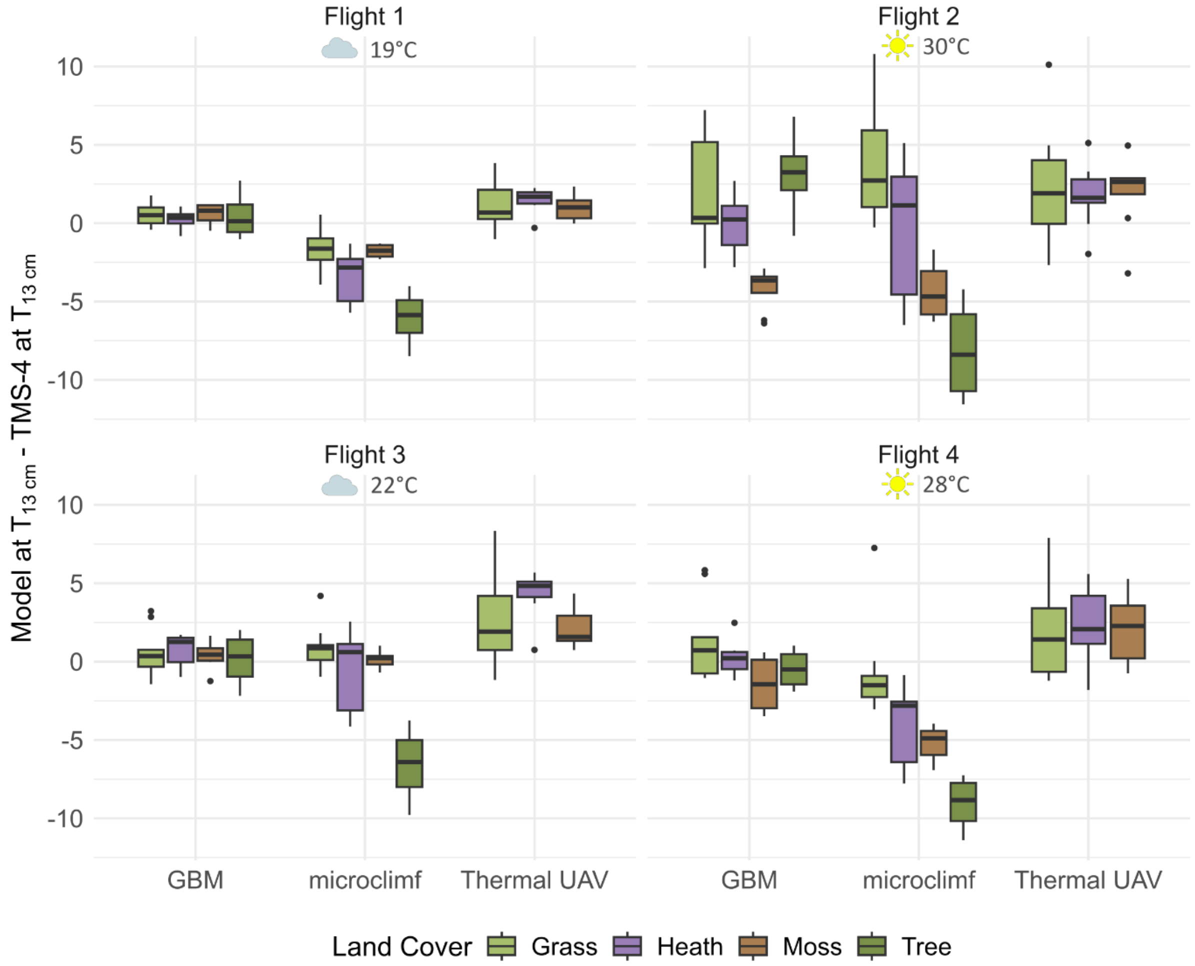

Figure 5. The difference between the model output and the corresponding measured microclimate for T_{13cm} *for the different models for the different flight days and presented by land cover class. For each flight, the weather conditions are given. Note, the land cover "Tree" was not available for the thermal UAV approach as the CHM exceeded the height of the reference weather station.*

In flight block ANBH1 (n = 30), across all land covers and flight days, the GBM model showed the lowest RMSE relative to the in situ logger measurements (2.22 °C), followed by the thermal UAV approach (3.37 °C) and *microclimf* (4.43 °C). The logger data are used here as a common reference for relative model comparison and are not interpreted as absolute ground truth (Section 2.5).

The modelled microclimate temperature T_{13cm} for 50 randomly selected points per land cover type shows a wide variation in T_{13cm} (Figure G1). Trends are consistent with the ΔT patterns: the thermal UAV approach predicts the highest temperatures, while *microclimf* generally predicts lower values, especially for trees. Extreme maximum temperatures predicted by the thermal approach exceeded 60 °C above moss during flight 2.

3.3. Comparison for LST

Differences between modelled output and measured land surface temperatures of the TMS-4 loggers (ΔT; equation (2)) could only be assessed for the land cover type *Moss* in area *ANBH1*. Discrepancies were generally larger than those observed for T_{13cm}, with the greatest differences and variability occurring on hot, sunny days (> 20 °C; Figure G2). Accordingly, RMSE values were higher and R^2 values lower for all models predicting surface temperature compared to T_{13cm} (Table G1).

Thermal UAV-derived LST consistently exceeded the predictions from both the GBM and mechanistic *microclimf* models for *Moss*, reaching extreme values of nearly 70 °C (Figure 6). In addition, the UAV-based approach exhibited greater variability, particularly over bare sandy areas. Under hot, sunny conditions with low wind speed and high direct solar radiation (flight 2), *microclimf* predicted higher LST for grass and heath than the other two approaches. In contrast, during the coldest and most overcast condition with the highest wind speed (flight 1; Table 1), *microclimf* predicted the lowest surface temperatures across all land cover types (Figure 6). For flight 3, *microclimf* produced an extreme surface temperature exceeding 50 °C for grass, which corresponded to spatial hotspots on the leeward side of trees in the model output (Figure 4).

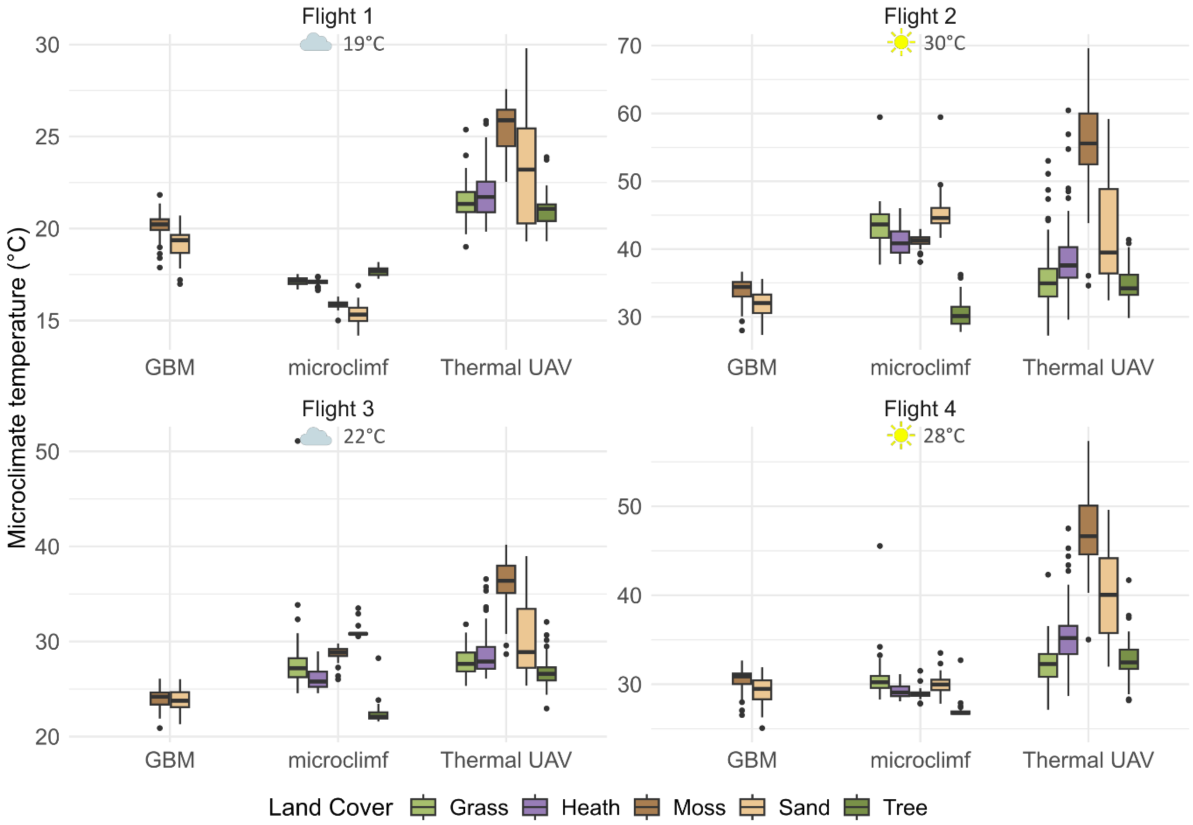

***Figure 6. The modelled microclimate land surface temperature (LST) for the different models** for each flight day derived from 50 random points per land cover class. Note only land covers “Sand” and “Moss” are shown for the GBM model as they represent the comparable surface.*

4. Discussion

4.1. Comparison of UAV-based methods for microclimate modelling

In this study, we compared three different UAV-based approaches for deriving microclimate temperature in an open heathland ecosystem: A gradient boosted model (GBM) trained temperature logger data, the mechanistic above- and below-canopy microclimate model, *microclimf* (Maclean, 2026), and thermal UAV data (Metsu et al., 2026). As thermal UAVs only provide land surface temperature (LST), we additionally evaluated how UAV-derived LST can be converted to near-surface air temperature to allow comparison with in situ TMS-4 loggers (Figure 2). We focused on both LST and near-surface temperature at a fixed height of 13 cm above ground (T_{13cm}).

Overall, the mechanistic *microclimf* model tended to predict lower temperatures compared to the GBM, whereas the thermal UAV approach consistently produced higher values. However, this contrast requires nuance. Rather than referring to systematic deviations as "bias," we quantified differences between model predictions and in situ measurements (ΔT) during four summer comparison periods in 2024. This terminology acknowledges that the triple-shielded loggers may themselves overestimate air temperature due to radiative heating and reduced ventilation within the shield (Maclean et al., 2021). Nevertheless, we assume that observed spatial and temporal variability exceeds the expected measurement error of the TOMST TMS-4 loggers. As expected, ΔT values for the GBM were centered around zero, given that the model was trained on the logger data.

The GBM predicting T_{13cm} achieved a high accuracy with an R^2 of 0.91 and an RMSE of 2.00 °C. Because we modelled absolute microclimate temperature rather than the temperature offset ($T_{micro} - T_{macro}$), the R^2 and RMSE values are not directly comparable to offset-based studies and are inherently higher, but remain in line with Haesen et al. (2021). The GBM predicting ground surface temperature (T_{0cm}) was slightly less accurate, yet still explained 84.8% of the variance (Table E1). Incorporating high-resolution soil moisture data may further improve predictive performance, given its buffering effect on microclimate temperatures (Greiser et al., 2024) and driving the efficiency of evapotranspirative cooling.

Microclimf predominantly underestimated T_{13cm} relative to the in situ measurements. This may partly reflect logger-related warming, but likely also stems from structural assumptions and parameter uncertainty within the model. We parameterized *microclimf* with site-specific adjustments such as leaf and soil reflectance derived from UAV-based multispectral measurements. However, the most influential predictor, plant area index (PAI), was estimated from NDVI. This could have resulted in overly dense canopy representations and excessive thermal buffering for shrubs and grasses. The model further relies on vegetation traits such as leaf angle distribution, characteristic leaf dimensions, clumping, and stomatal conductance, which are difficult and time-consuming to quantify accurately at this scale. A similar underestimation pattern was reported by Kolstela et al. (2024) under forest conditions using the same logger type. Our RMSE for *microclimf* (~4.4 °C for T_{13cm}) exceeds values reported in that study (≈3.5 °C for daily minima and maxima; ≈1.3 °C for daily means), and also those reported by MacLean (2026), with RMSE's of 1.1 and 0.7 °C for grasslands in Spain and the UK. The higher RMSE in our case likely reflects both the limited comparison window and the strong heterogeneity of land-cover types in the study area. The short evaluation period included high-radiation conditions and wind speeds, limiting temporal averaging and amplifying systematic model deviations. In addition, the presence of multiple heterogeneous land-cover types increased sensitivity to vegetation parameterization in *microclimf*. This effect is most evident beneath trees (Figure 4 and Figure **5**), where pixels were parameterized as evergreen needleleaf forest but in reality represented solitary or small tree patches, leading to substantial local underestimation. Conversely, wind-sheltered leeward areas showed local overestimation, producing extreme outliers when extracting random-point T_{13cm} and LST values (Figure 4, Figure **6**, Figure ***G1***). *Microclimf* performed best under overcast and windy conditions (Flight 3), that reduced the logger bias due to the absence of direct sunlight and good air mixing.

Thermal UAV–derived temperatures, both T_{13cm} and LST, were consistently higher than logger measurements (Figure 4-Figure **6**). Elevated LST over moss was expected, as mosses on inland sandy dunes typically have low water content, reducing evaporative cooling, and exhibit darker colors and relatively flat surfaces that enhance solar radiation absorption (Kim et al., 2025; Xiao and Bowker, 2020). Because this approach directly retrieves UAV-based LST and was corrected following state-of-the-art procedures (Metsu et al., 2026), it can be considered the most reliable for surface temperature estimation. In contrast, the T2 sensors of the TOMST TMS-4 loggers were in contact with the ground surface but north-facing, likely yielding systematically cooler readings than true LST. With an RMSE of ~3.3 °C across the four comparison days, conversion of LST to T_{13cm} generally produced values closer to the in situ measurements than *microclimf*. However, the land cover class *tree* could not be evaluated for the thermal UAV approach because the reference meteorological data were collected at a height lower than the tree canopy (Appendix F). Overestimation for grass and heather likely resulted from assumptions in ground temperature (T_G) estimation: when T_G is overestimated, vertical canopy temperature gradients are too weak, leading to inflated near-surface temperature predictions (Raupach, 1989a, 1989b). For moss, the LiDAR-derived canopy height model (CHM) values were frequently overestimated (7–8 cm versus ~1 cm actual height), distorting vertical temperature profiles; artificially constraining CHM to 0.01 m improved T_{13cm} predictions (Figure I1).

Soil data were resampled from 10 m to 10 cm resolution, likely missing fine-scale heterogeneity relevant for microclimate in the GBM and *microclimf* approach. In this study, we did not include soil moisture measurements. Although soil-specific calibration for the TOMST loggers is available following Wild et al. (2019), soil-moisture measurements remain more uncertain in well-drained sandy soils. These soils are typically characterized by low moisture contents, rapid drainage, and strong small-scale variability, which reduce sensor sensitivity and limit the representativeness of point-based soil moisture measurements (Ferrarezi et al., 2020; Robinson et al., 2008; Vaz et al., 2013).

4.2. Potential of UAV-derived variables for microclimate modelling

In this study, near-surface air temperature at 13 cm was successfully derived from thermal UAV data, demonstrating the potential of high-resolution thermal remote sensing for microclimate research beyond the analysis of land surface temperature patterns alone. This case study represents a first step towards integrating corrected UAV-derived LST (Metsu et al., 2026) with mechanistic microclimate modelling frameworks such as *microclimf* (Maclean, 2026).

Overall, the thermal UAV approach captured greater spatial heterogeneity and broader temperature ranges for both near-surface temperature and LST than the modelling approaches based on landscape metrics, vegetation parameters, or logger networks that do not resolve the full thermal range of the landscape. Thermal UAV data, therefore, represent a valuable addition to microclimate research, for example, for identifying landscape-scale hot and cold spots in the search for microrefugia (Hoffrén and García, 2023) or for assessing bark beetle impacts on forest canopy and understory temperatures (Greiser et al., 2025).

Despite the high spatial resolution and capacity to resolve fine-scale thermal heterogeneity, a key limitation of thermal UAV data remains its low temporal resolution. Alujević et al. (2025) addressed this constraint by developing the *throne* package, which links high-resolution thermal imagery with temporally dense in situ logger networks to generate continuous thermal landscapes throughout the measurement period. We evaluated this approach using the four UAV flight days available in our study (Supplementary Materials Appendix J). Although the limited number of thermal acquisitions precluded a robust statistical relationship between imagery and logger data, spatial patterns of relatively warmer and cooler areas were consistently reproduced. This framework, therefore, offers a promising pathway for temporally interpolating high-resolution land surface temperature maps, and by extension near-ground air temperatures derived from them, across time.

Both the *microclimf* model and the conversion of UAV-derived LST to near-surface temperature (T_{13cm}) strongly depend on estimates of PAI (Maclean, 2026). In this study, PAI was derived using a simple transformation between NDVI and PAI developed for shrubby tundra ecosystems (Juutinen et al., 2017). Although numerous studies have established robust relationships between satellite-derived NDVI and leaf or plant area index, the direct application of these relationships at very high spatial resolutions does not necessarily capture local vegetation structure accurately (Liu et al., 2025; Tian et al., 2025). While the resulting PAI values were broadly comparable to those used in *microclimf*, careful interpretation remains essential. Collecting reliable reference data for PAI at fine spatial scales is challenging, yet further validation of NDVI–PAI relationships for high-resolution UAV data is required to increase confidence in these estimates.

An alternative approach for deriving PAI is based on LiDAR data, for example using the ALS2PAD software where the number and intensity of LiDAR returns are related to vegetation density (Arnqvist et al., 2020). While this method has proven effective in forest and agricultural environments, its applicability in dense shrub systems at very high spatial resolutions is yet to be assessed (Kolstela et al., 2024; Wang et al., 2023; Yu et al., 2023). The accuracy of such an approach is also highly dependent on point cloud density (Watt et al., 2014). During our LiDAR processing, several heather-dominated areas lacked ground-classified points, indicating incomplete canopy penetration. This limitation highlights the difficulty of retrieving accurate PAI estimates in dense shrub and grassland ecosystems using our current LiDAR configuration.

Limited LiDAR penetration in dense shrub patches also affects the canopy height model (CHM) used in the analyses. When the laser signal does not fully reach the ground surface, canopy height can be underestimated. This issue is particularly relevant at very high spatial resolutions when trying to capture small-scale structural variability compared to studies using coarser-resolution airborne LiDAR data. Moreover, even small absolute errors in CHMs, on the order of a few centimeters, can substantially affect near-surface temperature estimates in open ecosystems, whereas similar errors are negligible in forest systems. In moss-dominated areas, for example, canopy height can easily be overestimated due to the presence of isolated grass stems, sensor inaccuracy and processing algorithms, resulting in inflated height estimates relative to the 13 cm level of interest, substantially influencing the derived vertical temperature profiles (Figure I1).

Working with high-resolution UAV data introduces an additional challenge related to the spatial alignment of multiple geospatial layers. Despite the use of real-time kinematic corrections and permanently installed ground control points, precise co-registration of UAV products from different sensors and flight dates remains difficult. The effect of misalignments becomes particularly evident at sharp thermal and structural gradients, such as transitions between dense heather shrubs and hot moss or bare soil patches. Even small positional offsets of a few pixels can substantially affect temperature estimates. For instance, when a high LST value from a dry moss pixel is combined with a neighboring shrub CHM that exceeds the height of interest, the resulting temperature profile may be strongly distorted. This effect is visible in the spatial T_{13cm} maps derived from LST, where elevated values occur adjacent to shrub patches (Figure 4). When integrating multiple UAV-derived datasets at very high spatial resolutions, it is therefore essential to carefully consider potential spatial mismatches, particularly when these exceed the ground sampling distance of the data.

4.3. Insights in microclimate conditions in open ecosystems

Microclimate temperatures measured with the TOMST loggers exhibited pronounced temporal and spatial variation. Daily maximum and minimum T_{13cm} were consistently higher and lower, respectively, than macroclimate temperatures (Figure 3), resulting in larger diurnal ranges across all land covers. This contrast was most pronounced in open areas such as moss-covered sandy soils, where full exposure to direct solar radiation led to near-surface temperatures up to 10 °C warmer than those recorded at the weather station during hot summer days (Figure H1). Even in locations not receiving direct sunlight (e.g., beneath solitary trees or within heather shrubs), mean daily maximum temperature offsets exceeded 5 °C. Although solitary trees provide substantial buffering closer to their canopies, they do not generate the same buffering capacity as closed forest canopies near the ground surface (Haesen et al., 2021; Van den Bossche et al., 2025). Under stable atmospheric conditions (low wind speed) and high incoming shortwave radiation, near-surface microclimate temperatures beneath solitary trees and dense grasses was occasionally lower compared to the macroclimate, likely due to limited turbulent mixing (Flight 2, Figure H2). At night, minimum microclimate temperatures were consistently lower than macroclimate temperatures (Figure 3). Under clear night skies and stable conditions, enhanced radiative cooling can rapidly decrease near-surface temperatures (Sun et al., 2017), resulting in nocturnal minima more than 5 °C below macroclimate values.

For heathland, maximum T_{13cm} measured by in situ loggers and derived from the thermal UAV approach were generally higher than in adjacent grassland patches (Figure 3; Figure G1). Two mechanisms likely contribute to this pattern: (1) the spatially heterogeneous structure of heathland, where variation in heather age produces a mosaic of vegetation structures and openness with differing levels of radiative penetration, and (2) the shallow rooting system of *Calluna vulgaris*, which limits water uptake compared to *Molinia caerulea*, whose roots can exceed 1 m depth and facilitate stronger transpirative cooling in grassland patches (Genney et al., 2002; Jacquemyn et al., 2005). This mechanism is consistent with slightly higher canopy surface temperatures observed for heather shrubs relative to grasses on sunny days in the thermal UAV data (Figure 6).

The highly heterogeneous landscape structure generated temperature differences of several degrees over distances of only a few meters for T_{13cm} (Figure 4), and differences of several tens of degrees for land surface temperature (Figure A2). This pattern aligns with previously reported high thermal variability in open systems compared to forested environments at high latitudes (Aalto et al., 2022).

Variable importance analyses (Figures Figure ***E3***, Figure ***E4***) showed that, after macroclimate temperature, incoming global radiation was the most influential predictor. This aligns with Aalto et al., (2022), who identified topographic solar radiation as a key factor in tundra microclimate. The canopy height model (CHM) was the strongest vegetation-related predictor for both ground surface temperature (T_{0cm}) and near-surface temperature (T_{13cm}), reflecting its influence on shading, vegetation structure, and wind patterns. For near-surface temperature, wind speed also contributed substantially, consistent with enhanced turbulent mixing under higher wind conditions. Solar altitude influenced ground surface temperatures by regulating the angle of incidence and capturing the diurnal radiation cycle, with peak inputs around solar noon. North- and east-facing slopes were generally cooler, as reflected in the predicted GBM maps (Figure 4). At the spatial resolution of this study, the topographic position index (TPI) had limited influence, suggesting that cold-air pooling effects or moisture accumulation were not strongly expressed at this scale.

5. Conclusion

Open heathland ecosystems exhibit meter-scale thermal mosaics that standard weather stations cannot resolve. By comparing three UAV-based modelling approaches: a correlative GBM, the mechanistic model *microclimf*, and thermal UAV observations with physically-based conversion of land surface temperature to near-surface air temperature, we show that each approach captures complementary aspects of microclimate. GBM excels in accuracy relative to dense logger networks, *microclimf* provides physically interpretable profiles but is sensitive to parameterization, and thermal UAVs uniquely reveal extremes and sharp transitions with ecological significance.

Across four flights spanning clear and overcast conditions, GBM yielded the lowest $T_{13\,cm}$ error (RMSE = 2.22 °C), while LST-based products resolved the broadest spatial ranges and detected extreme heating over dry moss (> 60 °C). *Microclimf* generally predicted cooler values, especially beneath trees, reflecting structural assumptions and input uncertainty. These systematic differences are explainable by physics, parameter sensitivities, and sub-decimeter co-registration at canopy–ground boundaries.

We present a workflow for integrating corrected UAV thermal data into microclimate modelling, demonstrating that surface measurements can be converted to ecologically relevant air temperatures and directly compared with in situ observations. This approach enables integrated monitoring in open ecosystems, where thermal data capture fine-scale variability and can serve as input for mechanistic approaches.

Future work should prioritize thermocouple-based validation under high-radiation conditions, refined retrievals of PAI and canopy height in shrubs and grasses, and temporal upscaling to link sparse UAV flights with continuous logger networks or the *microclimf* framework. Together, these steps will produce operational, high-resolution microclimate products that better represent the conditions organisms actually experience in open ecosystems.

Acknowledgements

We are grateful to the Agency for Nature and Forests of Belgium (ANB) for granting us permission to conduct UAV operations in this beautiful nature reserve. A special thank you to terrain manager Jef De Winter for showing us around in the reserve and communication and updates throughout the field campaign.

Declaration of Generative AI

During the preparation of this work the lead author used Microsoft 365 Copilot in order to improve the readability and language of the manuscript. After using this tool, the author reviewed and edited the content as needed and takes full responsibility for the content of the publication.

Funding

This study was funded by the Internal Funds of KU Leuven (MICROMICS project; C14/22/067).

Data Availability

Data is available on figshare: https://doi.org/10.6084/m9.figshare.32077611

6. References

Aalto, J., Tyystjärvi, V., Niittynen, P., Kemppinen, J., Rissanen, T., Gregow, H., Luoto, M., 2022. Microclimate temperature variations from boreal forests to the tundra. Agric. For. Meteorol. 323. https://doi.org/10.1016/j.agrformet.2022.109037

Agisoft, 2024. MicaSense Altum processing workflow (including Reflectance Calibration) in Agisoft Metashape Professional [WWW Document]. URL https://agisoft.freshdesk.com/support/solutions/articles/31000148381-micasense-altum-processing-workflow-including-reflectance-calibration-in-agisoft-metashape-professi

Agisoft, 2022. Agisoft Metashape.

Alujević, K., Garcia-Costoya, G., Ratia, N., Schmitz, E., Godkin, R.S., Gopal, A.C., Bujan, J., Logan, M.L., 2025. Using aerial thermography to map terrestrial thermal environments in unprecedented detail. Methods Ecol. Evol. 16, 1688–1702. https://doi.org/10.1111/2041-210X.70096

Andriambololonaharisoamalala, R., Helmholz, P., Ivánová, I., Jones, E., Soon, S., Bulatov, D., Song, Y., 2025. Enhancing the spatial and temporal resolution of satellite-derived land surface temperature in urban environments: A systematic literature review. Urban Clim. 60, 102345. https://doi.org/10.1016/j.uclim.2025.102345

Applanix, 2023. POSPac MMs 8.9.

Arnqvist, J., Freier, J., Dellwik, E., 2020. Robust processing of airborne laser scans to plant area density profiles. Biogeosciences 17, 5939–5952. https://doi.org/10.5194/bg-17-5939-2020

Baker, E., Harper, A.B., Williamson, D., Challenor, P., 2022. Emulation of high-resolution land surface models using sparse Gaussian processes with application to JULES. Geosci. Model Dev. 15, 1913–1929. https://doi.org/10.5194/gmd-15-1913-2022

Bonan, G.B., Patton, E.G., Finnigan, J.J., Baldocchi, D.D., Harman, I.N., 2021. Moving beyond the incorrect but useful paradigm: reevaluating big-leaf and multilayer plant canopies to model biosphere-atmosphere fluxes – a review. Agric. For. Meteorol. 306, 108435. https://doi.org/10.1016/j.agrformet.2021.108435

Bramer, I., Anderson, B.J., Bennie, J., Bladon, A.J., De Frenne, P., Hemming, D., Hill, R.A., Kearney, M.R., Körner, C., Korstjens, A.H., Lenoir, J., Maclean, I.M.D., Marsh, C.D., Morecroft, M.D., Ohlemüller, R., Slater, H.D., Suggitt, A.J., Zellweger, F., Gillingham, P.K., 2018. Advances in Monitoring and Modelling Climate at Ecologically Relevant Scales. pp. 101–161. https://doi.org/10.1016/bs.aecr.2017.12.005

Campbell, G.S., Norman, J.M., 1998. An Introduction to Environmental Biophysics. Springer New York, New York, NY. https://doi.org/10.1007/978-1-4612-1626-1

Davis, F.W., Synes, N.W., Fricker, G.A., McCullough, I.M., Serra-Diaz, J.M., Franklin, J., Flint, A.L., 2019. LiDAR-derived topography and forest structure predict fine-scale variation in daily surface temperatures in oak savanna and conifer forest landscapes. Agric. For. Meteorol. 269–270, 192–202. https://doi.org/10.1016/j.agrformet.2019.02.015

De Frenne, P., Beugnon, R., Klinges, D., Lenoir, J., Niittynen, P., Pincebourde, S., Senior, R.A., Aalto, J., Chytrý, K., Gillingham, P.K., Greiser, C., Gril, E., Haesen, S., Kearney, M., Kopecký, M., le Roux, P.C., Luoto, M., Maclean, I., Man, M., Penczykowski, R., van den Brink, L., Van de Vondel, S., De Pauw, K., Lembrechts, J.J., Kemppinen, J., Van Meerbeek, K., 2025. Ten practical guidelines for microclimate research in terrestrial ecosystems. Methods Ecol. Evol. 16, 269–294. https://doi.org/10.1111/2041-210X.14476

De Frenne, P., Lenoir, J., Luoto, M., Scheffers, B.R., Zellweger, F., Aalto, J., Ashcroft, M.B., Christiansen, D.M., Decocq, G., Pauw, K. De, Govaert, S., Greiser, C., Gril, E., Hampe, A., Jucker, T., Klinges, D.H., Koelemeijer, I.A., Lembrechts, J.J., Marrec, R., Meeussen, C., Ogée, J., Tyystjärvi, V., Vangansbeke, P., Hylander, K., 2021. Forest microclimates and climate change: Importance, drivers and future research agenda. Glob. Chang. Biol. 27, 2279–2297. https://doi.org/10.1111/gcb.15569

De Frenne, P., Rodríguez-Sánchez, F., Coomes, D.A., Baeten, L., Verstraeten, G., Vellend, M., Bernhardt-Römermann, M., Brown, C.D., Brunet, J., Cornelis, J., Decocq, G.M., Dierschke, H., Eriksson, O., Gilliam, F.S., Hédl, R., Heinken, T., Hermy, M., Hommel, P., Jenkins, M.A., Kelly, D.L., Kirby, K.J., Mitchell, F.J.G., Naaf, T., Newman, M., Peterken, G., Petřík, P., Schultz, J., Sonnier, G., Van Calster, H., Waller, D.M., Walther, G.-R., White, P.S., Woods, K.D., Wulf, M., Graae, B.J., Verheyen, K., 2013. Microclimate moderates plant responses to macroclimate warming. Proceedings of the National Academy of Sciences 110, 18561–18565. https://doi.org/10.1073/pnas.1311190110

Elith, J., Leathwick, J.R., Hastie, T., 2008. A working guide to boosted regression trees. Journal of Animal Ecology 77, 802–813. https://doi.org/10.1111/j.1365-2656.2008.01390.x

Evans, J.S., 2023. spatialEco: Spatial Analysis and Modelling Utilities. https://doi.org/10.32614/CRAN.package.spatialEco

Ferrarezi, R.S., Nogueira, T.A.R., Zepeda, S.G.C., 2020. Performance of Soil Moisture Sensors in Florida Sandy Soils. Water (Basel). 12, 358. https://doi.org/10.3390/w12020358

Fick, S.E., Hijmans, R.J., 2017. WorldClim 2: new 1-km spatial resolution climate surfaces for global land areas. International Journal of Climatology 37, 4302–4315. https://doi.org/10.1002/joc.5086

Foken, T., 2006. 50 Years of the Monin–Obukhov Similarity Theory. Boundary. Layer. Meteorol. 119, 431–447. https://doi.org/10.1007/s10546-006-9048-6

Gardner, A.S., Maclean, I.M.D., Gaston, K.J., 2019. Climatic predictors of species distributions neglect biophysiologically meaningful variables. Divers. Distrib. 25, 1318–1333. https://doi.org/10.1111/ddi.12939

Genney, D.R., Alexander, I.J., Hartley, S.E., 2002. Soil organic matter distribution and below-ground competition between *Calluna vulgaris* and *Nardus stricta*. Funct. Ecol. 16, 664–670. https://doi.org/10.1046/j.1365-2435.2002.00667.x

Greiser, C., Ehrlén, J., Meineri, E., Hylander, K., 2020. Hiding from the climate: Characterizing microrefugia for boreal forest understory species. Glob. Chang. Biol. 26, 471–483. https://doi.org/10.1111/gcb.14874

Greiser, C., Hederová, L., Vico, G., Wild, J., Macek, M., Kopecký, M., 2024. Higher soil moisture increases microclimate temperature buffering in temperate broadleaf forests. Agric. For. Meteorol. 345. https://doi.org/10.1016/j.agrformet.2023.109828

Greiser, C., Huo, L., Ghaly, M., Brown, I., Metsu, C., Van Meerbeek, K., Lehmann, P., 2025. Bark beetles as microclimate engineers – thermal characteristics of infested spruce trees at the canopy surface and below the canopy. Agric. For. Meteorol. 375, 110796. https://doi.org/10.1016/j.agrformet.2025.110796

Gril, E., Spicher, F., Greiser, C., Ashcroft, M.B., Pincebourde, S., Durrieu, S., Nicolas, M., Richard, B., Decocq, G., Marrec, R., Lenoir, J., 2023. Slope and equilibrium: A parsimonious and flexible approach to model microclimate. Methods Ecol. Evol. 14, 885–897. https://doi.org/10.1111/2041-210X.14048

Haesen, S., Lembrechts, J.J., Frenne, P. De, Lenoir, J., Aalto, J., Ashcroft, M.B., Kopecký, M., Luoto, M., Maclean, I., Nijs, I., Niittynen, P., van den Hoogen, J., Arriga, N., Brůna, J., Buchmann, N., Čiliak, M., Collalti, A., Lombaerde, E. De, Descombes, P., Gharun, M., Goded, I., Govaert, S., Greiser, C., Grelle, A., Gruening, C., Hederová, L., Hylander, K., Kreyling, J., Kruijt, B., Macek, M., Máliš, F., Man, M., Manca, G., Matula, R., Meeussen, C., Merinero, S., Minerbi, S., Montagnani, L., Muffler, L., Ogaya, R., Penuelas, J., Plichta, R., Portillo-Estrada, M., Schmeddes, J., Shekhar, A., Spicher, F., Ujházyová, M., Vangansbeke, P., Weigel, R., Wild, J., Zellweger, F., Meerbeek, K. Van, 2021. ForestTemp – Sub-canopy microclimate temperatures of European forests. Glob. Chang. Biol. 27, 6307–6319. https://doi.org/10.1111/gcb.15892

Haesen, S., Lenoir, J., Gril, E., De Frenne, P., Lembrechts, J.J., Kopecký, M., Macek, M., Man, M., Wild, J., Van Meerbeek, K., 2023. Microclimate reveals the true thermal niche of forest plant species. Ecol. Lett. 26, 2043–2055. https://doi.org/10.1111/ele.14312

Hijmans, R.J., 2025. terra: Spatial Data Analysis. https://doi.org/10.32614/CRAN.package.terra

Hoffrén, R., García, M.B., 2023. Thermal unmanned aerial vehicles for the identification of microclimatic refugia in topographically complex areas. Remote Sens. Environ. 286. https://doi.org/10.1016/j.rse.2022.113427

Ilich, A.R., Misiuk, B., Lecours, V., Murawski, S.A., 2023. MultiscaleDTM: An open-source R package for multiscale geomorphometric analysis. Transactions in GIS 27, 1164–1204. https://doi.org/10.1111/tgis.13067

Jacquemyn, H., Brys, R., Neubert, M.G., 2005. FIRE INCREASES INVASIVE SPREAD OF MOLINIA CAERULEA MAINLY THROUGH CHANGES IN DEMOGRAPHIC PARAMETERS. Ecological Applications 15, 2097–2108. https://doi.org/10.1890/04-1762

Juutinen, S., Virtanen, T., Kondratyev, V., Laurila, T., Linkosalmi, M., Mikola, J., Nyman, J., Räsänen, A., Tuovinen, J.-P., Aurela, M., 2017. Spatial variation and seasonal dynamics of leaf-area index in the arctic tundra-implications for linking ground observations and satellite images. Environmental Research Letters 12, 095002. https://doi.org/10.1088/1748-9326/aa7f85

Kearney, M.R., Gillingham, P.K., Bramer, I., Duffy, J.P., Maclean, I.M.D., 2020. A method for computing hourly, historical, terrain-corrected microclimate anywhere on earth. Methods Ecol. Evol. 11, 38–43. https://doi.org/10.1111/2041-210X.13330

Kemppinen, J., Lembrechts, J.J., Van Meerbeek, K., Carnicer, J., Chardon, N.I., Kardol, P., Lenoir, J., Liu, D., Maclean, I., Pergl, J., Saccone, P., Senior, R.A., Shen, T., Słowińska, S., Vandvik, V., von Oppen, J., Aalto, J., Ayalew, B., Bates, O., Bertelsmeier, C., Bertrand, R., Beugnon, R., Borderieux, J., Brůna, J., Buckley, L., Bujan, J., Casanova-Katny, A., Christiansen, D.M., Collart, F., De Lombaerde, E., De Pauw, K., Depauw, L., Di Musciano, M., Díaz Borrego, R., Díaz-Calafat, J., Ellis-Soto, D., Esteban, R., de Jong, G.F., Gallois, E., Garcia, M.B., Gillerot, L., Greiser, C., Gril, E., Haesen, S., Hampe, A., Hedwall, P.O., Hes, G., Hespanhol, H., Hoffrén, R., Hylander, K., Jiménez-Alfaro, B., Jucker, T., Klinges, D., Kolstela, J., Kopecký, M., Kovács, B., Maeda, E.E., Máliš, F., Man, M., Mathiak, C., Meineri, E., Naujokaitis-Lewis, I., Nijs, I., Normand, S., Nuñez, M., Orczewska, A., Peña-Aguilera, P., Pincebourde, S., Plichta, R., Quick, S., Renault, D., Ricci, L., Rissanen, T., Segura-Hernández, L., Selvi, F., Serra-Diaz, J.M., Soifer, L., Spicher, F., Svenning, J.C., Tamian, A., Thomaes, A., Thoonen, M., Trew, B., Van de Vondel, S., van den Brink, L., Vangansbeke, P., Verdonck, S., Vitkova, M., Vives-Ingla, M., von Schmalensee, L., Wang, R., Wild, J., Williamson, J., Zellweger, F., Zhou, X., Zuza, E.J., De Frenne, P., 2024. Microclimate, an important part of ecology and biogeography. Global Ecology and Biogeography 33. https://doi.org/10.1111/geb.13834

Kim, S., Dinh, T.-V., Park, B.-G., Lee, S.-W., Jung, K., Chung, H., Kim, J.-C., 2025. A Study on a New Moss for Moss-Based Green Roofs in Roof Surface Temperature Mitigation and Carbon Capture. Atmosphere (Basel). 16, 1277. https://doi.org/10.3390/atmos16111277

Klinges, D.H., Baecher, J.A., Lembrechts, J.J., Maclean, I.M.D., Lenoir, J., Greiser, C., Ashcroft, M., Evans, L.J., Kearney, M.R., Aalto, J., Barrio, I.C., 2024. Proximal microclimate : Moving beyond spatiotemporal resolution improves ecological predictions 1–16. https://doi.org/10.1111/geb.13884

Kolstela, J., Aakala, T., Maclean, I., Niittynen, P., Kemppinen, J., Luoto, M., Rissanen, T., Tyystjärvi, V., Gregow, H., Vapalahti, O., Aalto, J., 2024. Revealing fine-scale variability in boreal forest temperatures using a mechanistic microclimate model. Agric. For. Meteorol. 350, 109995. https://doi.org/10.1016/j.agrformet.2024.109995

Kuhn, M., 2008. Building Predictive Models in R Using the caret Package. J. Stat. Softw. 28. https://doi.org/10.18637/jss.v028.i05

Lembrechts, J.J., Lenoir, J., R. Scheffers, B., De Frenne, P., 2021. Designing countrywide and regional microclimate networks. Global Ecology and Biogeography 30, 1168–1174. https://doi.org/10.1111/geb.13290

Lembrechts, J.J., Nijs, I., Lenoir, J., 2019. Incorporating microclimate into species distribution models. Ecography 42, 1267–1279. https://doi.org/10.1111/ecog.03947

Lembrechts, J.J., van den Hoogen, J., Aalto, J., Ashcroft, M.B., Frenne, P. De, Kemppinen, J., Kopecký, M., Luoto, M., Maclean, I.M.D., Crowther, T.W., Bailey, J.J., Haesen, S., Klinges, D.H., Niittynen, P., Scheffers, B.R., Meerbeek, K. Van, Aartsma, P., Abdalaze, O., Abedi, M., Aerts, R., Ahmadian, N., Ahrends, A., Alatalo, J.M., Alexander, J.M., Allonsius, C.N., Altman, J., Ammann, C., Andres, C., Andrews, C., Ardö, J., Arriga, N., Arzac, A., Aschero, V., Assis, R.L., Assmann, J.J., Bader, M.Y., Bahalkeh, K., Barančok, P., Barrio, I.C., Barros, A., Barthel, M., Basham, E.W., Bauters, M., Bazzichetto, M., Marchesini, L.B., Bell, M.C., Benavides, J.C., Alonso, J.L.B., Berauer, B.J., Bjerke, J.W., Björk, R.G., Björkman, M.P., Björnsdóttir, K., Blonder, B., Boeckx, P., Boike, J., Bokhorst, S., Brum, B.N.S., Brůna, J., Buchmann, N., Buysse, P., Camargo, J.L., Campoe, O.C., Candan, O., Canessa, R., Cannone, N., Carbognani, M., Carnicer, J., Casanova-Katny, A., Cesarz, S., Chojnicki, B., Choler, P., Chown, S.L., Cifuentes, E.F., Čiliak, M., Contador, T., Convey, P., Cooper, E.J., Cremonese, E., Curasi, S.R., Curtis, R., Cutini, M., Dahlberg, C.J., Daskalova, G.N., de Pablo, M.A., Chiesa, S. Della, Dengler, J., Deronde, B., Descombes, P., Cecco, V. Di, Musciano, M. Di, Dick, J., Dimarco, R.D., Dolezal, J., Dorrepaal, E., Dušek, J., Eisenhauer, N., Eklundh, L., Erickson, T.E., Erschbamer, B., Eugster, W., Ewers, R.M., Exton, D.A., Fanin, N., Fazlioglu, F., Feigenwinter, I., Fenu, G., Ferlian, O., Calzado, M.R.F., Fernández-Pascual, E., Finckh, M., Higgens, R.F., Forte, T.G.W., Freeman, E.C., Frei, E.R., Fuentes-Lillo, E., García, R.A., García, M.B., Géron, C., Gharun, M., Ghosn, D., Gigauri, K., Gobin, A., Goded, I., Goeckede, M., Gottschall, F., Goulding, K., Govaert, S., Graae, B.J., Greenwood, S., Greiser, C., Grelle, A., Guénard, B., Guglielmin, M., Guillemot, J., Haase, P., Haider, S., Halbritter, A.H., Hamid, M., Hammerle, A., Hampe, A., Haugum, S. V, Hederová, L., Heinesch, B., Helfter, C., Hepenstrick, D., Herberich, M., Herbst, M., Hermanutz, L., Hik, D.S., Hoffrén, R., Homeier, J., Hörtnagl, L., Høye, T.T., Hrbacek, F., Hylander, K., Iwata, H., Jackowicz-Korczynski, M.A., Jactel, H., Järveoja, J., Jastrzębowski, S., Jentsch, A., Jiménez, J.J., Jónsdóttir, I.S., Jucker, T., Jump, A.S., Juszczak, R., Kanka, R., Kašpar, V., Kazakis, G., Kelly, J., Khuroo, A.A., Klemedtsson, L., Klisz, M., Kljun, N., Knohl, A., Kobler, J., Kollár, J., Kotowska, M.M., Kovács, B., Kreyling, J., Lamprecht, A., Lang, S.I., Larson, C., Larson, K., Laska, K., le Maire, G., Leihy, R.I., Lens, L., Liljebladh, B., Lohila, A., Lorite, J., Loubet, B., Lynn, J., Macek, M., Mackenzie, R., Magliulo, E., Maier, R., Malfasi, F., Máliš, F., Man, M., Manca, G., Manco, A., Manise, T., Manolaki, P., Marciniak, F., Matula, R., Mazzolari, A.C., Medinets, S., Medinets, V., Meeussen, C., Merinero, S., de Cássia Guimarães Mesquita, R., Meusburger, K., Meysman, F.J.R., Michaletz, S.T., Milbau, A., Moiseev, D., Moiseev, P., Mondoni, A., Monfries, R., Montagnani, L., Moriana-Armendariz, M., di Cella, U.M., Mörsdorf, M., Mosedale, J.R., Muffler, L., Muñoz-Rojas, M., Myers, J.A., Myers-Smith, I.H., Nagy, L., Nardino, M., Naujokaitis-Lewis, I., Newling, E., Nicklas, L., Niedrist, G., Niessner, A., Nilsson, M.B., Normand, S., Nosetto, M.D., Nouvellon, Y., Nuñez, M.A., Ogaya, R., Ogée, J., Okello, J., Olejnik, J., Olesen, J.E., Opedal, Ø.H., Orsenigo, S., Palaj, A., Pampuch, T., Panov, A. V, Pärtel, M., Pastor, A., Pauchard, A., Pauli, H., Pavelka, M., Pearse, W.D., Peichl, M., Pellissier, L., Penczykowski, R.M., Penuelas, J., Bon, M.P., Petraglia, A., Phartyal, S.S., Phoenix, G.K., Pio, C., Pitacco, A., Pitteloud, C., Plichta, R., Porro, F., Portillo-Estrada, M., Poulenard, J., Poyatos, R., Prokushkin, A.S., Puchalka, R., Pușcaș, M., Radujković, D., Randall, K., Backes, A.R., Remmele, S., Remmers, W., Renault, D., Risch, A.C., Rixen, C., Robinson, S.A., Robroek, B.J.M., Rocha, A. V, Rossi, C., Rossi, G., Roupsard, O., Rubtsov, A. V, Saccone, P., Sagot, C., Bravo, J.S., Santos, C.C., Sarneel, J.M., Scharnweber, T., Schmeddes, J., Schmidt, M., Scholten, T., Schuchardt, M., Schwartz, N., Scott, T., Seeber, J., de Andrade, A.C.S., Seipel, T., Semenchuk, P., Senior, R.A., Serra-Diaz, J.M., Sewerniak, P., Shekhar, A., Sidenko, N. V, Siebicke, L., Collier, L.S., Simpson, E., Siqueira, D.P., Sitková, Z., Six, J., Smiljanic, M., Smith, S.W., Smith-Tripp, S., Somers, B., Sørensen, M.V., Souza, J.J.L.L., Souza, B.I., Dias, A.S., Spasojevic, M.J., Speed, J.D.M., Spicher, F., Stanisci, A., Steinbauer, K., Steinbrecher, R., Steinwandter, M., Stemkovski, M., Stephan, J.G., Stiegler, C., Stoll, S., Svátek, M., Svoboda, M., Tagesson, T., Tanentzap, A.J., Tanneberger, F., Theurillat, J.P., Thomas, H.J.D., Thomas, A.D., Tielbörger, K., Tomaselli, M., Treier, U.A., Trouillier, M., Turtureanu, P.D., Tutton, R., Tyystjärvi, V.A., Ueyama, M., Ujházy, K., Ujházyová, M., Uogintas, D., Urban, A. V, Urban, J., Urbaniak, M., Ursu, T.M., Vaccari, F.P., de Vondel, S. Van, van den Brink, L., Geel, M. Van, Vandvik, V., Vangansbeke, P., Varlagin, A., Veen, G.F., Veenendaal, E., Venn, S.E., Verbeeck, H., Verbrugggen, E., Verheijen, F.G.A., Villar, L., Vitale, L., Vittoz, P., Vives-Ingla, M., von Oppen, J., Walz, J., Wang, R., Wang, Y., Way, R.G., Wedegärtner, R.E.M., Weigel, R., Wild, J., Wilkinson, M., Wilmking, M., Wingate, L., Winkler, M., Wipf, S., Wohlfahrt, G., Xenakis, G., Yang, Y., Yu, Z., Yu, K., Zellweger, F., Zhang, J., Zhang, Z., Zhao, P., Ziemblińska, K., Zimmermann, R., Zong, S., Zyryanov, V.I., Nijs, I., Lenoir, J., 2022. Global maps of soil temperature. Glob. Chang. Biol. 28, 3110–3144. https://doi.org/10.1111/gcb.16060

Lenoir, J., Hattab, T., Pierre, G., 2017. Climatic microrefugia under anthropogenic climate change: implications for species redistribution. Ecography 40, 253–266. https://doi.org/10.1111/ecog.02788

Liu, M., Yu, W., Li, D., Shang, F., Zhang, L., Wang, S., Yang, W., Zhao, R., Wang, X., 2025. Validation of Multi-Scale LAI Products in Heterogeneous Terrain-Based UAV Images. Remote Sens. (Basel). 17, 3393. https://doi.org/10.3390/rs17193393

Maclean, I.M.D., 2026. Microclimf: Fast modelling of microclimate across real landscapes in R. Methods Ecol. Evol. https://doi.org/10.1111/2041-210x.70253

Maclean, I.M.D., 2025. microctools: Various worker functions for microclimc package.

Maclean, I.M.D., Duffy, J.P., Haesen, S., Govaert, S., De Frenne, P., Vanneste, T., Lenoir, J., Lembrechts, J.J., Rhodes, M.W., Van Meerbeek, K., 2021. On the measurement of microclimate. Methods Ecol. Evol. 12, 1397–1410. https://doi.org/10.1111/2041-210X.13627

Maclean, I.M.D., Klinges, D.H., 2021. Microclimc: A mechanistic model of above, below and within-canopy microclimate. Ecol. Modell. 451, 109567. https://doi.org/10.1016/j.ecolmodel.2021.109567

Maes, W.H., 2025. Practical Guidelines for Performing UAV Mapping Flights with Snapshot Sensors. Remote Sens. (Basel). 17. https://doi.org/10.3390/rs17040606

Maes, W.H., Huete, A.R., Steppe, K., 2017. Optimizing the processing of UAV-based thermal imagery. Remote Sens. (Basel). 9. https://doi.org/10.3390/rs9050476

Man, M., Kalčík, V., Macek, M., Brůna, J., Hederová, L., Wild, J., Kopecký, M., 2023. myClim: Microclimate data handling and standardised analyses in R. Methods Ecol. Evol. 14, 2308–2320. https://doi.org/10.1111/2041-210X.14192

Manfreda, S., McCabe, M.F., Miller, P.E., Lucas, R., Madrigal, V.P., Mallinis, G., Dor, E. Ben, Helman, D., Estes, L., Ciraolo, G., Müllerová, J., Tauro, F., de Lima, M.I., de Lima, J.L.M.P., Maltese, A., Frances, F., Caylor, K., Kohv, M., Perks, M., Ruiz-Pérez, G., Su, Z., Vico, G., Toth, B., 2018. On the use of unmanned aerial systems for environmental monitoring. Remote Sens. (Basel). 10. https://doi.org/10.3390/rs10040641

Metsu, C., Maes, W.H., Ottoy, S., Van Meerbeek, K., 2026. theRmalUAV: An R package to clean and correct thermal UAV data for accurate land surface temperatures. Methods Ecol. Evol. 17, 488–496. https://doi.org/10.1111/2041-210x.70196

MicaSense, 2024. Using Panels and/or DLS in Post-Processing [WWW Document]. URL https://support.micasense.com/hc/en-us/articles/360025336894-Using-Panels-and-or-DLS-in-Post-Processing

Monin, A.S., Obukhov, A.M., 1954. Basic laws of turbulent mixing in the surface layer of the atmosphere. Tr. Akad. Nauk SSSR Geophiz. Inst. 24, 163–187.

QGIS Development Team, 2025. QGIS Geographic Information System.

R Core Team, 2023. R: A Language and Environment for Statistical Computing.

Raupach, M.R., 1989a. Applying Lagrangian fluid mechanics to infer scalar source distributions from concentration profiles in plant canopies. Agric. For. Meteorol. 47, 85–108.

Raupach, M.R., 1989b. A practical Lagrangian method for relating scalar concentrations to source distributions in vegetation canopies. Quarterly Journal of the Royal Meteorological Society 115, 609–632.

Ridgeway, G., GBM Developers, 2024. gbm: Generalized Boosted Regression Models. https://doi.org/10.32614/CRAN.package.gbm

Robinson, D.A., Campbell, C.S., Hopmans, J.W., Hornbuckle, B.K., Jones, S.B., Knight, R., Ogden, F., Selker, J., Wendroth, O., 2008. Soil Moisture Measurement for Ecological and Hydrological Watershed-Scale Observatories: A Review. Vadose Zone Journal 7, 358–389. https://doi.org/10.2136/vzj2007.0143

Rouse, J.W., Haas, R.H., Schell, J.A., Deering, D.W., 1974. Monitoring Vegetation Systems in the Great Plains with ERTS (Earth Resources Technology Satellite). Proceedings of the Third Earth Resources Technology Satellite- 1 Symposium 1, 309.

Rubio, E., Caselles, V., Badenas, C., 1997. Emissivity measurements of several soils and vegetation types in the 8-14 µm wave band: Analysis of two field methods. Remote Sens. Environ. 59, 490–521. https://doi.org/10.1016/S0034-4257(96)00123-X

Sievert, Carson., 2020. Interactive web-based data visualization with R, plotly, and shiny. CRC Press, Taylor and Francis Group.

Sun, X., Sun, Y., Zhou, Z., Alam, M.A., Bermel, P., 2017. Radiative sky cooling: fundamental physics, materials, structures, and applications. Nanophotonics 6, 997–1015. https://doi.org/10.1515/nanoph-2017-0020

TeAx, 2022. ThermalCapture Calibrator [WWW Document]. URL https://thermalcapture.com/thermalcapture-calibrator-2/

TeAx Technology, 2020. ThermoViewer.

Tian, X., Jia, X., Da, Y., Liu, J., Ge, W., 2025. Evaluating the sensitivity of vegetation indices to leaf area index variability at individual tree level using multispectral drone acquisitions. Agric. For. Meteorol. 364, 110441. https://doi.org/10.1016/j.agrformet.2025.110441

Van den Bossche, A., Moeys, K., De Pauw, K., Van Meerbeek, K., Thomaes, A., Brunet, J., Cousins, S.A.O., Diekmann, M., Graae, B.J., Hagenblad, J., Heavyside, P., Hedwall, P.-O., Heinken, T., Huang, S., Lenoir, J., Lindgren, J., Lindmo, S., Mazalla, L., Naaf, T., Orczewska, A., Paulssen, J., Plue, J., Spicher, F., Vanneste, T., Verheyen, K., Verschuren, L., Visakorpi, K., Wulf, M., De Frenne, P., 2025. Microclimate of large solitary trees along rural-to-urban gradients across Europe. Agric. For. Meteorol. 370, 110585. https://doi.org/10.1016/j.agrformet.2025.110585

Vaz, C.M.P., Jones, S., Meding, M., Tuller, M., 2013. Evaluation of Standard Calibration Functions for Eight Electromagnetic Soil Moisture Sensors. Vadose Zone Journal 12, 1–16. https://doi.org/10.2136/vzj2012.0160

Wang, Y., Fang, H., Zhang, Y., Li, S., Pang, Y., Ma, T., Li, Y., 2023. Retrieval and validation of vertical LAI profile derived from airborne and spaceborne LiDAR data at a deciduous needleleaf forest site. GIsci. Remote Sens. 60. https://doi.org/10.1080/15481603.2023.2214987

Watt, M.S., Meredith, A., Watt, P., Gunn, A., 2014. The influence of LiDAR pulse density on the precision of inventory metrics in young unthinned Douglas-fir stands during initial and subsequent LiDAR acquisitions. N. Z. J. For. Sci. 44, 18. https://doi.org/10.1186/s40490-014-0018-3

Wickham, H., Averick, M., Bryan, J., Chang, W., McGowan, L., François, R., Grolemund, G., Hayes, A., Henry, L., Hester, J., Kuhn, M., Pedersen, T., Miller, E., Bache, S., Müller, K., Ooms, J., Robinson, D., Seidel, D., Spinu, V., Takahashi, K., Vaughan, D., Wilke, C., Woo, K., Yutani, H., 2019. Welcome to the Tidyverse. J. Open Source Softw. 4, 1686. https://doi.org/10.21105/joss.01686

Wickham, H., François, R., Henry, L., Müller, K., Vaughan, D., 2023. dplyr: A Grammar of Data Manipulation. https://doi.org/10.32614/CRAN.package.dplyr

Wickham, Hadley., 2016. Ggplot2 : elegant graphics for data analysis. Springer.

Wild, J., Kopecký, M., Macek, M., Šanda, M., Jankovec, J., Haase, T., 2019. Climate at ecologically relevant scales: A new temperature and soil moisture logger for long-term microclimate measurement. Agric. For. Meteorol. 268, 40–47. https://doi.org/10.1016/j.agrformet.2018.12.018

Wittemans, K., Ottoy, S., Oorts, K., De Ruyck, J., Erauw, L., Luts, D., Salomez, J., Vancampenhout, K., Van Orshoven, J., 2023. Bodemdatabank-STAT: Koppeling van statistische bodemgegevens aan de bodemkaart gebaseerd op de bodemdata van de DOV-bodemdatabank, Databank Ondergrond Vlaanderen. Vlaams Planbureau voor Omgeving (Departement Omgeving) .

Wright, M.N., Ziegler, A., 2017. ranger : A Fast Implementation of Random Forests for High Dimensional Data in *C++* and *R*. J. Stat. Softw. 77. https://doi.org/10.18637/jss.v077.i01

Xiao, B., Bowker, M.A., 2020. Moss-biocrusts strongly decrease soil surface albedo, altering land-surface energy balance in a dryland ecosystem. Science of The Total Environment 741, 140425. https://doi.org/10.1016/j.scitotenv.2020.140425

YellowScan, 2024. CloudStation.

Yu, T., Zhou, J., Fan, J., Wang, Y., Zhang, Z., 2023. Potato Leaf Area Index Estimation Using Multi-Sensor Unmanned Aerial Vehicle (UAV) Imagery and Machine Learning. Remote Sens. (Basel). 15, 4108. https://doi.org/10.3390/rs15164108

Zellweger, F., De Frenne, P., Lenoir, J., Rocchini, D., Coomes, D., 2019. Advances in Microclimate Ecology Arising from Remote Sensing. Trends Ecol. Evol. 34, 327–341. https://doi.org/10.1016/j.tree.2018.12.012

Zellweger, F., Frenne, P. De, Lenoir, J., Vangansbeke, P., Verheyen, K., Bernhardt-Römermann, M., Baeten, L., Hédl, R., Berki, I., Brunet, J., Calster, H. Van, Chudomelová, M., Decocq, G., Dirnböck, T., Durak, T., Heinken, T., Jaroszewicz, B., Kopecký, M., Máliš, F., Macek, M., Malicki, M., Naaf, T., Nagel, T.A., Ortmann-Ajkai, A., Petřík, P., Pielech, R., Reczyńska, K., Schmidt, W., Standovár, T., Świerkosz, K., Teleki, B., Vild, O., Wulf, M., Coomes, D., 2020. Response to Comment on "Forest microclimate dynamics drive plant responses to warming." Science (1979). 370, 772–775. https://doi.org/10.1126/science.abf2939

Zhou, X., Fonteyn, W., Haesen, S., Sentinella, A., Van Meerbeek, K., 2025. Microclimate data reveal microrefugia potential in European forests. Biol. Conserv. 312, 111473. https://doi.org/10.1016/j.biocon.2025.111473

7. Supplementary Materials

Contents

Appendix A. General Additional Information

Figure A1. Schematic view (left) and picture in the field (right) of a TOMST TMS-4 logger. *The TOMST TMS-4 loggers were placed in the field, covered by a chromed steel shopping basket to protect them against grazers. The sensors were placed with the middle temperature sensor (T2) facing north and making contact with the ground. Left image inspired by Wild et al. (2019).*

Table A1. *The different bands available on the Micasense Altum-PT together with their central wavelength and bandwidth. Values taken from (Micasense Website), more sensor-specific information is available there as well.*

Band name	Central wavelength	Bandwidth
Blue	475 nm	32 nm
Green	560 nm	27 nm
Red	668 nm	16 nm
Red-Edge	717 nm	12 nm
Near Infrared	842 nm	57 nm
Panchromatic band	634.5 nm	463 nm
Thermal Infra-red	10.5 µm	6 µm

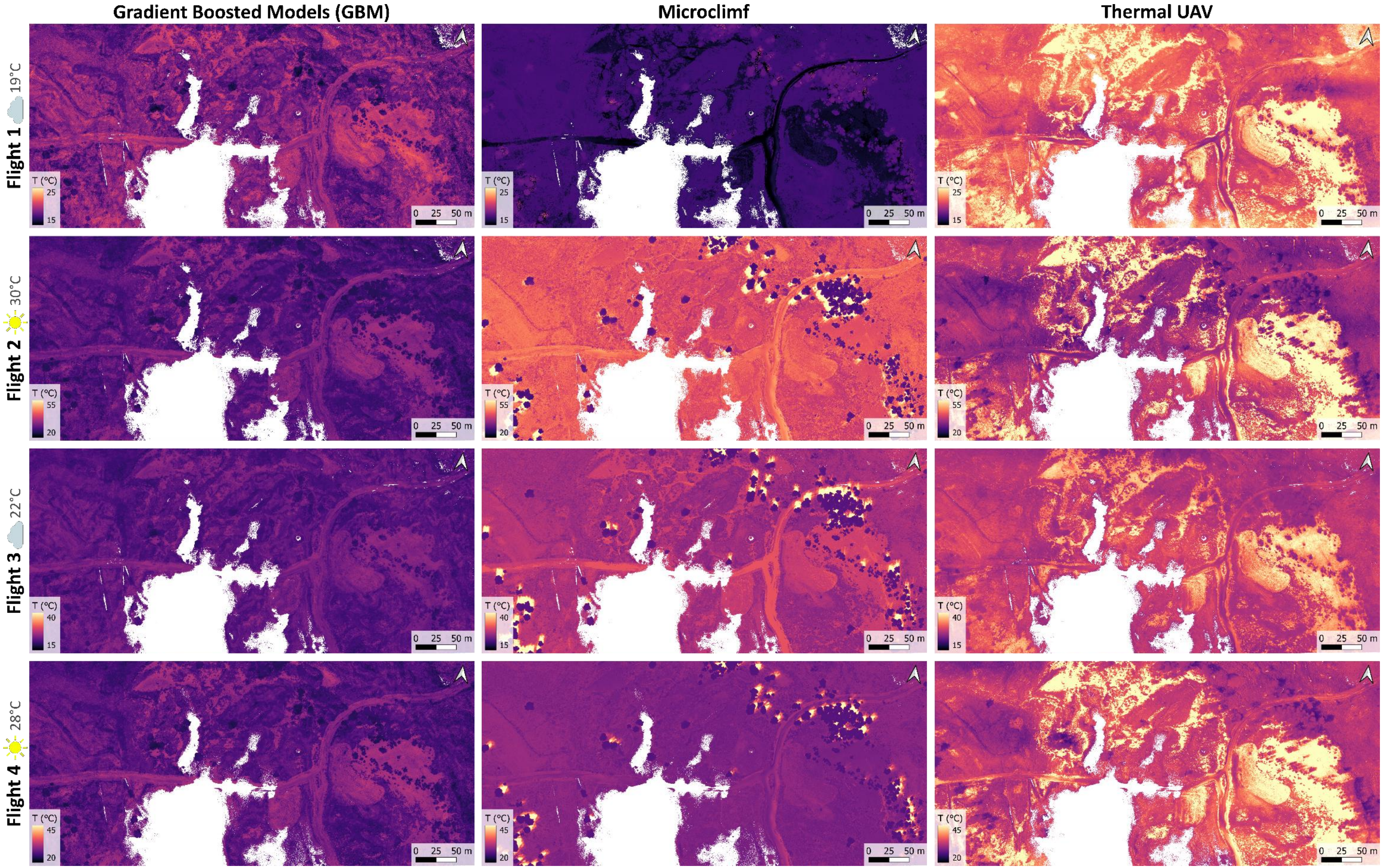

Figure A2. The modelled microclimate temperature at (ground)surface temperature*. Each column presents the output of a different model (left: Gradient Boosted Model (T at 0 cm), GBM; middle: full mechanistic model, microclimf; right: land surface temperature derived with the Thermal UAV data). Note the temperature range differs between the days, but is constant within a flight over the different models.*

Table A2. Conversion table from land cover classes to microclimf's habitat types. *As the grasslands were dominated by Molinia caerulea, we chose tall grassland. Note the solitary/patches of trees are classified as forest.*

Original land cover	Microclimf's habitat type
Grass	Tall grassland
Heath	Open shrubland
Moss	Barren or sparsely vegetated
Bare sandy soil	Barren or sparsely vegetated
Trees	Evergreen needleleaf forest
Water	Permanent wetland

Appendix B. Results Land Cover Classifications

The landcover classification map was created using the reflectance values of the multispectral (MSP) data (blue, green red, red-edge, and NIR), the normalized difference vegetation index (NDVI), and the canopy height model (CHM). A random forest model was trained and tuned using the ranger package (Wright and Ziegler, 2017) and the caret package (Kuhn, 2008b). The final model consisted of 500 trees, an mtry of 4, min.node.size of 3 and Gini as split rule. The overall accuracy was 94.6 % and the Kappa was 92.7 %. The confusion matrix is presented in Table B1, and the accuracy metrics per class are summarized in Table B2. An example of the land cover class over the flight block "ANBH1" is presented in Figure B1.

Table B1. *The confusion matrix for the land cover classification used for the GBM model training. The rows represent the ground truth, the columns the predicted values.*

Predicted **TRUE**	**Heath**	**Sand**	**Tree**	**Grass**	**Water**	**Moss**
Heath	85002	47	9	6043	92	890
Sand	172	12895	7	288	6	151
Tree	120	0	35609	297	6	10
Grass	4521	96	13	100034	6	605
Water	279	15	0	136	30987	2
Moss	1187	109	0	634	1	10499

Table B2. *Summary of the accuracy metrics per class.*

	Heath	**Sand**	**Tree**	**Grass**	**Water**	**Moss**
Sensitivity	0.9312	0.97971	0.9992	0.9311	0.9964	0.86362
Specificity	0.9645	0.99775	0.9983	0.9714	0.9983	0.99307
Pos Pred Value	0.9231	0.95384	0.9880	0.9502	0.9863	0.84465
Neg Pred Value	0.9684	0.99904	0.9999	0.9601	0.9996	0.99404
Precision	0.9231	0.995384	0.9880	0.9502	0.9863	0.84465
Recall	0.9312	0.97971	0.9992	0.9311	0.9964	0.86362
F1	0.9271	0.96661	0.9936	0.9406	0.9913	0.85403
Prevalence	0.3139	0.04527	0.1226	0.3695	0.1070	0.04181
Detection Rate	0.2923	0.04435	0.1225	0.3440	0.1066	0.03611
Detection Prevalence	0.3167	0.04649	0.1240	0.3621	0.1081	0.04275
Balanced Accuracy	0.9479	0.98873	0.9987	0.9513	0.9974	0.92834

Each thermal flight was accompanied with MSP data for co-registration and emissivity correction. In this study we performed spatial emissivity correction based on land cover type and thus made land cover maps for each corresponding thermal flight. The accuracies can be found in Table B3.

Table B3. *Summary of the accuracy metrics for the LC maps corresponding with the four thermal flights.*

		Heath	Sand	Tree	Grass	Water	Moss
Flight 1 : 2024-06-13							
Overall Accuracy	0.9656						
Kappa	0.9566						
Precision		0.9573	0.95370	0.99035	0.9508	0.9997	0.93470
Recall		0.9564	0.97658	0.99716	0.9614	0.9998	0.88817
F1		0.9569	0.96501	0.99374	0.9561	0.9997	0.91084
Flight 2 : 2024-06-26							
Overall Accuracy	0.9659						
Kappa	0.9571						
Precision		0.9426	0.97426	0.99145	0.9522	0.9995	0.95775
Recall		0.9501	0.98399	0.99685	0.9576	0.9997	0.91262
F1		0.9464	0.97910	0.99414	0.9549	0.9996	0.93464
Flight 3 : 2024-07-25							
Overall Accuracy	0.9680						
Kappa	0.9596						
Precision		0.9549	0.93911	0.99168	0.9589	0.9999	0.95190
Recall		0.9591	0.97152	0.99655	0.9616	0.9999	0.90821
F1		0.9570	0.95504	0.99411	0.9603	0.9999	0.92954
Flight 4 : 2024-08-06							
Overall Accuracy	0.9654						
Kappa	0.9564						
Precision		0.9416	0.97539	0.99142	0.9485	0.9998	0.9636
Recall		0.9477	0.98635	0.99701	0.9547	0.9998	0.9191
F1		0.9446	0.98084	0.99421	0.9516	0.9998	0.9408

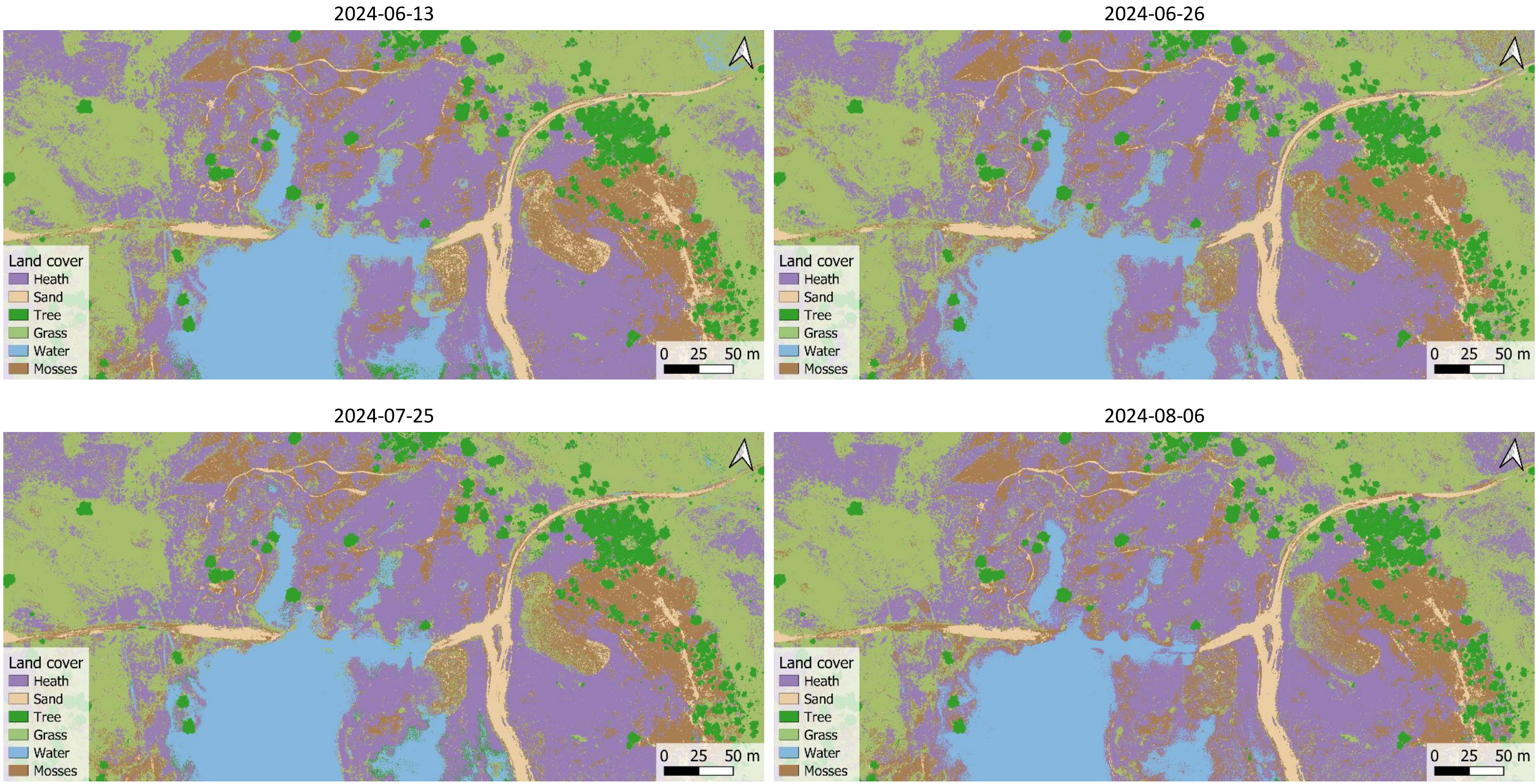

Figure B1. Land cover classes for each flight. *Spatial representation of the different landcover classes for each flight. Note the water level changes throughout the season.*

Appendix C. Processing Thermal UAV data

The ThermalCapture 2.0 camera provides raw data as .TMC file containing thermal images captured at 8 Hz. To convert these images to tiff files, we used TeAx' ThermoViewer 3.0.10 (TeAx Technology, 2020). The corresponding metadata was exported as a single .csv file. As the ThermalCapture provided us with at-sensor temperatures, we still need to do the necessary corrections to obtain Land Surface Temperature (LST). We used the *theRmalUAV* R package (Metsu et al., 2026) to streamline these corrections. Here we adopted the image-based workflow to be able to account for variations throughout the flight.

First a ThermalUAV object was created using the metadata exported from ThermoViewer. The amount of thermal images was reduced by setting a minimal overlap of 90 %. Second, the background temperature was retrieved by calculating the brightness temperature of the crumpled aluminium foil panels. Thrid, the atmospheric correction was performed using the weather data retrieved with the portable weather station Kestrel 5500L using the *data.frame* option in *tuav_correct().* We set the emissivity to 1 to obtain the atmospherically corrected brightness temperatures. Finally, we accounted for the effect of air temperature on LST (Maes et al., 2017) by using *tuav_smooth()* in "T_air" option.

In order to optimize the location accuracy of the ThermalCapture through co-registration, we first processed the accompanying MSP data in the same way as described in Section 2.3.3. Hereafter, the estimated camera locations of the MSP were exported from Agisoft Metashape as a csv-file. The thermal cameras were then co-reigtered using the theRmalUAV package with an offset of 46, -103, and 20 mm in respectively the X, Y, Z plane. The corrected tif files containing brightness temperatures and accurate location information where then exported and stitched in Agisoft Metashape using default values, resulting in a brightness temperature orthomosiac.

Finally, in order to retrieve the LST, the spatial emissivity correction was performed. The surfaces present in our landscape exhibit different surface properties, so we cannot just assume a uniform emissivity. We spatially accounted for emissivity based on land cover type. Therefore, we created a landcover map based on the corresponding MSP data of the thermal flights, in the same way as described in Section 2.3.3. As the water level fluctuated throughout the season and the flights were conducted under varying illumination, we generated a LC maps for each flight, based on the reference polygons in flight block "ANBH1". The accuracy of each map can be found in Supplementary Materials, 0. For each land cover type the emissivity was derived from Rubio, Caselles and Badenas (1997) and presented Table C1. After the spatial emissivity correction, the final corrected land surface temperature maps were returned.

Table C1. *Land cover types with their corresponding emissivity values.*

Label	Land cover	Emissivity
1	Heath	0.984
2	Sand	0.914
3	Tree	0.983
4	Grass	0.984
5	Water	0.991
6	(Dry) Moss	0.962

Appendix D. Input variable overview

In this study we use many input variables either spatial or tabular. These variables are used to train the model, correct certain properties or to predict the microclimate temperature. Here we present an overview table with all the variables together with if and how they are used in each model.

Table D1. Overview of the input variables used by the different modelling approaches. *The variables are grouped in a) spatially explicit variables, derived by the unoccupied aerial vehicles (UAV) or nationally available data, and b) temporally explicit variables, derived from either the automatic weather station (AWS) or by the Kestrel 5500L environmental meter in the field.*

Variable	Unit	Description	GBM	Microclimf	Thermal UAV
Spatially explicit data derived from unoccupied aerial vehicles (UAV) at 10 cm resolution					
DTM	m	Digital terrain model, the elevation of the terrain above sea level. Derived from LiDAR data at 10 cm resolution	Used to train and predict	Used as input for terrain variable	/
CHM	m	Canopy height model, the vegetation height derived through subtracting the DTM from the digital surface model DSM (both derived from LiDAR) at 10 cm resolution.	Used to train and predict	Used as input for canopy height	Used as canopy height to convert LST to T_z
East	[-1,1]	Eastness, calculated as sine of the aspect in radians, which in turn was calculate from DTM using terra (Hijmans, 2022), at 10 cm resolution	Used to train and predict	/	/
North	[-1,1]	Northness, calculated as cosine of the aspect in radians, which in turn was calculate from DTM using terra (Hijmans, 2022), at 10 cm resolution	Used to train and predict	/	/
Slope	°	Measure of steepness, calculated from DTM using terra (Hijmans, 2022) at 10 cm resolution	Used to train and predict	/	/
TPI	m	Topographic position index, a measure of relative topography, calculated using MultscaleDTM (Ilich et al., 2023) with a kernel of 10 x 10 m at 10 cm resolution	Used to train and predict	/	/
Rough	/	Roughness, Vector Ruggedness Measure (VRM, Ilich et al., 2023) calculated from DSM with a 3 x 3 m kernel, at 10 cm resolution	Used to train and predict	/	/
LC	/	Land Cover, a land cover classification map, made using trained and tuned RandomForest model (Wright and Ziegler, 2017). Available classes are: Heath, Sand, Tree, Grass, Water, and Moss. 10 cm resolution (0)	LC map from 19/09/2026 was used to train, the LC maps from the thermal flight days were used to predict	LC maps from the thermal flight days were reclassified and used in vegfromhab() function (Maclean, 2026) to retrieve vegetation parameters	LC maps from the thermal flight days were used for spatial emissivity correction in the theRmalUAV package (Metsu et al., 2026)
NDVI	[-1,1]	Normalized Difference Vegetation Index [-1,1] as proxy for greenness and plant density	NDVI map from 19/09/2026 was used to train, the NDVI maps from the thermal flight days were used to predict	NDVI maps from the thermal flight days were used to estimate plant area index	NDVI maps from the thermal flight days were used to estimate plant area index in the conversion to T_z

Variable	Unit	Description	GBM	Microclimf	Thermal UAV
Spatial explicit data derived from national geo service					
Sand	%	Sand soil fraction at 10 m resolution from Databank Ondergrond Vlaanderen	Used to train and predict	Used to derive input soil type	/
Silt	%	Silt soil fraction at 10 m resolution from Databank Ondergrond Vlaanderen	Used to train and predict	Used to derive input soil type	/
Clay	%	Clay soil fraction at 10 m resolution from Databank Ondergrond Vlaanderen	Used to train and predict	Used to derive input soil type	/
Temporal weather information					
Macro_T	°C	The hourly aggregated macroclimate free air temperature at 2 m height, measured by a nearby automatic weather station (AWS) at 10 min intervals hosted by the royal meteorological institute (KMI), one value for the study area	Used to train and predict	Used as input climate dataframe	Air temperature from the Kestrel meter was used to correct the thermal data and in the conversion to T_z
wind_s	m/s	The hourly aggregated wind speed, measured by the AWS at 10 min intervals, one value for the study area	Used to train and predict	Used as input climate dataframe	Wind speed measured with Kestrel meter was used in the conversion to T_z
wind_dir	°	The hourly aggregated wind direction, measured by the AWS at 10 min intervals, one value for the study area	/	Used as input climate dataframe	/
rel_hum	%	The hourly aggregated relative humidity, measured by the AWS at 10 min intervals, one value for the study area	Used to train and predict	Used as input climate dataframe	Relative humidity from the Kestrel meter was used to correct the thermal data and in the conversion to T_z
Pressure	Pa	The hourly aggregated atmospheric pressure, measured by the AWS at 10 min intervals, one value for the study area	/	Used as input climate dataframe	Atmospheric Pressure measured with Kestrel meter was used in the conversion to T_z
glob_rad	W/m^2	The hourly aggregated global shortwave downwelling radiation, measured by the AWS at 10 min intervals, one value for the study area	Used to train and predict	Used as input climate dataframe, and used to calculate diffuse radiation	/
Lw_down	W/m^2	The hourly aggregated longwave downwelling radiation, measured by the AWS at 10 min intervals, one value for the study area	Used to train and predict	Used as input climate dataframe	/
Precip	mm	The hourly precipitation, measured by the AWS, one value for the study area	/	Used as input climate dataframe	/
Precip_48	mm	The total accumulated precipitation from the last 48 hours, calculated from the precipitation derived from the AWS, one value for the study area	Used to train and predict	/	/
Alt	°	Solar altitude, calculated using the microctools package (Maclean, 2025) with date, latitude and longitude.	Used to train and predict	/	/
Azi	°	Solar azimuth, calculated using the microctools package (Maclean, 2025) with date, latitude and longitude.	Used to train and predict	/	/

The maps with input variables derived from LiDAR and multispectral UAV data for flight block ANBH1 illustrate the highly heterogeneous landscape, with varying vegetation structures, slopes, and expositions, covering an area of approximately 14 hectares (Figure D1)

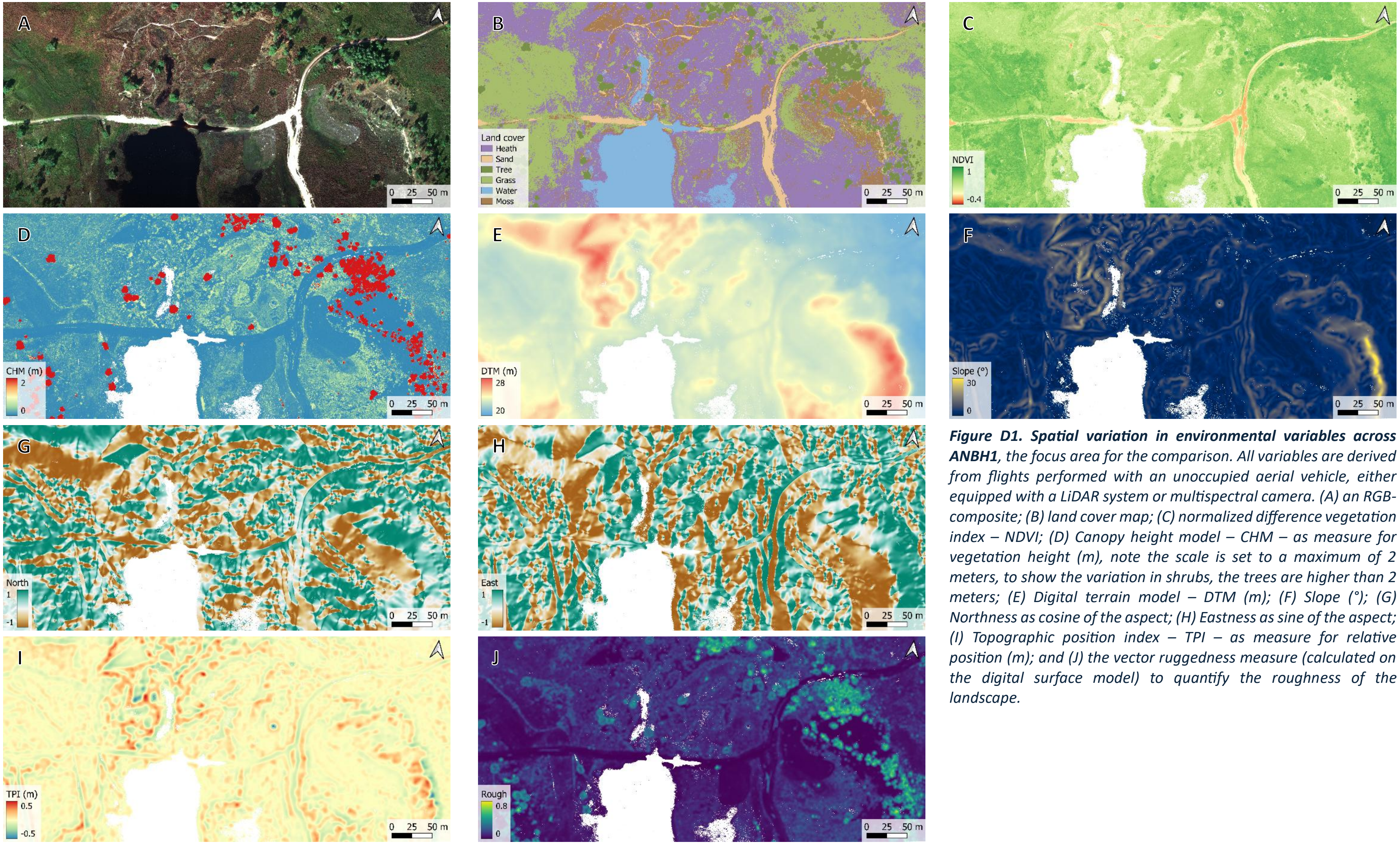

***Figure D1. Spatial variation in environmental variables across ANBH1**, the focus area for the comparison. All variables are derived from flights performed with an unoccupied aerial vehicle, either equipped with a LiDAR system or multispectral camera. (A) an RGB-composite; (B) land cover map; (C) normalized difference vegetation index – NDVI; (D) Canopy height model – CHM – as measure for vegetation height (m), note the scale is set to a maximum of 2 meters, to show the variation in shrubs, the trees are higher than 2 meters; (E) Digital terrain model – DTM (m); (F) Slope (°); (G) Northness as cosine of the aspect; (H) Eastness as sine of the aspect; (I) Topographic position index – TPI – as measure for relative position (m); and (J) the vector ruggedness measure (calculated on the digital surface model) to quantify the roughness of the landscape.*

Appendix E. Training and tuning the GBM

The gradient boosted model (gbm) used in the correlative approach was trained and tuned using the packages caret (Kuhn, 2008b) and gbm (Ridgeway and GBM Developers, 2024) in R 4.3.1 (R Core Team, 2023). The eventual model had the following structure:

Micro_T ~ DTM + CHM + East + North + Slope + TPI + Rough + LC + NDVI + Sand + Silt + Clay + Macro_T + wind_s + rel_hum + glob_rad + alt + azi + precip_48 + Lw_down

With Micro_T the microclimate temperature (°C) at 0 cm (T2) and 13 cm (T3).

The input variables varying over the spatial scale are (Table D1): the elevation above sea level as the digital terrain model (DTM; m), the canopy height model (CHM; m), the northness (North) and eastness (East) as respectively the cosine and sine of the aspect, the Slope in degrees, the topographic position index (TPI; m) as relative position in a 10m x 10m window, the surface roughness (rough) in a 3m x 3m window give as the vector ruggedness measure, the land cover class (LC; 0), the normalized difference vegetation index (NDVI) as measure for plant density and greenness, and the Sand, Silt and Clay content in percentages.

The input variables varying over the temporal scale are (Table D1): the macroclimate temperature (Macro_T; °C), wind speed (wind_s; m/s), relative humidity (rel_hum; %), global shortwave radiation (glob_rad; W/m^2), solar altitude and azimuth (resp. alt, azi; °), the accumulative precipitation in the last 48 hours (precip_48; mm) and the downwelling longwave radiation (Lw_down; W/m^2).

Different hyperparameter combinations were modelled to check which set gave the most accurate results. As we wanted to keep relatively shallow trees the shrinkage (learning rate) was set to 0.01. The tuning grid was thus set as follows: shrinkage: 0.01, interaction.depth: 2,3,4, n.trees: 5000:10000 in steps of 500, and n.minobsinnode: 8,10,12. Here, shrinkage or learning rate represents the relative contribution of each tree; interaction.depth the number of splits/levels in each tree (here again not too deep to avoid overfitting and capturing the main effects); n.trees the number of trees; and n.minobsinnode, the minimum number of observations in each leaf.

The models were assessed based on three accuracy metrics: mean absolute error (MAE), root mean squared error (RMSE) and the coefficient of determination (R^2). The final hyperparameter sets for T2 and T3 together with the accuracy metrics are presented in Table E1.

Table E1. *Overview of the final hyperparameter set together with the accuracy metrics for the temperature at ground surface (T_{0cm}, TMS-4 T2 sensor) and the near surface air temperature at 13 cm (T_{13cm}, TMS-4 T3 sensor).*

	T_{0cm}	T_{13cm}
Hyperparameter		
Shrinkage	0.01	0.01
Interation.depth	2	2
n.trees	10000	10000
n.minobsinnode	12	12
Accuracy Metric		
MAE	1.411	1.286
RMSE	2.057	1.996
R^2	0.848	0.908

The accuracy metrics for all hyperparameter combinations are presented in Figure E1 and Figure E2. Note that the proposed final model (the one with the highest accuracy) is different from the one used in the study. As one can notice, the differences in accuracy are marginal. To avoid overfitting, and since the models with interaction depth equal to two are already stabilizing around 10.000 trees, we went with an interaction depth of 2 for the final model in the study.

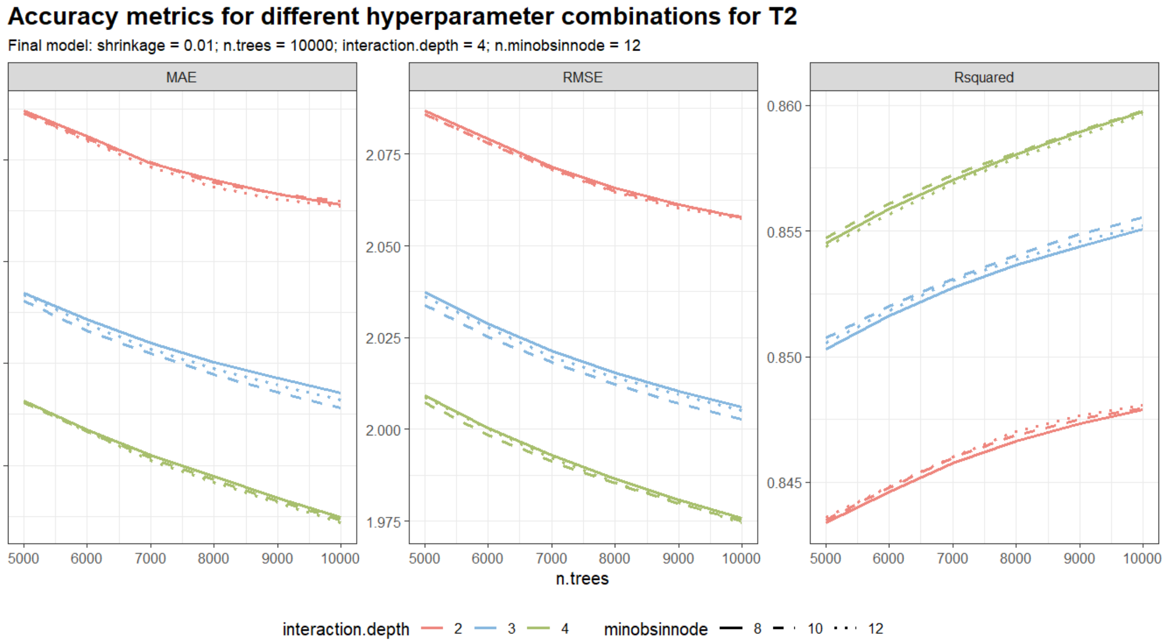

Figure E1. Accuracy metrics for the different hyperparameter combinations for T2. *The Mean Absolute Error (MAE), Root Mean Squared Error (RMSE) and the coefficient of determination (R^2) are given for all the hyperparameter sets. Note the proposed final model here is the one with the highest accuracy based on R^2 and is different from the one used in the study.*

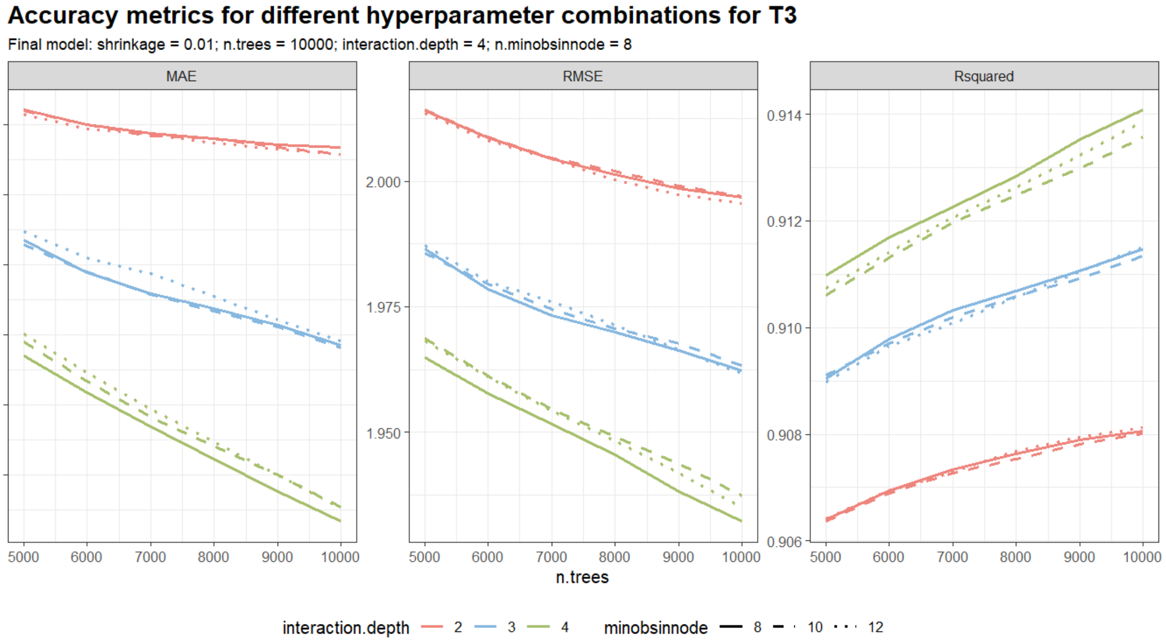

Figure E2. Accuracy metrics for the different hyperparameter combinations for T3*. The Mean Absolute Error (MAE), Root Mean Squared Error (RMSE) and the coefficient of determination (R^2) are given for all the hyperparameter sets. Note the proposed final model here is the one with the highest accuracy based on R^2 and is different from the one used in the study.*

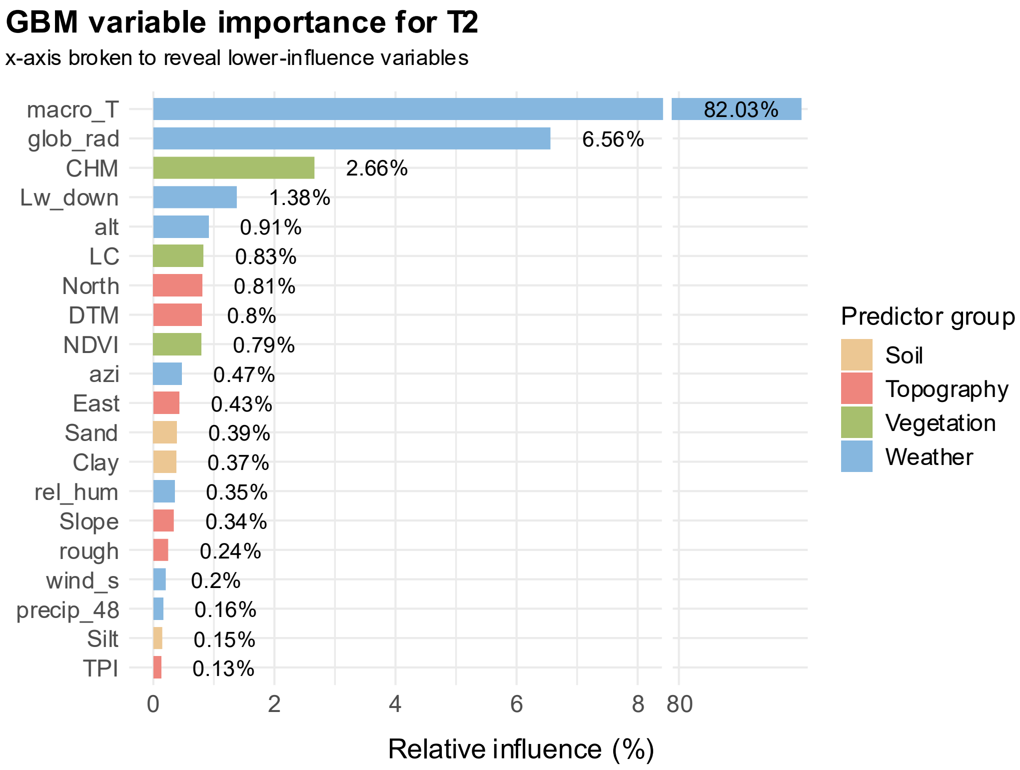

Figure E3. *The variable importance of the different input variables for the gradient boosted models (GBMs) for the microclimate at the ground surface (TMS-4 T2, T_0). Note the x-axis has a break to also provide information on the lower-influence variables.*

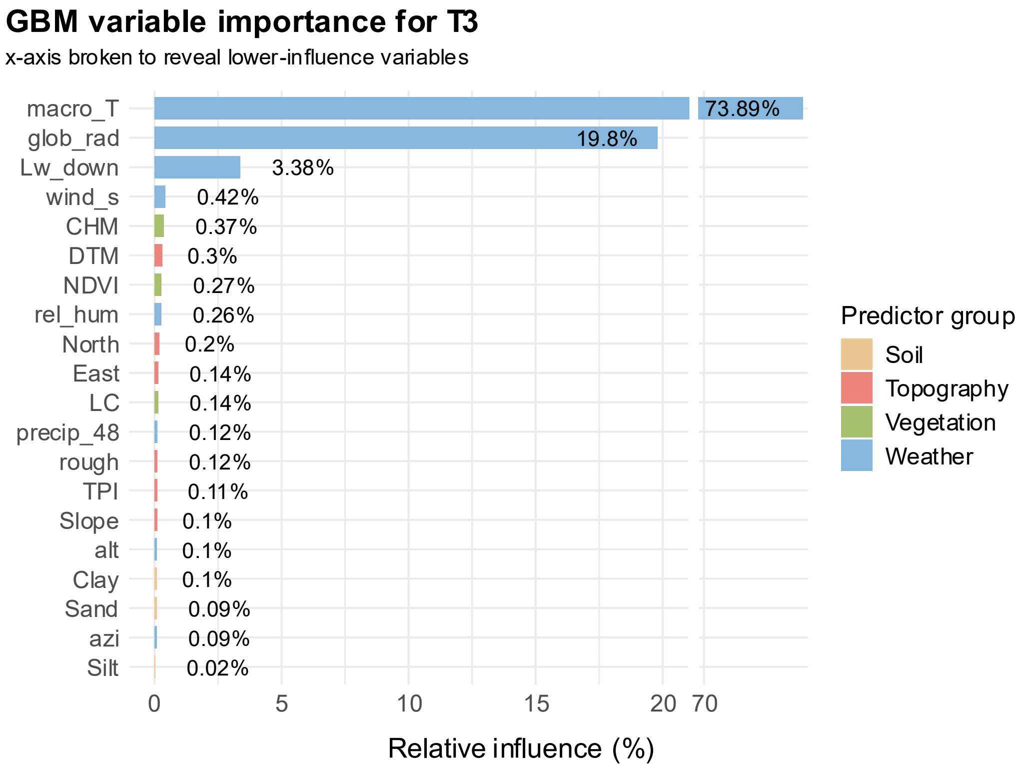

Figure E4. *The variable importance of the different input variables for the gradient boosted models (GBMs) for the microclimate at 13 cm height (TMS-4 T3, T_{13cm}). Note the x-axis has a break to also provide information on the lower-influence variables.*

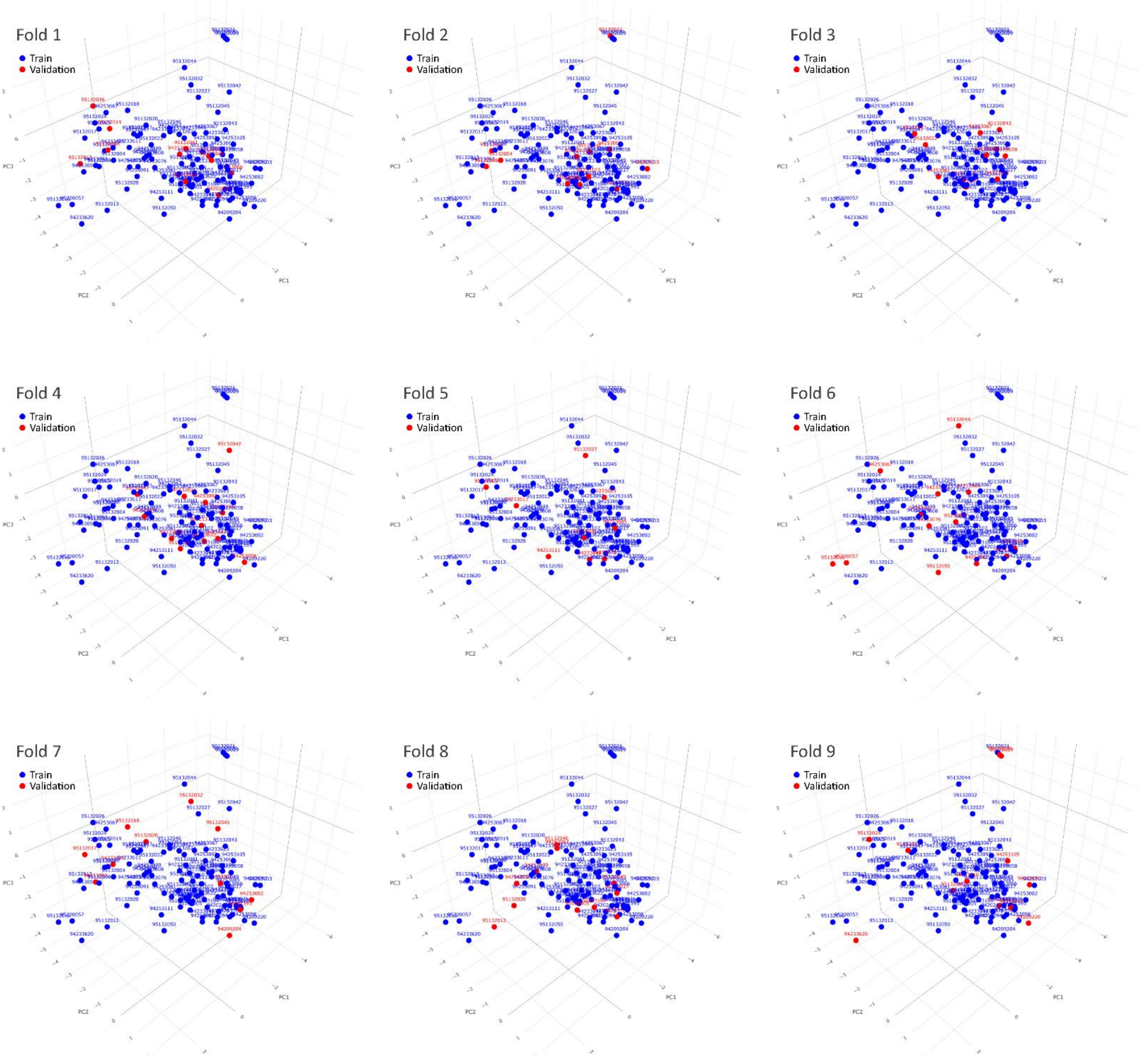

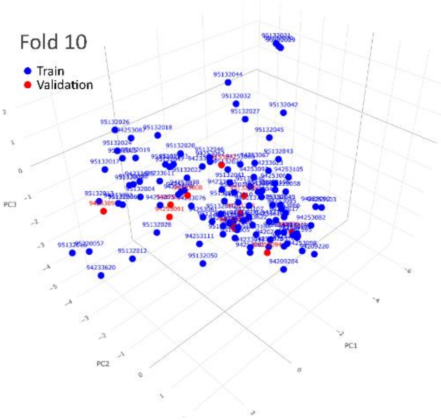

***Figure E5. The different spatial folds created to perform the 10 fold cross validation**. This serves as visual inspection that the validation folds are not clustered outside the main environmental range covered by the training set. The logger ID's are presented as label. The training set per fold is given in blue and the validation set in red.*

Appendix F. Converting LST into temperature at 13 cm

Thermal data acquired with an unoccupied aerial vehicle (UAV), provide us with information on the land surface temperature (LST). LST is a highly valuable parameter to look at microclimate, especially to uncover spatial heterogeneity. However, in some cases, microclimate research focusses on near surface temperatures. Hence, a one on one comparison of LST with near surface temperatures measured with in situ loggers is not straightforward. Here, we outline a way to convert the LST to the air temperature at height z (T_z). Through this way we want to highlight an interesting avenue of the potential of thermal UAV data in microclimate research. This conversion is twofold, depending on the desired height (z) of T_z and the canopy height of the plants:

1. T_z is above the canopy/ground surface
2. T_z is below the canopy/vegetation surface

Thus, the vegetation structure will depict which workflow to follow for that specific area/pixel. If the desired near surface temperature is above bare soil or mosses, we should apply the above canopy model. On the other hand, where shrubs or grasses are higher compared to the desired height, we should follow the second approach. We mostly follow the formulae and approaches used in the microclimf model (Maclean, 2026), for modelling and solving the radiation budgets and modelling T_z above and below canopy, with some adjustments to incorporate LST as the top of canopy leaf temperature.

1. T_z Above canopy/surface

In this first case we outline the method to derive temperature at a certain height above the canopy. To model this we used the standard Monin-Obukhov Similarity Theory (MOST, (Foken, 2006; Monin and Obukhov, 1954)) in order to work with the energy balance of a vegetated surface. Important, we assume a vegetated surface, e.g. a small layer of moss, grasses or small shrubs. Above the canopy, wind profiles are responsible for the heat and vapor exchange between the canopy and the air above. Here we are interested in near surface temperatures and assume the temperature of the canopy to be known as the land surface temperature measured by the thermal camera on the unoccupied aerial vehicle (UAV). The surface with known temperature exchanges heat with the air layer above through eddy diffusion. The key is now to solve the near surface air temperature, given the surface temperature and weather conditions at a reference height (in our case, measured at 1.5m height with the Kestrel 5500L environmental meter).

T_z (°C) at any given height z (m, above the canopy, can be derived from the canopy temperature (T_C, °C) and a reference temperature T_A (°C) at height z_R (m) through the following equation (Maclean, 2026):

$$T_z = T_A + (T_C - T_A)\left(1 + \frac{\ln\frac{z-d}{z_H}}{\ln\frac{z_R-d}{z_H}}\right)$$

with d the zero plane displacement length (m), a measure representing the height within the canopy where the windspeed approximates zero. Z_H is the roughness length for heat. The zero plane displacement length can be calculated using the total plant area index (Pai, m^2/m^2) and the canopy height h (m):

$$d = h\frac{1-(1-\exp(-\sqrt{7.5\,Pai})}{\sqrt{7.5\,Pai}}$$

The only unknown still in the equation is now the roughness length for heat z_H with $z_H = 0.2 * z_M$, the roughness length for momentum (Campbell and Norman, 1998). The roughness length for momentum is given by:

$$z_M = (h-d)\exp\left(\frac{-\kappa}{\beta} - \psi_H(z_R)\right)$$

Where h is the canopy height (m), d is the zero plane displacement length (m), κ is the Von Karman constant (0.4), β given by $\sqrt{0.003 + 0.1\,Pai}$ and ψ_H the diabatic correction factor for heat. This diabatic correction takes turbulence created by strongly heated or cooled surfaces into account.

According to Harman and Finnigan, (2008) the diabatic correction factor for heat and momentum are given by:

$$\psi_M(z) = \psi_M\frac{z_M}{Lo} - \psi_M\frac{z-d}{Lo}$$

$$\psi_H(z) = \psi_H\frac{z_H}{Lo} - \psi_H\frac{z-d}{Lo}$$

Where Lo is the Obukhov length given by:

$$Lo = -\frac{\tilde{\rho} c_p u_*^3 \bar{T}}{\kappa g H}$$

$\tilde{\rho}$ is the molar density of air (mol m^{-3}) and c_p represents the heath capacity at constant pressure, u_* is the friction velocity, $\bar{T}$ the average temperature of the wind profile in Kelvin (here assumed to be equal to T_A), g is the gravitational constant (9.81 m/s^2) and H is the sensible heat flux (W m^{-2}). The friction velocity and sensible heat flux can then again be calculated using the following equations:

$$u_* = \frac{\kappa u_{z_R}}{\ln\frac{z_R-d}{z_M} + \psi_M(z_R)}$$

$$H = \frac{\kappa \tilde{\rho} c_p u_* (T_C - T_A)}{\ln\frac{z_R-d}{z_H} + \psi_H(z_R)}$$

where u_{z_R} is the wind speed at the reference height (m s^{-1}) and $\psi_M(z_R)$ and $\psi_H(z_R)$ the diabatic correction factor for respectively momentum and heat for the reference height.

Depending on whether the air layer is stable (H < 0, cool surface, heat transfer from the air to the surface) or unstable (H > 0, warm surface, heat transfer from the surface to the air), the diabatic correction factors are calculated in a different way following Businger et al. (1971) using:

$$\zeta = \frac{-\kappa g H z}{\tilde{\rho} c_p u_*^3 \bar{T}} = \frac{z}{Lo}$$

Unstable conditions:

$$\psi_M(\zeta) = \ln\left[\left(\frac{1+x}{2}\right)^2\left(\frac{1+x^2}{2}\right)\right] - 2\arctan x + \frac{\pi}{2}$$

with $x = \sqrt[4]{1-15\zeta}$,

$$\psi_H(\zeta) = \ln\left[\left(\frac{1+\sqrt{1-9\zeta}}{2}\right)^2\right]$$

Stable conditions:

$$\psi_M(\zeta) = -4.7\,\zeta$$

$$\psi_H(\zeta) = -4.7\zeta/0.74$$

As the attentive reader may have noticed by now is that in order to calculate z_M, we need u_* and H, which depend on z_M itself and each other. We thus need an iterative optimization process to estimate these three parameters. Once z_M is know, we can calculate T_z.

2. T_z Below canopy

In case the desired height of our temperature lies within the canopy (e.g., within a shrub), we cannot use the MOST approach (e.g., Bonan et al., 2021). To calculate the temperature profile within the canopy, Raupach (1989b, 1989a), developed an approach to predict the concentration of heat and vapour within a canopy, using Lagrangian theory. This is called the "localized near-field" theory (LNFT), whereby the mean concentrations of heat and vapor are the sum of a diffusive far-field contribution obeying the Monin-Obukhov Similarity Theory, and a non-diffusive near-field contribution coming from local sources (e.g., leaves) where turbulence is assumed to be locally homogenic. In the following text we present the formulae derived from the *microclimf* approach. We outline our reasoning and assumptions made to come to a method to derive T_z from LST. For more information on the derivation or interpretation on the formulae we gladly guide the reader to MacLean (2026). Following Raupach's theory, the temperature at a certain height z, above the ground but below the canopy can be given by:

$$\tilde{\rho} c_p T_z = C_f(z) + C_n(z)$$

$$C_f(z) = \tilde{\rho} c_p T_H - C_n(h) + \int_z^h \frac{H(z_i)}{K_H(z_i)} dz$$

$$H(z_i) = \frac{\tilde{\rho} c_p}{r_L}\left(T_{c_i} - T(z_i)\right) + F_G$$

Where T_z is the temperature at a height z above the ground, but within the canopy. $\tilde{\rho}$ is the molar density of air (mol m^{-3}) and c_p represents the heath capacity at constant pressure. $C_f(z)$ and $C_n(z)$ are respectively the far-field and near-field contributions. T_H is the air temperature at the top of the canopy whereby the $C_f(h) = \tilde{\rho} c_p T_H$. The thermal diffusivity is given as K_H, r_L is the resistance to heat loss at the boundary layer with the elements in the canopy with temperature T_{c_i}. The ground heat flux is presented as F_G. The near-field contribution is given by:

$$C_n(z) = \int_0^\infty \frac{S(z_i)}{\sigma_\omega(z)} k_n \left[\frac{z - z_i}{\sigma_\omega(z_i) T_L} + \frac{z + z_i}{\sigma_\omega(z_i) T_L}\right] dz_i$$

where $S(z_i)$ is the source concentration given by $f_d(z_i)H(z_i)$ where $f_d(z_i)$ is the foliage density for layer z_i and k_n presents a kernel function which can be approximated by

$$k_n \approx -0.39894 \ln\left(1 - e^{\zeta}\right) - 0.15623\, e^{\zeta} \qquad \text{with} \qquad \zeta = \frac{|h-z|}{\sigma_\omega(z_i) T_L}$$

The problem with the Lagrangian approach is that it relies on two parameters: the particle position variance (σ_ω^2) and the lagrangian time scale T_L. Both appear in the formulae we need, but neither are actually known. Raupach (1989a) proposed plausible vertical profiles:

$$T_L = \frac{a_2 h}{u_*}$$

$$\sigma_\omega(z_i) = u_* \left[0.5(a_1 + a_0) + 0.5(a_1 - a_0)\cos\left(\pi\left(1 - \frac{z_i}{h}\right)\right)\right]$$

here, a_1 is given by 1.25 as it is the values of $\sigma_\omega(z_i)/u_*$ at the top of canopy (height = h), and a_0 is equal to 0.25. The parameter a_2 is unknow but generally taken to be vertically constant. Solving for a_2 is done by some authors (e.g., Ogée et al., 2003) by reconciling conventional MOST with LNFT by making the thermal diffusivity (K_H) equivalent with the above canopy ($z = h$), this gives the following:

$$\kappa\, u_* \frac{z-d}{\phi_H} = \sigma_\omega(z_i)^2\, T_L$$

Where the left side of the equation is the thermal diffusivity (K_H) for above canopy and the right side is the thermal diffusivity for below canopy. Setting $a_1 = 1.25$ and $a_0 = 0.25$ and solving for a_2 gives:

$$a_2 = \frac{\kappa\left(1 - \frac{d}{h}\right)}{1.25^2\, \phi_H}$$

with ϕ_H the diabatic correction coefficient for heat for the above canopy temperature (Campbell and Norman, 1998). The diabatic correction coefficient following Yasuda (1988) can be written as:

$$\sqrt{\phi_H} = \frac{1}{(1 - 16\zeta)^{1/4}}$$

For unstable conditions, for stable conditions:

$$\phi_H = 1 + \frac{6\zeta}{1 + \zeta}$$

where ζ is given by (see above canopy derivation):

$$\zeta = \frac{-\,\kappa g H z}{\tilde{\rho} c_p u_*^3 \overline{T}} = \frac{z}{Lo}$$

Now that we have a way to derive a_2 we can also deduct T_L and $\sigma_\omega(z_i)$. We thus first need to solve the above canopy equation to derive ϕ_H, u_*, and sensible heat flux and subsequently derive the temperature within the canopy.

To derive the temperature within the canopy we also need the ground heat flux, as it needed for deriving the sensible heat flux at z_i ($H(z_i)$) given by Fick's law:

$$F_G = \tilde{\rho} c_p \bar{K}_{z,0} (T_G - T_z)$$

Here T_z is the air temperature at height z and $\bar{K}_{z,0}$ represents the average thermal diffusivity within the canopy and can be calculated as:

$$\frac{1}{\bar{K}_{z,0}} = z \int_0^z \frac{1}{K_H(z)} dz$$

The previously presented formulae requires integration over the whole canopy, whereby the canopy is divided in numerous layers whereby every layer has a known canopy density. This is practically challenging to derive such data. Furthermore, it is computationally very inefficient to solve al these equations on pixel level, even if the vertical distribution is known. Therefore we follow some assumptions made by MacLean (2026). A first assumption we make is that the effects of the vertical variation in H and K_H on the far-field contribution are very small relative to the contribution of the air above the canopy. Therefore, the contribution to the far-field component can be approximated as:

$$\int_z^h \frac{H(z_i)}{K_H(z_i)} dz \approx \frac{H_C}{\bar{K}_{h,0}} \left(1 - \frac{z}{h}\right)$$

In this formula, the H_C is the total heat flux resulting from the combined canopy elements and $\bar{K}_{h,0}$ is the average thermal diffusivity within the canopy (from ground to the top of the canopy):

$$\frac{1}{\bar{K}_{h,0}} = h \int_0^h \frac{1}{K_H(z)} dz$$

A second assumption that can be made is the fact that we treated the initial vegetated surface (to calculate the above canopy properties) was treated as a single layer of phytomass. Therefore, technically the sensible heat flux resulting form the top of this layer is the combination canopy components (H_C) and the underlying ground surface (H_G). Whereby the sensible heat flux calculated in previous section is given by $H = H_C + H_G$. Now the assumption can be made that the fraction H_G/H is equal to the proportion of ground surface that is not covered by canopy elements in a way that:

$$H_G = H\, e^{-Pai}, H_C = H\, (1 - e^{-Pai})$$

Whit this in mind, we can create an energy balance equation for T_z below the canopy:

$$\tilde{\rho} c_p \bar{K}_{z,0} (T_G - T_z) + \tilde{\rho} c_p \bar{K}_{h,z} (T_H - T_z) + \tilde{\rho} c_p \bar{K}_{h,0} (T_C - T_z) = 0$$

With T_C the temperature of the canopy elements at the top of the canopy and T_H the air temperature at the top of the canopy given by:

$$T_H = T_C - \frac{H_C}{\tilde{\rho} c_p \bar{K}_{h,0}}$$

We can now use the last two formulae to solve for T_G the ground temperature:

$$T_G = T_z + \frac{\bar{K}_{h,z}}{\bar{K}_{z,0}} \left(T_z - T_C + \frac{H_C}{\tilde{\rho} c_p \bar{K}_{h,0}} \right) + \bar{K}_{h,0} (T_z - T_C)$$

Here the mean thermal diffusivities $\bar{K}_{z,0}$, $\bar{K}_{h,0}$ and $\bar{K}_{h,z}$ can be derived by integration following MacLean (2026):

$$\frac{1}{\overline{K}_{z,0}} = z\int_0^z \frac{1}{K_H(z)}dz = z\frac{2}{a_2\,\pi\,u_*}\left(\frac{48\tan\frac{\sqrt{5}\,f_1}{f_2}}{5^{3/2}} + \frac{32\,f_1}{f_2\left(\frac{25\,f_1}{f_2^2}+5\right)}\right)$$

Where:

$$f_1 = \sin x\,, \qquad f_2 = \cos x + 1, \qquad x = \frac{\pi z}{h}$$

In the case where $z = h$, this results in:

$$\frac{1}{\overline{K}_{h,0}} = h\int_0^h \frac{1}{K_H(z)}dz = h\frac{4.293251}{a_2\,u_*}$$

For $\overline{K}_{h,z}$ we can use:

$$\frac{1}{\overline{K}_{h,z}} = (h-z)\int_z^h \frac{1}{K_H(z)}dz = (h-z)\left[\int_0^h \frac{1}{K_H(z)}dz - \int_0^z \frac{1}{K_H(z)}dz\right]$$

A third assumption is related to the computation of the near-field contribution. The effects of the kernel function k_n are such that at height z the near-field concentration is more influenced by the local source concentration $S(z)$ and the contributions at other heights z_i are negligible when $|z - z_i| \gg 0$. Therefore the near-field contribution $C_n(z)$ can be determined just on $S(z)$ with a minor adjustment (C_s, empirically derived (Maclean, 2026)) based on plant area index:

$$C_n(z) = S(z)(3.05 + 0.129\ln Pai), \qquad S(z) = f_d(z)H(z)$$

To recapitulate, the air temperature at height z with the canopy (T_z) can be given as:

$$\tilde{\rho}c_pT_z = \tilde{\rho}c_pT_H - C_n(h) + \int_z^h \frac{H(z_i)}{K_H(z_i)}dz + C_n(z)$$

From what we learned in the derivations above and the assumptions made, we can reformulate this to:

$$T_z = T_H + \frac{H_C}{\tilde{\rho}c_p\overline{K}_{h,0}}\left(1-\frac{z}{h}\right) - \frac{S(h)C_s}{\tilde{\rho}c_p} + \frac{S(z)C_s}{\tilde{\rho}c_p}, \qquad C_s = (3.05 + 0.129\ln Pai)$$

$$=> T_z = T_C - \frac{z\,H_C}{h\,\tilde{\rho}c_p\overline{K}_{h,0}} - \frac{f_d(h)HC_s}{\tilde{\rho}c_p} + \frac{f_d(z)H(z)C_s}{\tilde{\rho}c_p}$$

$$=> T_z = T_C - \frac{z\,4.293251\,H\,(1-e^{-Pai})}{\tilde{\rho}c_pa_2\,u_*} - \frac{f_d(h)HC_s}{\tilde{\rho}c_p} + \frac{f_d(z)H(z)C_s}{\tilde{\rho}c_p}$$

Note, we now have almost everything to calculate T_z, T_C is the canopy temperature, given by the LST derived from the thermal UAV data, H is the sensible heat flux at the top of the phytomass layer, calculated in the previous step, the derivation of the above canopy properties, this also allowed us to get the friction velocity u_*. The constant a_2 can also be determined using the diabatic correction coefficient for heat. The only variable still needed is the heat flux at height z:

$$H(z) = \frac{\tilde{\rho}c_p}{r_L}\left(T_{c_z} - T_{\mathrm{z}}\right) + \tilde{\rho}c_p\overline{K}_{z,0}(T_G - T_z)$$

With T_{c_z} the temperature of the canopy elements at height z, r_L the boundary layer resistance of the leaves given $r_L = 318\sqrt{0.71\,L_w/u_z}$ with L_w the leaf with (m) and u_z the wind speed (m s^{-1}) given by Harman and Finnigan (2008):

$$u_z = u_h \exp\left(\frac{\beta}{L_M}(z-h)\right)$$

In this formula, u_h represents the windspeed at the top of canopy with height h, the parameter β is given by u_*/u_h, and $L_M = 2\beta^2 L_C$ where $L_C = (0.25\,Pai/h)^{-1}$. The wind speed at the top of the canopy can then be calculated as:

$$u_h = \frac{u_*}{\kappa}\left(\ln\frac{h-d}{z_M} + \psi_M(h)\right)$$

With κ the Von Karman constant, z_M the roughness length for momentum (calculated from the above canopy properties), d the zero-plane displacement length and $\psi_M(h)$ the diabatic correction factor for momentum.

We have now a way to describe T_z based on known variables, T_{c_z} and T_G. The latter two are technically not known yet, but we can express them in function of different variables and T_z itself. We can now solve for these three parameters using a numerical optimization technique, similar to the approach in the above canopy temperature situation.

Note: one should remain cautious when applying the formulae or interpreting the data. Here we test this approach, proposed by MacLean (2026), and adapted it to our use case to test against in situ loggers. With this study we want to show the potential of incorporating thermal UAV data into mechanistic microclimate modelling.

Appendix G. Comparison: measured vs. predicted

Accuracy Metrics

When compared to the loggers present in the flight block "ANBH1", the GBM model obtains the best metric values. One should note that this reason is two-fold: (I) the GBM is directly trained on the in situ loggers themselves and, (II) for T_{0cm} the GBM best represents the temperature at 0 cm, while the other two models provide the land surface temperature and could therefore only be evaluated for the land cover *Moss,* explaining the high RMSE (Table G1). The in situ loggers here are seen as a common reference to perform the comparison.

***Table G1. Accuracy metrics for the different approaches** calculated from the loggers in ANBH1 (n = 30) across all land covers and flights. Note, for T_{13cm} the land cover "tree" is not taken into account due to lack of data. For T_{0cm} the metrics are solely calculated for the landcover "Moss" for microclimf and the Thermal UAV approach as this is the only representable LC class, for the GBM model all land cover classes could be evaluated.*

	T_{13cm}		**T_{0cm}**	
Model	**RMSE (°C)**	**R^2**	**RMSE (°C)**	**R^2**
GBM	2.217	0.850	2.636	0.719
Microclimf	4.427	0.645	6.283	0.598
Thermal UAV	3.372	0.775	13.834	0.402

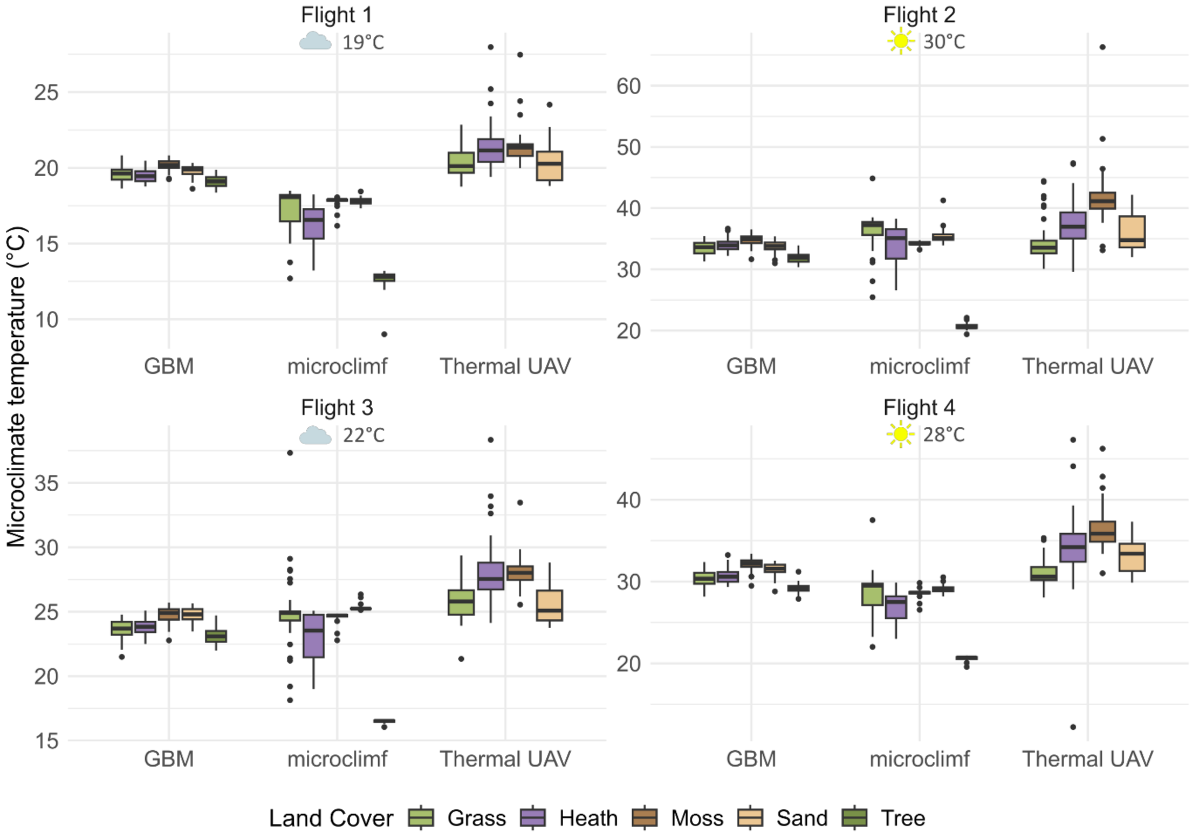

***Figure G1. Comparison of the modelled microclimate temperature at 13cm of 50 random points per land cover types of ANBH1.** Note, the land cover "tree" is not available for the Thermal UAV approach.*

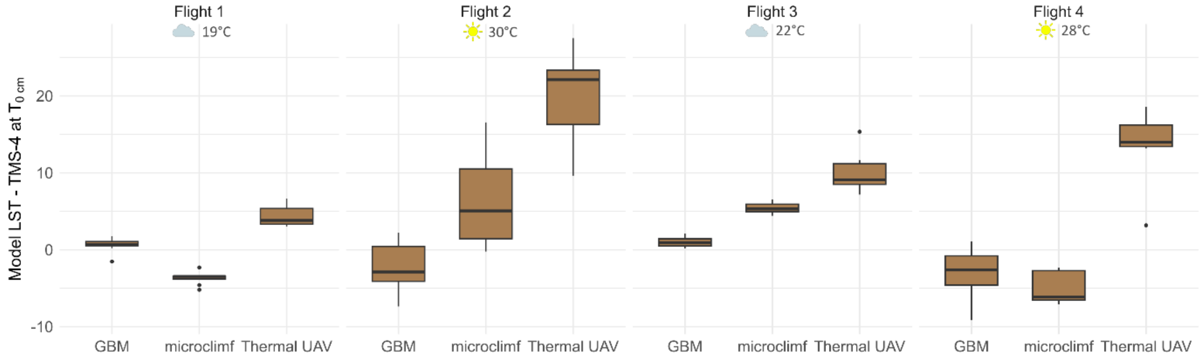

Figure G2. The difference between the model output and the corresponding measured microclimate for LST/T_{0cm} *for the different models for the different flight days for the landcover Moss.*

Scatter Plots

To compare the output of the different modelling approaches with the in-situ logger measurements we plotted for each model the model prediction against the temperature measured with the TOMST TMS-4 loggers. This for both the ground surface temperature (T_{0cm}, or the TMS-4 T2 sensor) as well as the near surface air temperature measured at 13 cm (T_{13cm}, or the TMS-4 T3 sensor). The data is grouped per land cover class (colour) and flight date (symbol). Note, the ground surface temperature can only be compared with the in-situ measurements for areas where they both represent the same surface (i.e., Mosses). Figure G3, Figure G4 and Figure G5 show the scatter plots for near surface air temperature (T_{13cm}) for respectively the gradient boosted model (GBM), the mechanistic *microclimf* model and the thermal UAV data. The scatter plots for the ground surface temperatures of these models are shown in Figure G6, Figure G7 and Figure G8.

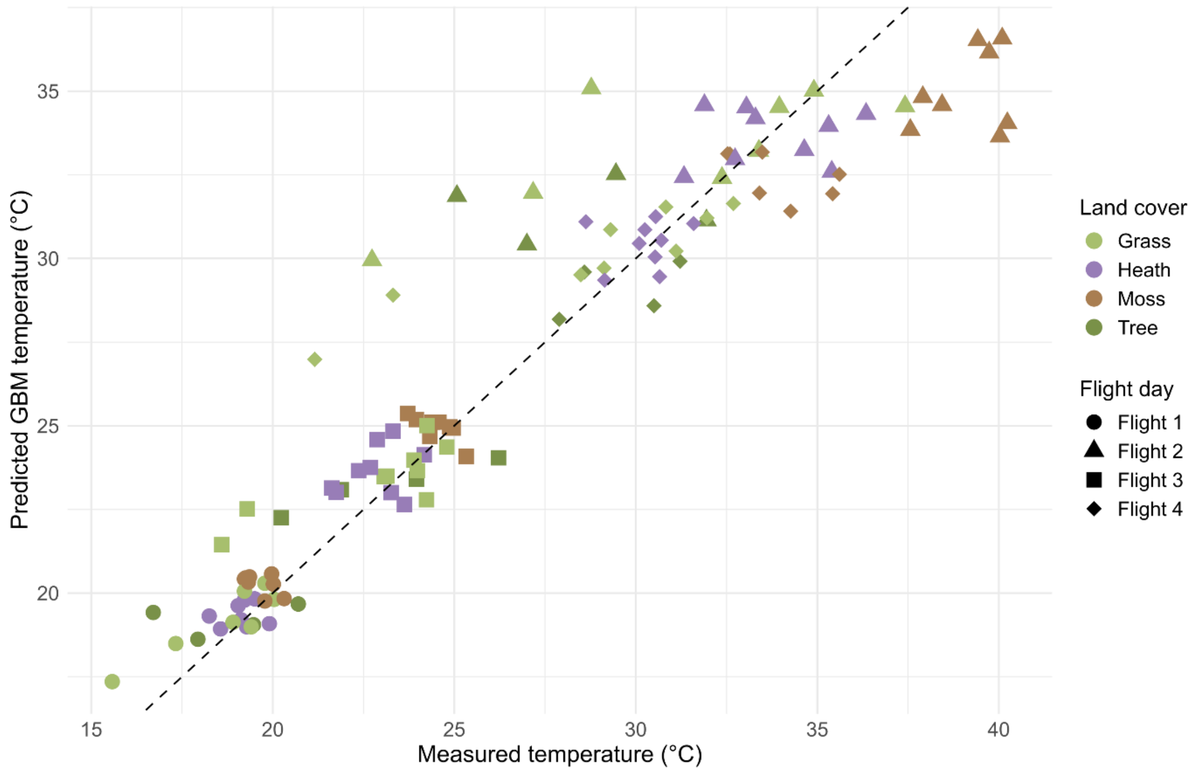

Figure G3. Measured vs. Predicted GBM microclimate at 13 cm. *Scatter plot of the measured (TOMST TMS-4 T3) versus predicted near air surface temperatures at 13 cm for the gradient boosted model (GBM). The colours represent the different landcover classes, the symbols the different flight days. Where flight 1 and 3 were overcast conditions and flight 2 and 4 had clear skies with full incoming solar radiation.*

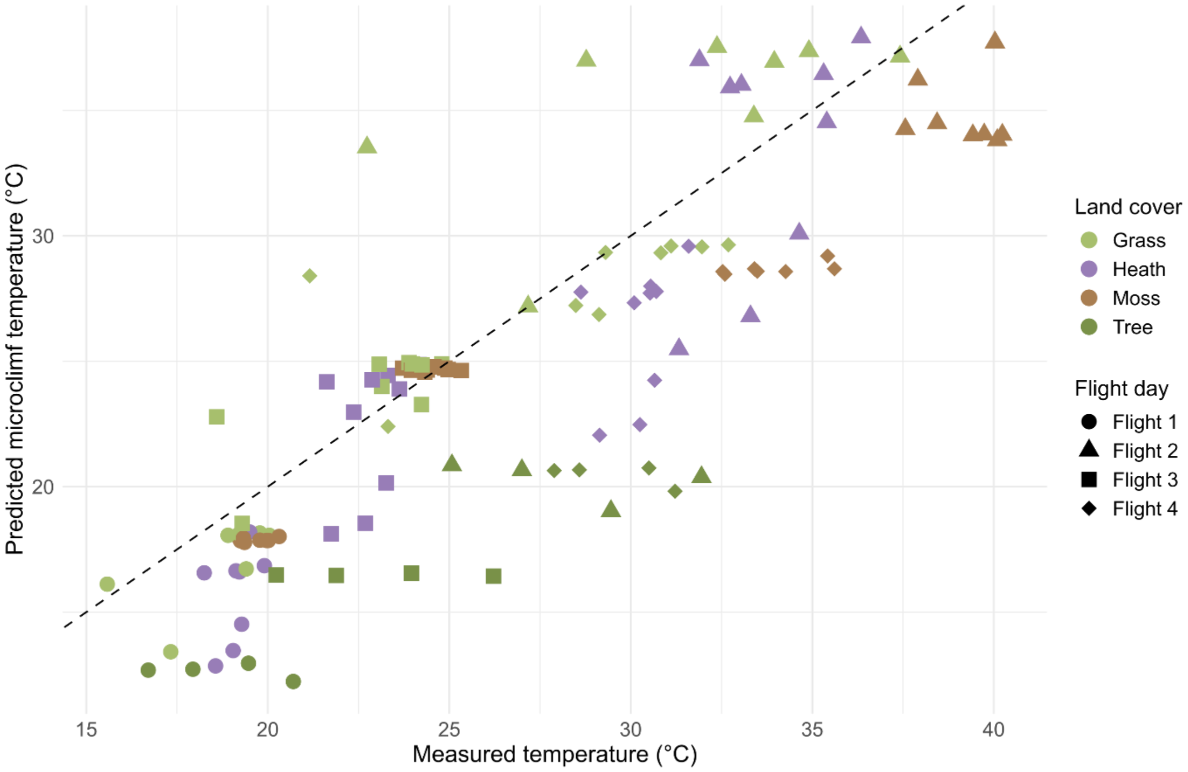

Figure G4. Measured vs. Predicted microclimf microclimate at 13 cm. *Scatter plot of the measured (TOMST TMS-4 T3) versus predicted near air surface temperatures at 13 cm for the microclimf model. The colours represent the different landcover classes, the symbols the different flight days. Where flight 1 and 3 were overcast conditions and flight 2 and 4 had clear skies with full incoming solar radiation.*

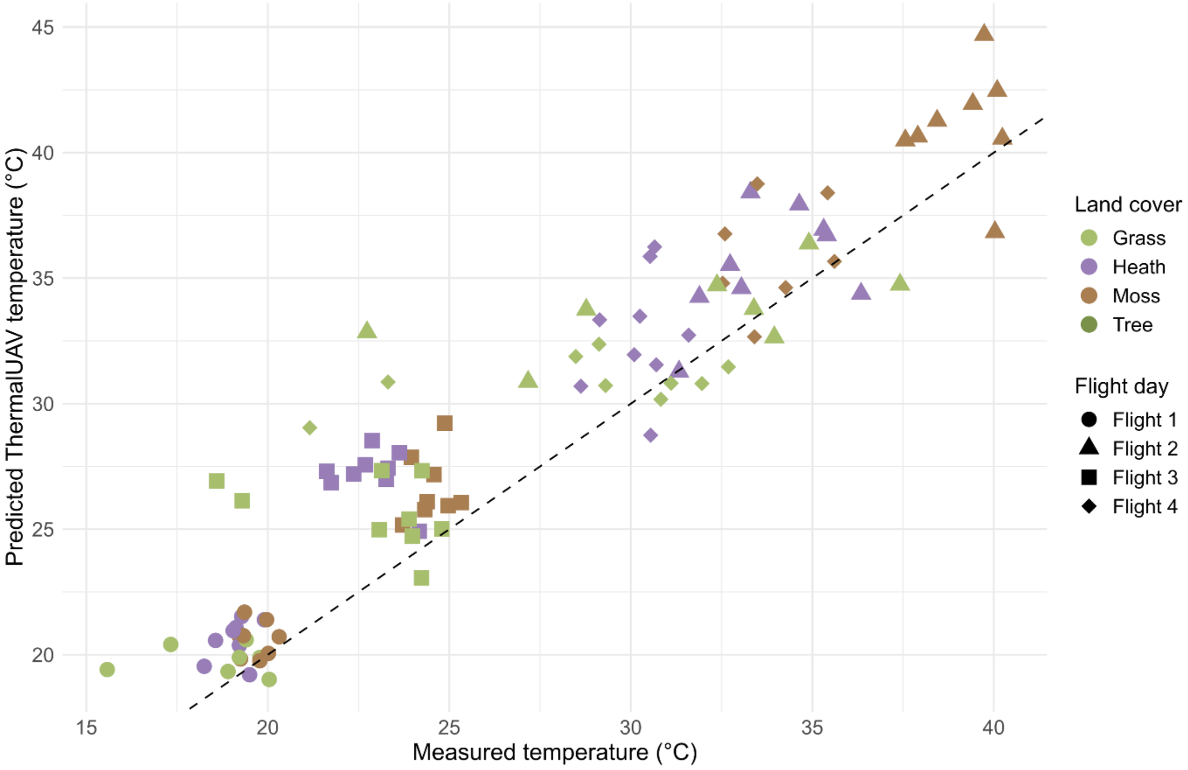

Figure G5. Measured vs. Predicted Thermal UAV microclimate at 13 cm. *Scatter plot of the measured (TOMST TMS-4 T3) versus predicted near air surface temperatures at 13 cm for the thermal UAV approach. The colours represent the different landcover classes, the symbols the different flight days. Where flight 1 and 3 were overcast conditions and flight 2 and 4 had clear skies with full incoming solar radiation.*

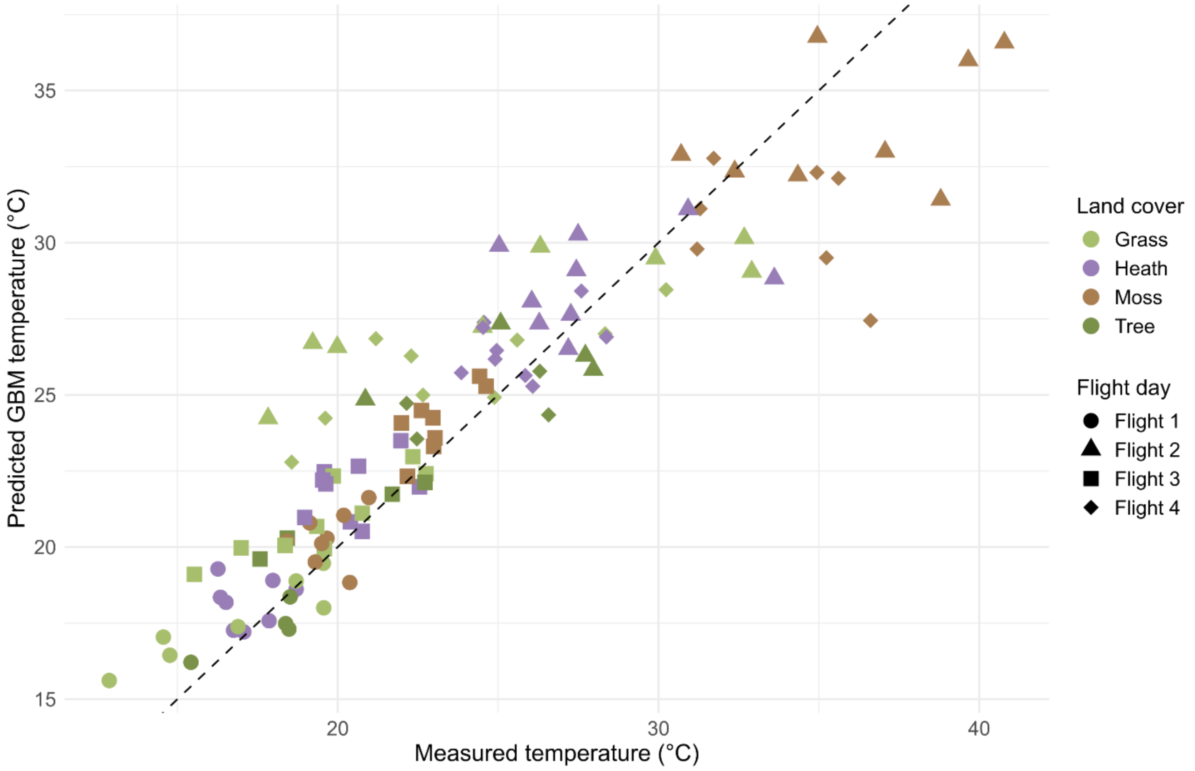

Figure G6. Measured vs. Predicted GBM LST microclimate (at 0 cm). *Scatter plot of the measured (TOMST TMS-4 T2) versus predicted ground surface temperatures at 0 cm for the microclimf model. The colours represent the different landcover classes, the symbols the different flight days. Where flight 1 and 3 were overcast conditions and flight 2 and 4 had clear skies with full incoming solar radiation.*

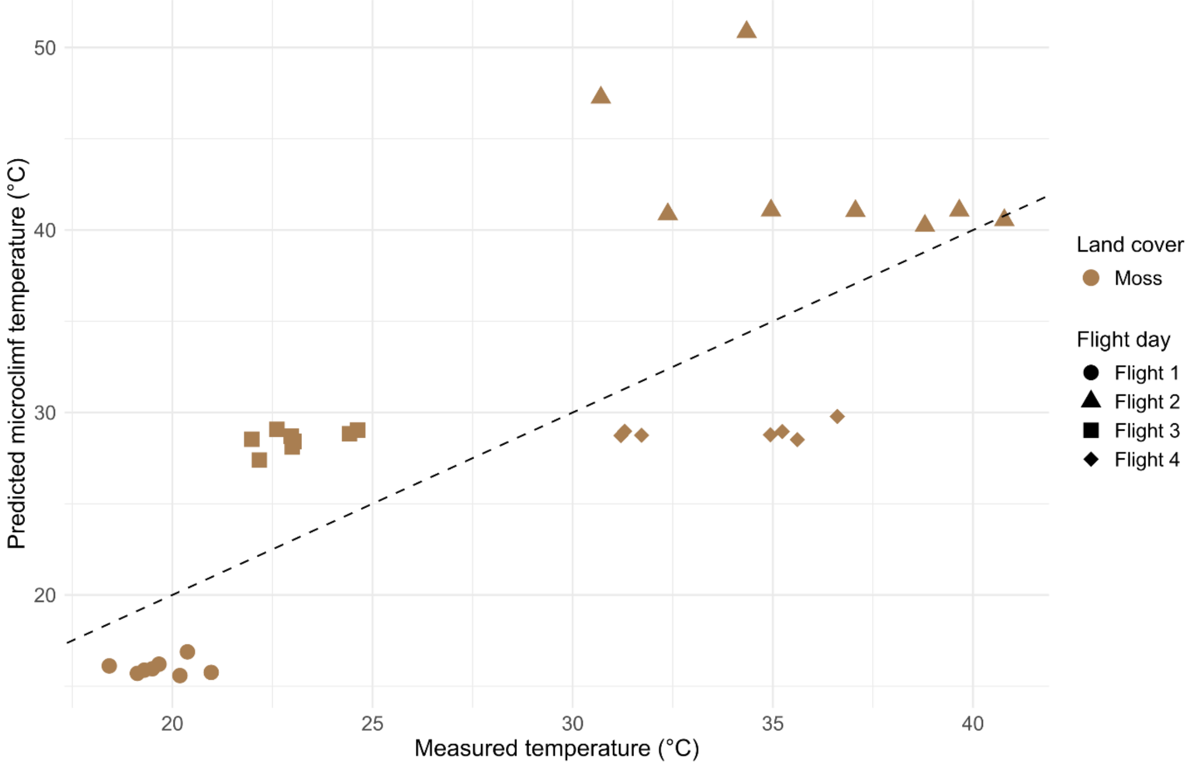

Figure G7. Measured vs. Predicted microclimf LST microclimate. *Scatter plot of the measured (TOMST TMS-4 T2) versus predicted leaf surface temperatures for the microclimf model. Note only the landcover class moss is presented, the symbols the different flight days. Where flight 1 and 3 were overcast conditions and flight 2 and 4 had clear skies with full incoming solar radiation.*

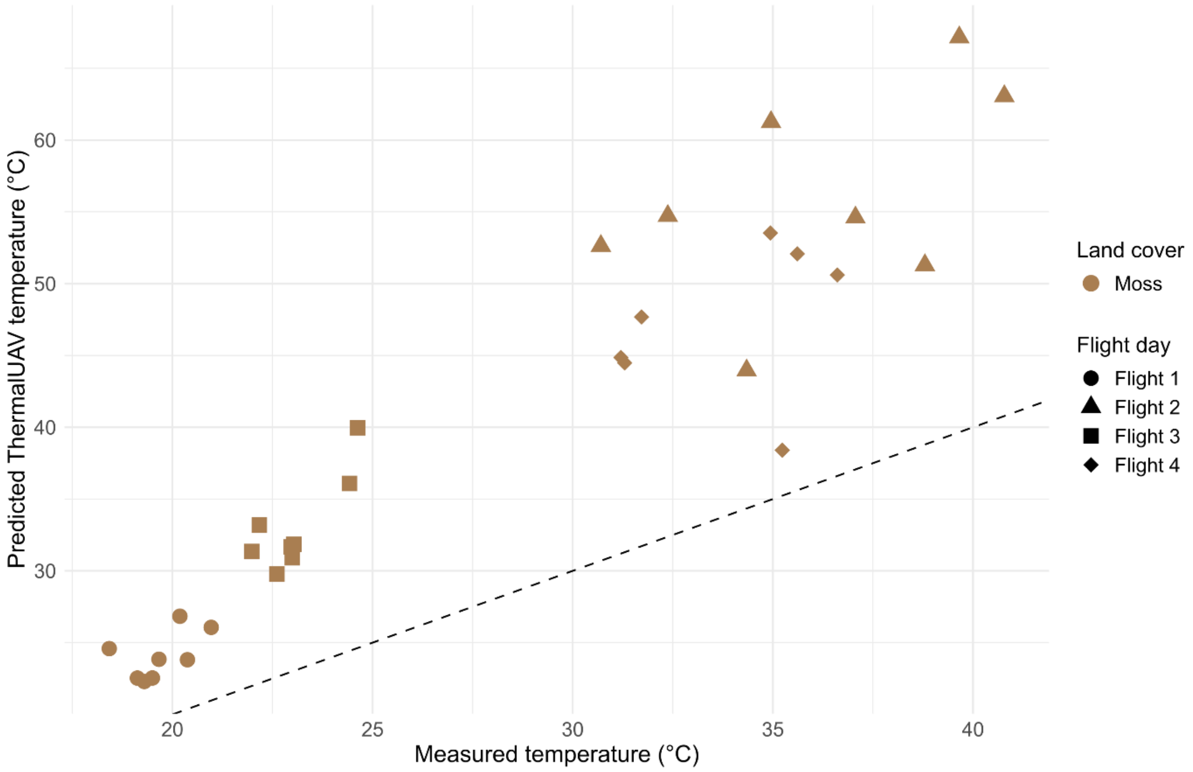

Figure G8. Measured vs. Predicted Thermal UAV LST microclimate. *Scatter plot of the measured (TOMST TMS-4 T2) versus the measured land surface temperatures from the thermal UAV. Note only the landcover class moss is presented, the symbols the different flight days. Where flight 1 and 3 were overcast conditions and flight 2 and 4 had clear skies with full incoming solar radiation.*

Appendix H. Temperature Offsets

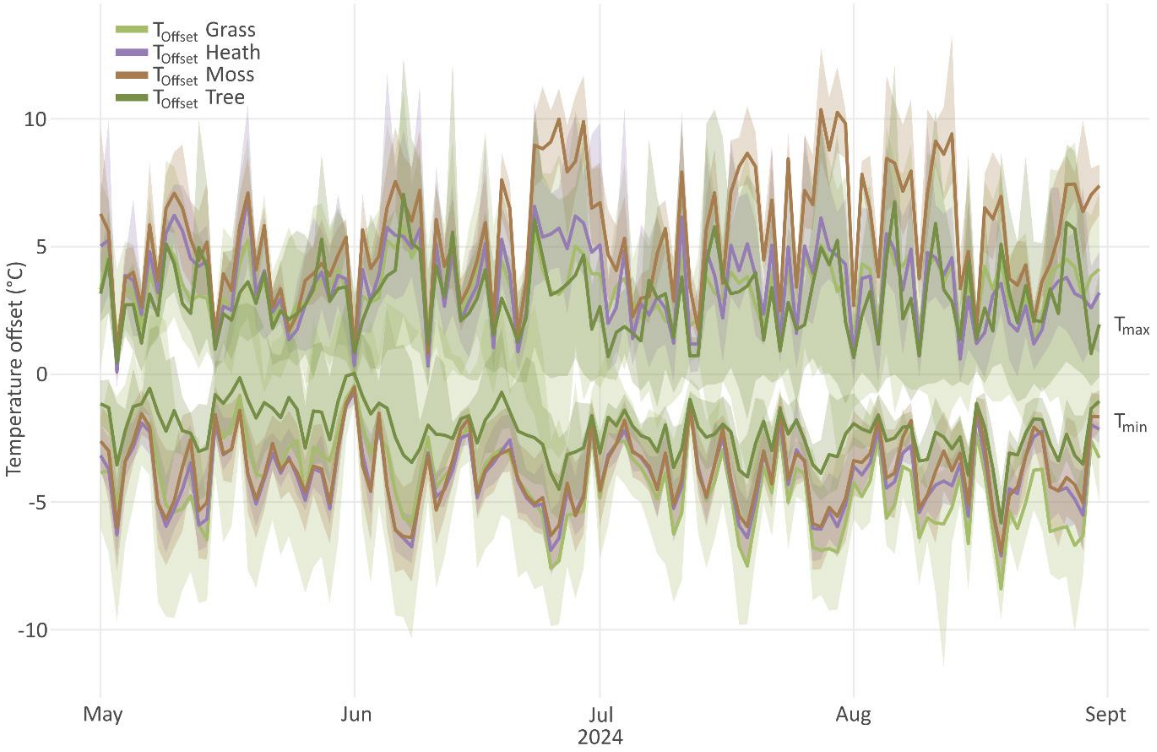

Figure H1. The daily maximum and minimum offset of the T_{13cm} microclimate compared to the macroclimate temperature *calculated from the TOMST TMS-4 loggers present in the focus area ANBH1. The observed offsets are much larger compared to the offsets observed in forest ecosystems, even in the shaded shrubs or under solitary trees/tree patches.*

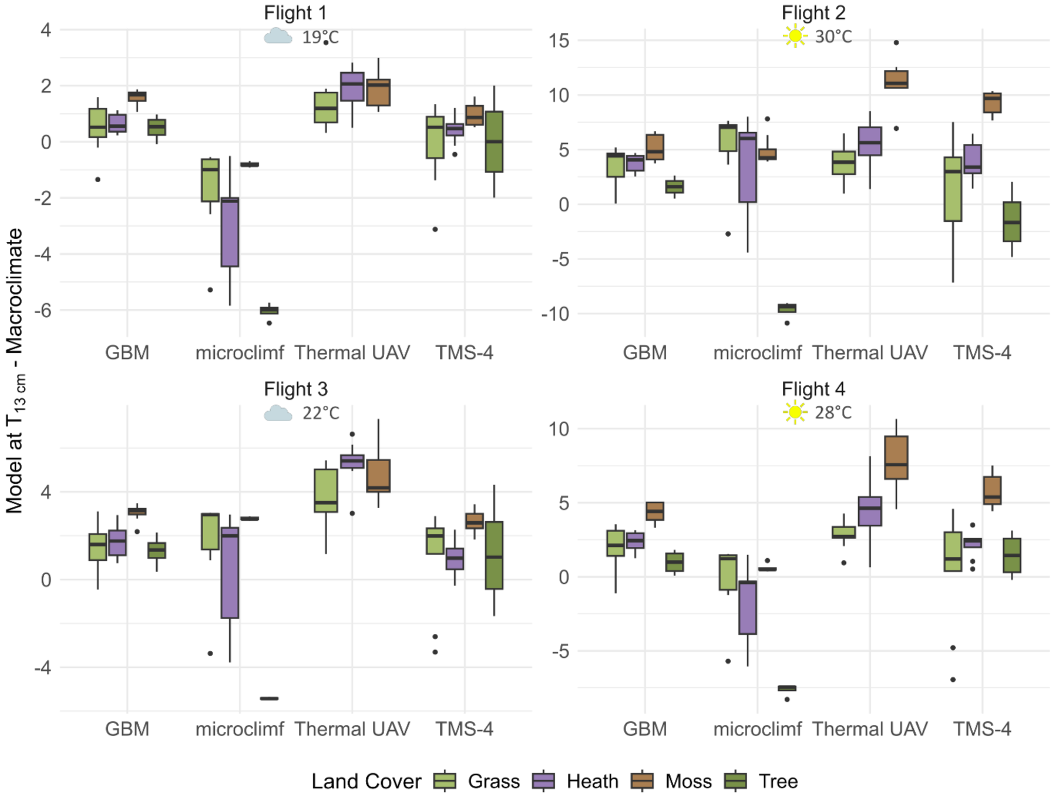

Figure H2. Offsets of T_{13cm} calculated per method on the logger locations on the instances of comparison per land cover. *Note, the loggers themselves are also included in this figure.*

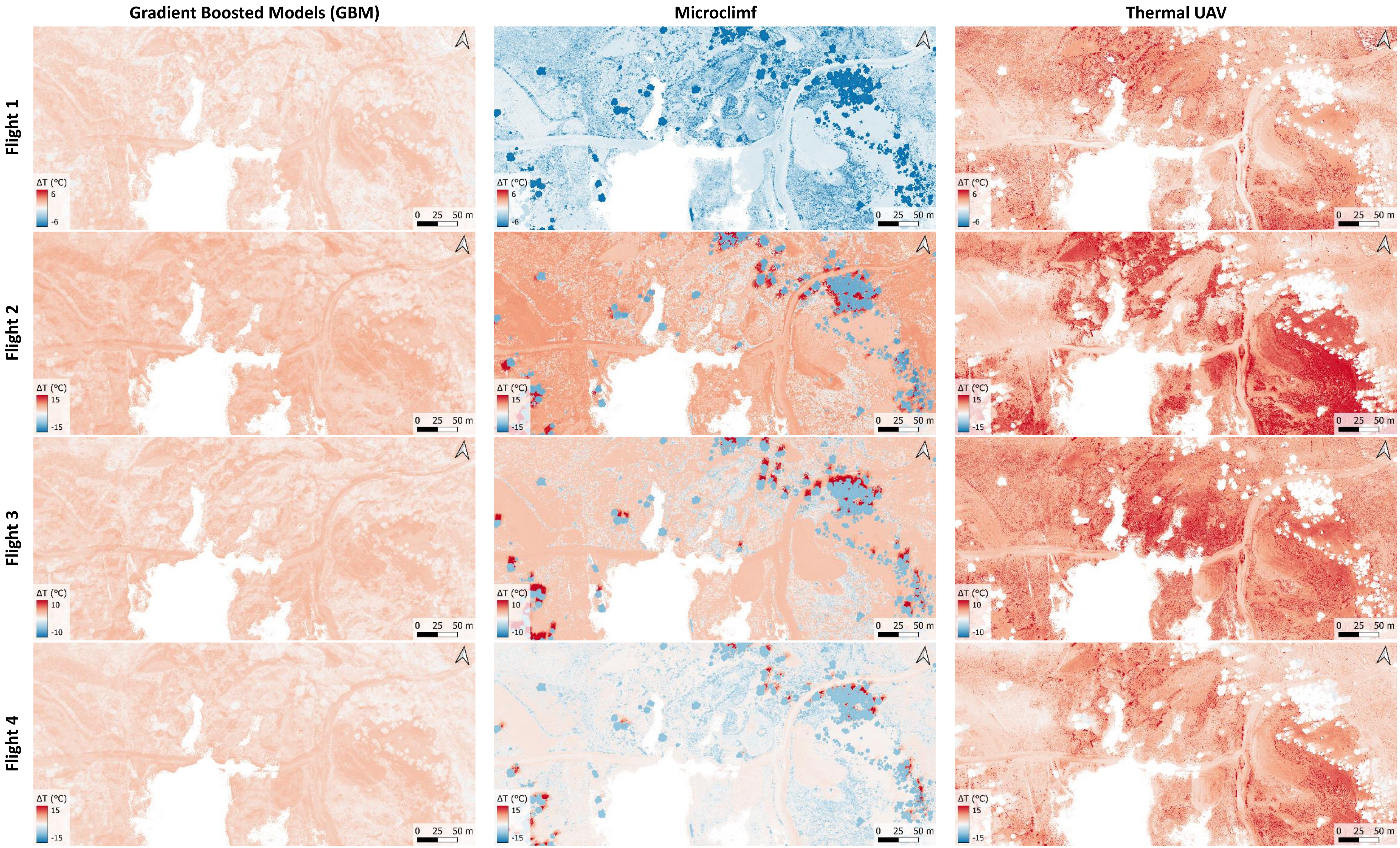

Figure H3. Microclimate T_{13cm} offsets per method for each day, presented as spatial maps. *The microclimf approach suggests negative offsets on the coldest overcast day. This method furthermore shows very large legative offsets under trees. The thermal UAV approach shows extreme positive offsets, indicating much warmer temperatures compared to the macroclimate. The GBM approach is much more reserved in the offsets, but consistently predicts higher temperatures compared to the weather station data.*

Appendix I. Models with adjusted CHM

The canopy height models in our study are derived from a UAV LiDAR system. However, when working at very small scales (e.g., height of mosses) and in dense systems (e.g., dense shrubs), the derived canopy height model (CHM) can yield over- or underestimations. Especially, when converting land surface temperatures (LST) to near surface air temperatures, the canopy height plays a large role in modelling the temperature profile near the ground. Here, an overestimation of the moss height can lead to higher near surface air temperatures. To test this, we artificially set the CHM of moss to 1 cm and calculated the model output for the *microclimf* model and the derivation from LST again. In this appendix we present the output of the models with an adjusted CHM. The accuracy metrics (Table I1) only show a slight increase as we didn't change anything for the other land cover classes, the effect is furthermore less noticeable when there is good air flow/mixing. Only on the very hot day, with low wind speeds, this effect is large (flight 2). We demonstrate this based on some loggers in the field above moss layers (Figure I1).

Table I1. Accruacy metrics for the different approaches when setting the CHM artificially to 1 cm for moss.

	T_{13cm}		$T_{Surface}$	
Model	**RMSE (°C)**	**R²**	**RMSE (°C)**	**R²**
GBM	2.217	0.850	2.636	0.720
Microclimf	4.424	0.644	7.762	0.412
Thermal UAV	3.067	0.787	9.948	0.412

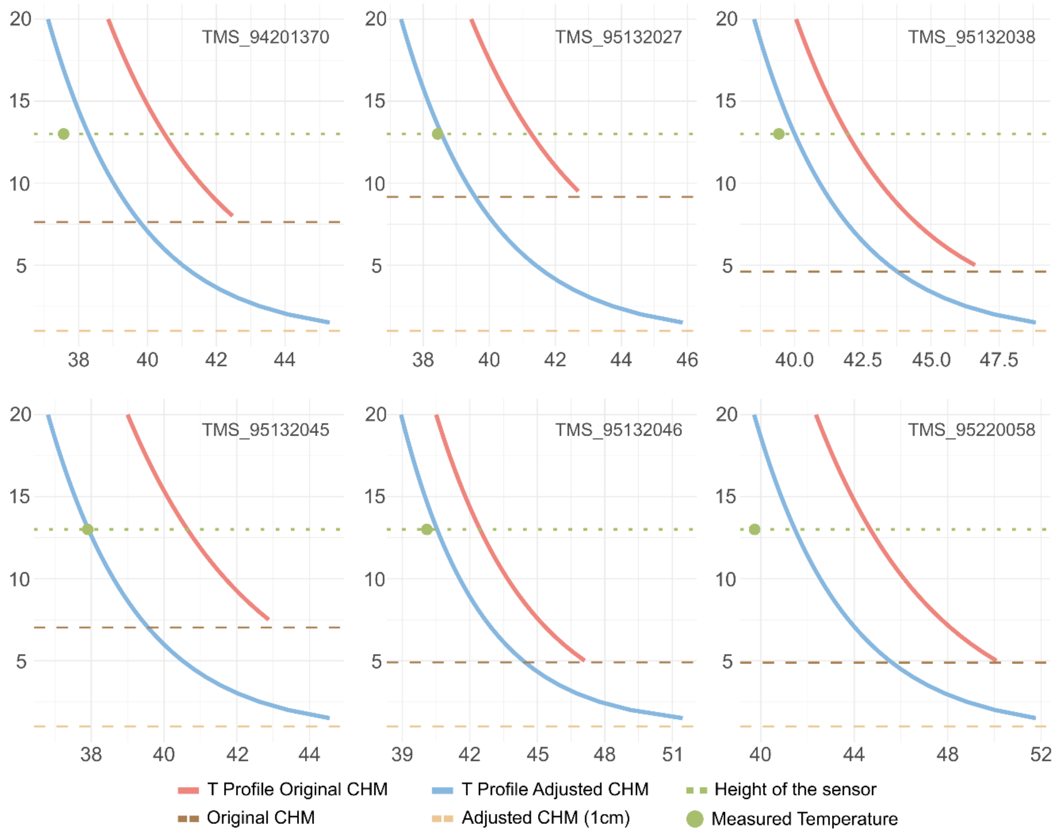

Figure I1. Temperature profiles above moss derived from the LST using the MOST theory. *The temperature profiles when using the original CHM do not decrease fast enough compared to the temperature profiles with the adjusted CHM, in blue.*

Appendix J. throne package test

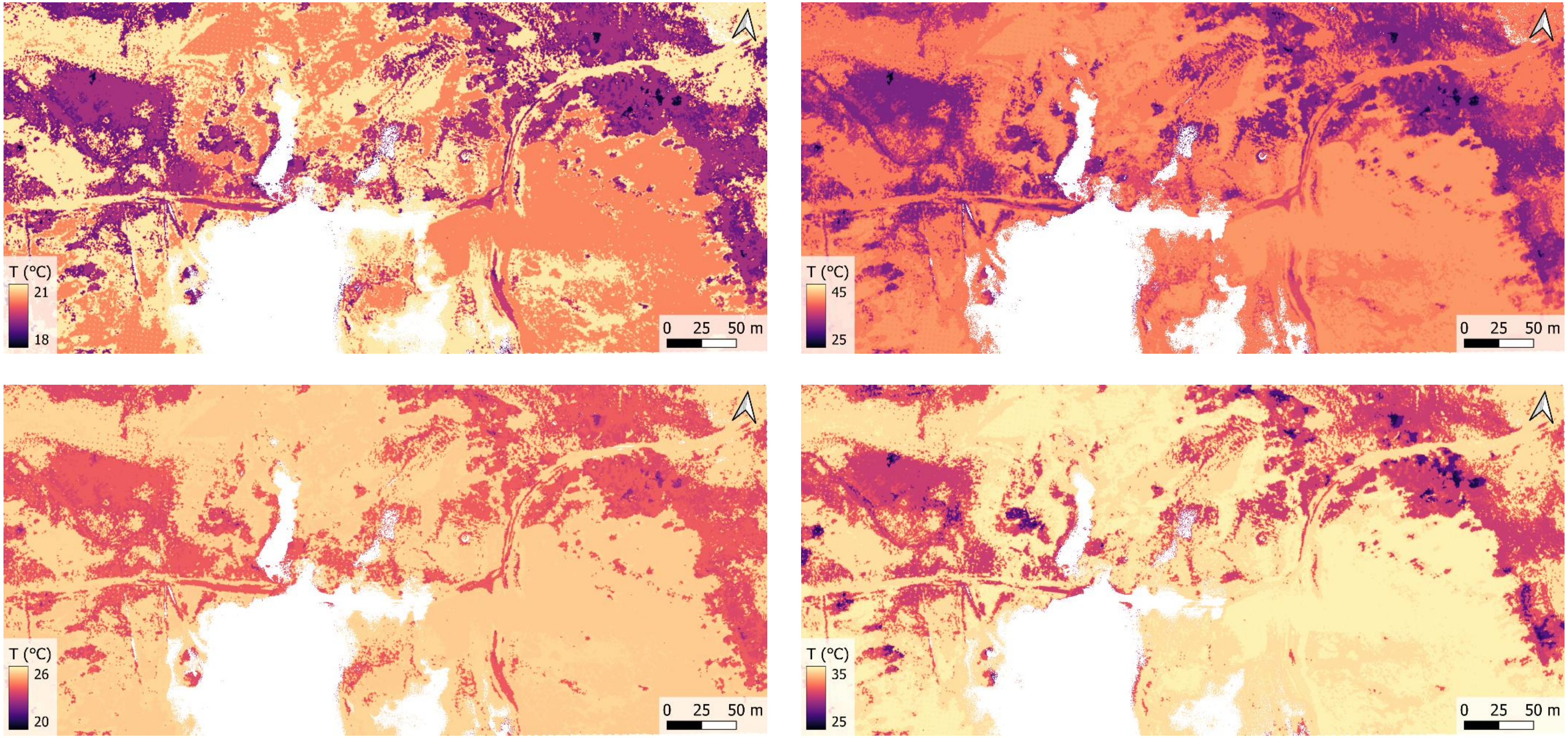

Figure J1. The output of the throne package for the ground surface temperature (T_{0cm}) for flight 1-4 (top left to bottom right). *Instead of operative temperature loggers, we used the TMS-4 T2 loggers to establish a relationship with the four thermal flights. While only a limited amount of data was used, the workflow was able to uncover temporally interpolated spatial maps showing thermal heterogeneity with warmer and colder areas also observed in the instances for the comparison.*

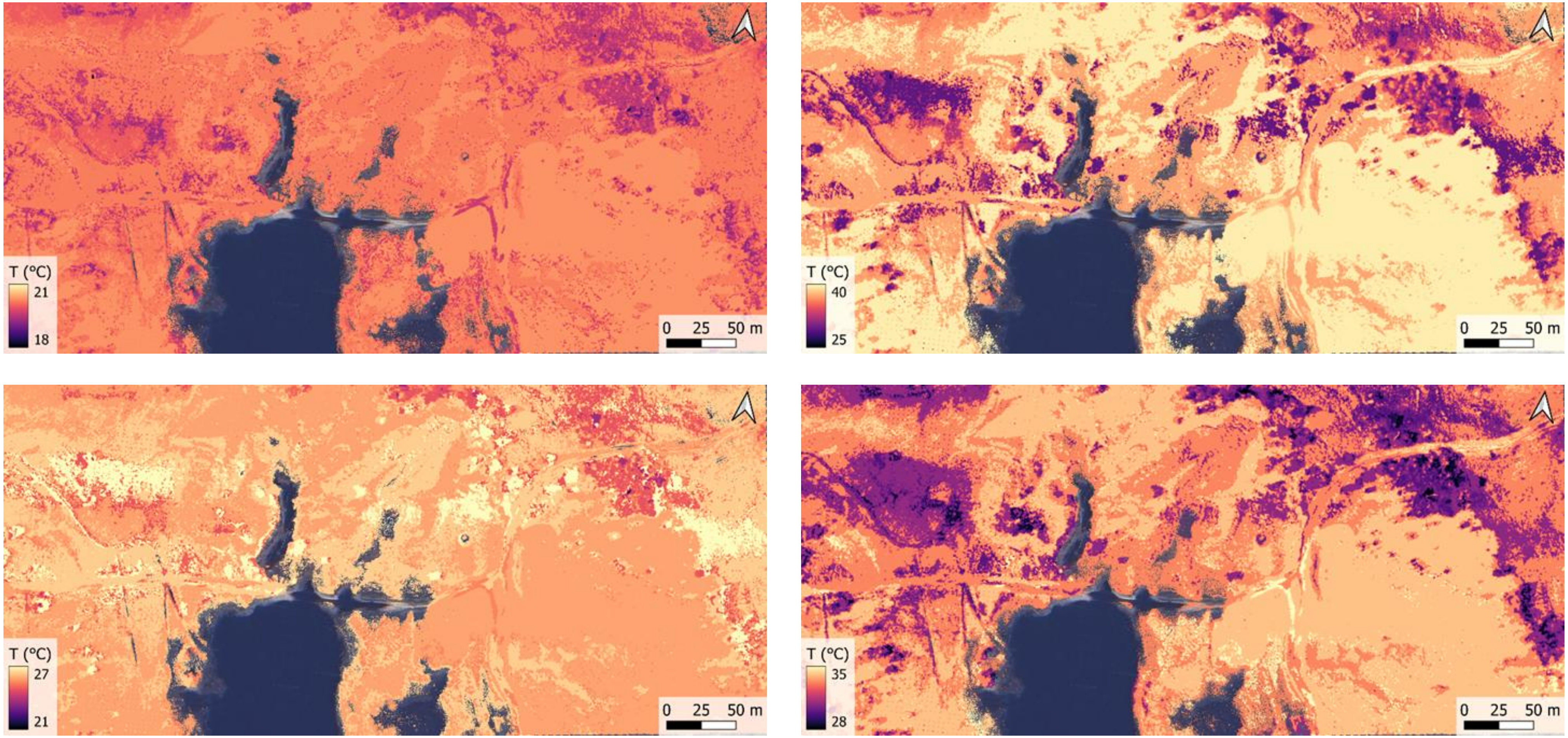

Figure J2. The output of the throne package for the near surface air temperature (T_{13cm}) for flight 1-4 (top left to bottom right). *Instead of operative temperature loggers, we used the TMS-4 T3 loggers to establish a relationship with the four thermal flights. While only a limited amount of data was used, the workflow was able to uncover temporally interpolated spatial maps showing thermal heterogeneity with warmer and colder areas also observed in the instances for the comparison.*

References

Bonan, G.B., Patton, E.G., Finnigan, J.J., Baldocchi, D.D., Harman, I.N., 2021. Moving beyond the incorrect but useful paradigm: reevaluating big-leaf and multilayer plant canopies to model biosphere-atmosphere fluxes – a review. Agric. For. Meteorol. 306, 108435. https://doi.org/10.1016/j.agrformet.2021.108435

Businger, J.A., Wyngaard, J.C., Izumi, Y., Bradley, E.F., 1971. Flux-Profile Relationships in the Atmospheric Surface Layer. J. Atmos. Sci. 28, 181–189.

Campbell, G.S., Norman, J.M., 1998. An Introduction to Environmental Biophysics. Springer New York, New York, NY. https://doi.org/10.1007/978-1-4612-1626-1

Foken, T., 2006. 50 Years of the Monin–Obukhov Similarity Theory. Boundary. Layer. Meteorol. 119, 431–447. https://doi.org/10.1007/s10546-006-9048-6

Harman, I.N., Finnigan, J.J., 2008. Scalar Concentration Profiles in the Canopy and Roughness Sublayer. Boundary. Layer. Meteorol. 129, 323–351. https://doi.org/10.1007/s10546-008-9328-4

Hijmans, R., 2022. terra: Spatial Data Analysis.

Ilich, A.R., Misiuk, B., Lecours, V., Murawski, S.A., 2023. MultiscaleDTM: An open-source R package for multiscale geomorphometric analysis. Transactions in GIS 27, 1164–1204. https://doi.org/10.1111/tgis.13067

Kuhn, M., 2008. Building Predictive Models in R Using the caret Package. J. Stat. Softw. 28. https://doi.org/10.18637/jss.v028.i05

Maclean, I.M.D., 2026. Microclimf: Fast modelling of microclimate across real landscapes in R. Methods Ecol. Evol. https://doi.org/10.1111/2041-210x.70253

Maclean, I.M.D., 2025. microctools: Various worker functions for microclimc package.

Maes, W.H., Huete, A.R., Steppe, K., 2017. Optimizing the processing of UAV-based thermal imagery. Remote Sens. (Basel). 9. https://doi.org/10.3390/rs9050476

Metsu, C., Maes, W.H., Ottoy, S., Van Meerbeek, K., 2026. theRmalUAV: An R package to clean and correct thermal UAV data for accurate land surface temperatures. Methods Ecol. Evol. 17, 488–496. https://doi.org/10.1111/2041-210x.70196

Monin, A.S., Obukhov, A.M., 1954. Basic laws of turbulent mixing in the surface layer of the atmosphere. Tr. Akad. Nauk SSSR Geophiz. Inst. 24, 163–187.

Ogée, J., Brunet, Y., Loustau, D., Berbigier, P., Delzon, S., 2003. MuSICA , a CO 2 , water and energy multilayer, multileaf pine forest model: evaluation from hourly to yearly time scales and sensitivity analysis. Glob. Chang. Biol. 9, 697–717. https://doi.org/10.1046/j.1365-2486.2003.00628.x

R Core Team, 2023. R: A Language and Environment for Statistical Computing.

Raupach, M.R., 1989a. Applying Lagrangian fluid mechanics to infer scalar source distributions from concentration profiles in plant canopies. Agric. For. Meteorol. 47, 85–108.

Raupach, M.R., 1989b. A practical Lagrangian method for relating scalar concentrations to source distributions in vegetation canopies. Quarterly Journal of the Royal Meteorological Society 115, 609–632.

Ridgeway, G., GBM Developers, 2024. gbm: Generalized Boosted Regression Models. https://doi.org/10.32614/CRAN.package.gbm

Rubio, E., Caselles, V., Badenas, C., 1997. Emissivity measurements of several soils and vegetation types in the 8-14 µm wave band: Analysis of two field methods. Remote Sens. Environ. 59, 490–521. https://doi.org/10.1016/S0034-4257(96)00123-X

TeAx Technology, 2020. ThermoViewer.

Wild, J., Kopecký, M., Macek, M., Šanda, M., Jankovec, J., Haase, T., 2019. Climate at ecologically relevant scales: A new temperature and soil moisture logger for long-term microclimate measurement. Agric. For. Meteorol. 268, 40–47. https://doi.org/10.1016/j.agrformet.2018.12.018

Wright, M.N., Ziegler, A., 2017. ranger : A Fast Implementation of Random Forests for High Dimensional Data in C++ and R. J. Stat. Softw. 77. https://doi.org/10.18637/jss.v077.i01

Yasuda, N., 1988. Turbulent diffusivity and diurnal variations in the atmospheric boundary layer. Boundary. Layer. Meteorol. 43, 209–221. https://doi.org/10.1007/BF00128403